



Maria Clara Carvalho Teixeira

**Fatigue failure assessment in ultrasonic
test based on temperature evolution and
crack initiation mechanisms**

Tese de Doutorado

Thesis presented to the Programa de Pós-Graduação em Engenharia de Materiais e de Processos Químicos e Metalúrgicos of PUC-Rio in partial fulfillment of the requirements for the degree of Doutor em Engenharia de Materiais e de Processos Químicos e Metalúrgicos.

Advisor: Prof. Marcos Venicius Soares Pereira

Rio de Janeiro
April 2023



Maria Clara Carvalho Teixeira

**Fatigue failure assessment in ultrasonic
test based on temperature evolution and
crack initiation mechanisms**

Thesis presented to the Programa de Pós-Graduação em Engenharia de Materiais e de Processos Químicos e Metalúrgicos of PUC-Rio in partial fulfillment of the requirements for the degree of Doutor em Engenharia de Materiais e de Processos Químicos e Metalúrgicos. Approved by the Examination Committee.

Prof. Marcos Venicius Soares Pereira

Advisor

Departamento de Engenharia Química e de Materiais - PUC-Rio

Profa. Amanda Lemette Teixeira Brandão

Departamento de Engenharia Química e de Materiais - PUC-Rio

Profa. Ana Rosa Fonseca de Aguiar Martins

Departamento de Engenharia Química e de Materiais - PUC-Rio

Profa. Suzana Bottega Peripolli

Instituto SENAI Inspeção e Integridade

Prof. Luis Filipe Galvão dos Reis

ULisboa

Rio de Janeiro, April 18th, 2023.

All rights reserved. Total or partial reproduction of the work without the authorization of the author, advisor, and university is prohibited.

Maria Clara Carvalho Teixeira

She is graduated in Mechanical Engineering from the Pontifícia Universidade Católica of Rio de Janeiro (PUC-RJ). Later, she obtained a Master's degree through the Programa de Pós-graduação em Engenharia de Materiais e de Processos Químicos e Metalúrgicos da PUC-RJ under the thesis titled 'Comportamento do aço DIN 34CrNiMo6 em Fadiga de Altíssimo Ciclo.' Her academic research was focused on the fatigue behavior of materials, mainly Very High Cycle Fatigue. Currently, she works as a researcher in the field of Mechanical and Materials Engineering.

Bibliographic data

Teixeira, Maria Clara Carvalho

Fatigue failure assessment in ultrasonic test based on temperature evolution and crack initiation mechanisms / Maria Clara Carvalho Teixeira ; advisor: Marcos Venicius Soares Pereira. – 2023.

103 f. : il. color. ; 30 cm

Tese (doutorado)–Pontifícia Universidade Católica do Rio de Janeiro, Departamento de Engenharia Química e de Materiais, 2023.

Inclui bibliografia

1. Engenharia Química e de Materiais – Teses. 2. Fadiga de altíssimo ciclo. 3. Termografia infravermelha. 4. Microplasticidade. 5. FGA. 6. Aços estruturais. I. Pereira, Marcos Venicius Soares. II. Pontifícia Universidade Católica do Rio de Janeiro. Departamento de Engenharia Química e de Materiais. III. Título.

CDD: 620.11

Acknowledgements

First, to God for giving me life and the opportunity to do a PhD with patience, perseverance and dedication, especially resilience.

To my parents, Janice and Avelino and to my husband Renato for their support, love, patience and encouragement.

To my advisor Marcos Venicius Soares Pereira for his guidance, support and partnership.

To the members of the committee Professor Amanda Lemette Teixeira Brandão, Ana Rosa Fonseca de Aguiar Martins, Suzana Bottega Peripolli and Professor Luis Galvão dos Reis, for their availability and for having accepted the invitation to participate in the committee.

Profa. Amanda and DSc. Andrea for believing that it could work.

Profa. Suzana, Lincoln, Felipe, Talita from the SENAI ISI Inspection and Integrity for supporting me with the IR thermography.

To Isabel for scanning and transmission electron microscopy and EDS characterizations.

To Prof. Adrian for the partnership of all these years and for giving up the mechanical testing laboratory.

To Mr. José Felix Marques, technician responsible for machining the specimens.

To Carlos Senna and Prof. Rodrigo Prioli for allowing the use of the focused ion beam (FIB) equipment.

To the dear friends I acquired during this journey and will continue to be present in my life, Daiana, Fabiana, Juliana, João, Renan, Matheus, Mario, Rodrigo and Allan thank you for all your love, support and encouragement.

The partnership of colleagues Tiago Castro and Thiago Peixoto who have been with me since the beginning of my master's degree.

To CNPq and PUC-RIO, for the support granted, without which this work could not have been carried out.

This study was financed in part by the Coordenação de Aperfeiçoamento de Pessoal de Nível Superior - Brasil (CAPES) - Finance Code 001.

This research was developed within the scope of the Research and Technological Development of the Brazilian Electric Energy Sector Program regulated by ANEEL, with the support of the Eneva Companies - Pecém II Energy Generation S.A., Itaquí Energy Generation S.A., Parnaíba Energy Generation and Commercialization S.A. and Parnaíba II Energy Generation S.A.

Abstract

Teixeira, Maria Clara Carvalho; Pereira, Marcos Venicius Soares (Advisor). **Fatigue failure assessment in ultrasonic test based on temperature evolution and crack initiation mechanisms.** Rio de Janeiro, 2023. 103p. Tese de Doutorado - Departamento de Engenharia Química e de Materiais, Pontifícia Universidade Católica do Rio de Janeiro.

The determination of fatigue life to design structures and mechanical components is extremely important. The S-N curve can be affected by different operational conditions, and some factors are more pronounced under ultrasonic fatigue test, depending on the material. The influence of the high frequency in self-heating phenomena and frequency effect are discussed. A relevant aspect in VHCF is the mechanism of crack initiation and propagation. The fish-eye and fine granular area (FGA) phenomena were encountered on the fracture surfaces. This thesis is divided in 3 topics: temperature evolution, microplasticity strain amplitude, and investigation of the FGA region. The materials under study are DIN 34CrNiMo6 and DIN 42CrMo4 steel. Ultrasonic fatigue test was conducted at different intermittent driving and loading ratios, accompanied by an infrared thermographic camera. These results obtained by the thermographic camera were used to developed an artificial intelligence model using machine learning to predict the temperature-number of cycle curves based on the fatigue life. The model was able to predict the temperature and the coefficient of determination values to be above 0.98. In order to predict the fatigue life, parameters were selected based on stress, the traditional S-N curve, slope temperature at the beginning of the test, R_{θ} , heat dissipation, Q_{cyc} , and gradient temperature. A steady state temperature was reached approximately in $5E+04$ cycles with both steels. It is noticeable that the number of cycles to failure increases as slope temperature and heat dissipation decreases. R_{θ} provided better agreement with the experimental results followed by Q_{cyc} . Moreover, ultrafine grains in the cross-section of the FGA between 500 - 700 nm within the fracture surface were detected by FIB and EBSD analysis. “Local grain refinement” was choose the best model to explain FGA formation. The non-metallic inclusions were ultimately responsible for all internal crack initiations of Al_2O_3 .

Key-words

Very High Cycle Fatigue; Infrared Thermography; Microplasticity; FGA; Structural steels.

Resumo

Teixeira, Maria Clara Carvalho; Pereira, Marcos Venicius Soares. **Avaliação de falha por fadiga em teste ultrassônico com base na evolução da temperatura e mecanismos de iniciação de trincas.** Rio de Janeiro, 2023. 103p. Tese de Doutorado - Departamento de Engenharia Química e de Materiais, Pontifícia Universidade Católica do Rio de Janeiro.

A determinação da vida à fadiga para projetar estruturas e componentes mecânicos é extremamente importante. A curva S-N pode ser afetada por diferentes condições operacionais e alguns fatores são mais pronunciados no teste ultrassônico de fadiga, dependendo do material. A influência da alta frequência nos fenômenos de auto aquecimento e o efeito da frequência são discutidos. Um aspecto relevante em VHCF é o mecanismo de iniciação e propagação de trincas. Os fenômenos como olho de peixe e área fina granular (FGA) foram encontrados nas superfícies de fratura. Esta tese está dividida em 3 tópicos: evolução da temperatura, amplitude de deformação da micro plasticidade e investigação da região FGA. Os materiais em estudo são os aços DIN 34CrNiMo6 e DIN 42CrMo4. O teste de fadiga ultrassônica foi realizado em diferentes condições de carregamento no modo intermitentes e acompanhado por câmera termográfica infravermelha. Esses resultados obtidos para a câmera termográfica foram usados para desenvolver um modelo de inteligência artificial usando aprendizado de máquina para prever a curva temperatura-número de ciclos. O modelo foi capaz de prever a temperatura e os valores do coeficiente de determinação estão acima de 0,98. Para prever a vida à fadiga, foram escolhidos parâmetros baseados em tensão, curva S-N tradicional, temperatura no início do teste, R_{θ} , dissipação de calor, Q_{cyc} e gradiente de temperatura. A temperatura em estado estacionário foi atingida em aproximadamente $5E+04$ ciclos em ambos os aços. Observa-se que o número de ciclos até a falha aumenta à medida que a inclinação da temperatura (fase I) e a dissipação de calor diminuem. R_{θ} forneceu melhor concordância com os resultados experimentais seguido por Q_{cyc} . Além disso, grãos ultrafinos na seção transversal do FGA entre 500 - 700 nm dentro da superfície da fratura foram detectados pela análise FIB e EBSD. O “local grain refinement” foi escolhido como o melhor modelo para explicar a formação de FGA. As inclusões não metálicas Al_2O_3 foram responsáveis por todas as iniciações internas da trinca de fadiga.

Palavras chave

Fadiga de Altíssimo Ciclo; Termografia Infravermelha; Microplasticidade; FGA; Aços Estruturais.

Table of contents

1 Introduction.....	20
2 Fatigue	22
3 Background of VHCF	25
3.1 Brief History.....	25
3.2 Ultrasonic Fatigue Testing.....	27
3.3 VHCF Interpretations.....	30
3.3.1 VHCF behavior of engineering materials.....	30
3.3.2 Fracture mechanisms	33
3.3.2.1 Empirical Equations.....	43
3.3.3 Temperature and Frequency Effects	44
4 Temperature Application to Predicted the Fatigue Life.....	47
5 Microplasticity.....	50
6.1 Materials.....	51
6.2 Experimental Procedure	52
6.2.1 Calibration	53
6.2.2 VHCF with Thermographic Test	55
6.2.3 Ultrasonic Fatigue tests.....	57
6.2.4 Metallography.....	59
6.2.5 Scanner Electron Microscopy (SEM) and Focused Ion Beam (FIB).....	59
7 Results and Discussion	60
7.1 Microstructure and Inclusions.....	60
7.2 Experiments and Computational T-N curve.....	62
7.2.1 Experimental Results.....	62
7.2.2 Artificial Intelligence modeling to predict the temperature increase.....	64
7.3 S-N curve	67
7.4 T-N curves.....	73
7.5 Fatigue Damage Parameters	75
7.5.1 R_e	75
7.5.2 Q_{cyc}	76

7.5.3 ΔT	78
7.6 Microplasticity.....	80
7.7 Fracture surfaces	82
8 Conclusions.....	91
9 Suggestions for future work	93
10 References	95
Appendix A.....	101
Appendix B.....	101

List of Figures

Figure 1: Schematic of cyclic loading with nomenclature (adapted by [2]).	22
Figure 2: Conventional S-N curve (adapted by [4]).	24
Figure 3: S-N curve with 3 domains: 1- LCF, 2: HCF, 3: VHCF [11-12].	24
Figure 4: Examples of some applications that have service life beyond 10^8 cycles [adapted from 5].	26
Figure 5: Illustration of mechanical resonance system adapted from [29].	28
Figure 6: Ultrasonic specimen geometry [5].	28
Figure 7: Schematic diagram of materials type I [27-33].	31
Figure 8: Schematic diagram of materials type II [27-33].	32
Figure 9: Schematic diagram of materials type II proposed by Pyttel et al. [34].	33
Figure 10: Illustration of the mechanism of fatigue crack initiation site [33].	33
Figure 11: Different stages of the VHCF fracture surface [40].	35
Figure 12: a) typical fish-eye fracture surface of internal inclusion in steel 4240; b) detail of the inclusion responsible by internal nucleation [20].	35
Figure 13: FGA fracture surface nearby the non-metallic inclusion (adapted by [43]).	36
Figure 14: Schematic with different morphologies in the fracture surface [adapted by 42].	37
Figure 15: Steps of the FGA formation [37,39].	38
Figure 16: Fractography of the hydrogen trapped around the non-metallic inclusion [adapted by 6].	38
Figure 17: A schematic drawing of ODA formation mechanism [6,43-46].	39
Figure 18: Illustration the cross section of mechanism that conduct the GBF formation [adapted by 39]: a) microstructure before the crack initiation, b) initiation of the micro cracks and coalescence, c) complete GBF facet.	39
Figure 19: Schematic drawing of NCP model with 4 steps to complete the FGA formation after millions cycles [48]: a) crack initiation, b) nanograins layer, c) appear the rough aspect and d) complete formation of FGA.	40
Figure 20: Mechanism of the FGA formation [24]: (a) microstructure before the crack nucleation, (b) local grain refinement, (c) crack nucleation and propagation along the grain refinement, (d) local grain refinement at crack tip, (e) crack propagation and (f) FGA.	42
Figure 21: Fracture surface of tested specimen in ultra high frequency [56].	45
Figure 22: S-N curve of low carbon steel under different loading frequencies [67].	46
Figure 23: Theoretical T-N curve [adapted by 74].	47

Figure 24: Illustration the temperature evolution with the applied σ_a (adapted by [75])	48
Figure 25: Hourglass specimens and its dimensions for testing in fully reversed conditions.	53
Figure 26: a) Calibration instrument, b) the signal captured the amplitude and c) oscillation (peak to peak value).	54
Figure 27: a) Illustration of the ultrasonic fatigue machine USF2000A and IR camera model FLIR A655SC [6]. b) Thermogram of the specimen surface. .	56
Figure 28: Software used to control the test.	57
Figure 29: USF 2000A from LABFADAC used to performed the tests: a) $R=-1$ and b) $R \neq -1$	58
Figure 30: a) SEM/EBSD from mechanical department and b) FIB form physics department, both from PUC-Rio.	60
Figure 31:Micrograph of: a) DIN 34CrNiMo6 and b) DIN 42CrMo4.	61
Figure 32: Fractographics obtained by optical microscopic and digital image program ImageJ.	61
Figure 33:Thermal gradients of: a) 30% $\sigma_u = 270$ MPa and b) 35% $\sigma_u = 315$ MPa.	63
Figure 34:Thermal gradients of: a) 40% $\sigma_u = 360$ MPa and b) 45% $\sigma_u = 405$ MPa.	63
Figure 35: Thermal gradients of 30 and 40% σ_u in 110-500 msec with and without cooling.	63
Figure 36:Scatter plots of train model: a) comparison predicted and observed T and b) T-N curve.	64
Figure 37:Scatter plots of test model: a) comparison predicted and observed T and b) T-N curve.	64
Figure 38:Model performance from the R^2	65
Figure 39:SHAP method: a) feature importance and b) summary plot.	67
Figure 40:S-N for DIN 34CrNiMo6 steel.	68
Figure 41:S-N for DIN 42CrMo4 steel.	69
Figure 42: Comparative analysis of predicted life vs. experimental life of DIN 34CrNiMo6.	70
Figure 43:Comparative analysis of predicted life vs. experimental life of DIN 42CrMo4.	71
Figure 44:S-N curves of DIN 34CrNiMo6 for different loading ratios.	72
Figure 45:S-N curves of DIN 42CrMo4 for different loading ratios.	72
Figure 46:T-N curves until $5E+05$ cycles of DIN 34CrNiMo6.	73
Figure 47:T-N curves until $5E+05$ cycles of DIN 42CrMo4.	74
Figure 48:Bars diagram R_e versus σ_a	75
Figure 49: R_e vs N_f	76
Figure 50:Comparative analysis of predicted life and experimental life of a) DIN 34CrNiMo6 and b) DIN 42CrMo4.	76
Figure 51: Q_{cyc} vs. N_f	77

Figure 52:Comparative analysis of predicted life and experimental life of a) DIN 34CrNiMo6 and b) DIN 42CrMo4.	77
Figure 53: ΔT vs. N_f	79
Figure 54:Fracture surface with crack initiation at the surface.....	83
Figure 55:Subsuperficial crack initiation from non-metallic inclusions.	84
Figure 56: Fisheye image by backscattered electrons detector.....	84
Figure 57: FGA region: a) 1000 x, b) 5000 x.	85
Figure 58: a)Fracture surface with crack initiation from the interior inclusion, b) highlighted of FGA and inclusion, c) aspect of fish-eye surface and d) aspect of FGA surface.....	86
Figure 59: a) Entire fracture surface, b) crack initiation site of a), c) image of crack initiation site by backscattered electrons and d) the same of c) obtained by secondary electrons.	87
Figure 60: EDS of DIN42CrMo6.....	88
Figure 61: a) fracture surface with the cross made nearby the surface and b) cross-section of the specimen.	89
Figure 62: a) fracture surface obtained with FIB analysis, b) lamella.	90
Figure 63: a) lamella of FGA regions after EBSD analysis (Euller map).	91

List of Tables

Table 1: Time demand of ultrasonic and conventional fatigue test [6-8,26]...	27
Table 2: Chemical composition with the main elements.	51
Table 3: Mechanical properties of the steels under study.	52
Table 4: Parameters of the fatigue experiments[26].	56
Table 5: Model comparison performance over MAE, R^2 , R^2_{adj} , MSE and RMSE.	65
Table 6: presents the stress applied and respective number of cycles to failure of DIN 34CrNiMo6.	69
Table 7: presents the stress applied and respective number of cycles to failure of DIN 42CrMo4.	70
Table 8: Data obtained from T-N curves of DIN 34CrNiMo6.	74
Table 9: Data obtained from T-N curves of DIN 42CrMo4.	74
Table 10: Constant ϕ Fargione' s equation.	79
Table 11: Microplasticity strain amplitude of DIN 34CrNiMo6 results.	80
Table 12: Microplasticity strain amplitude of DIN 42CrMo4 results.	80
Table 13: Results at low frequency test.	81
Table 14: Cyclic strain rate.	81

List of Abbreviations and Symbols

VHCF – very high cycle fatigue

S – stress

N – number of cycles

BCC - body centered cubic

FGA - fine granular area

T – temperature

SEM - scanning electron microscope

SIF – stress intensity factor

FIB - focused ions beam

σ_{max} - maximum stress

σ_{min} - minimum stress

$\Delta\sigma$ - stress range

σ_a - stress amplitude

σ_m - mean stress

R - load ratio

N_f - number of cycles to failure

LCF - Low cycle fatigue

σ_u - ultimate strength

σ_y - yield strength

HCF - High cycle fatigue

L_1 - resonance length

E – elasticity modulus

ρ - density

f - resonance frequency

c - wave velocity

σ – stress

α, β – geometries parameters
 x - the axial distance along the reduce section part
 A_0 - displacement amplitude at the ends of the specimen
 PSB - persistent slip bands
 ΔK_{th} - stress intensity factor threshold of the material
 ODA - optically dark area
 GBF - granular bright facet
 NCP - numerous cyclic pressing
 SIF - stress intensity factor
 K_{max} - maximum SIF
 $K_{th,global}$ - global SIF threshold
 $K_{th,local}$ - local SIF threshold
 HV - Vickers hardness
 C – constant value of crack initiation site
 FCC - face-centered cubic
 T_0 - room temperature
 T_s - steady state temperature
 c_p - specific heat capacity
 c_1, c_2 – constants of $R_\theta - N_f$
 $\varepsilon_{a,e}$ - elastic portion
 $\varepsilon_{a,p}$ - plastic parcel
 ε_f - fatigue ductility coefficient
 σ_a^μ - microscopic stress tensor
 $\varepsilon_{a,p}^\mu$ - plastic strain tensor
 μ - shear modulus
 ξ - the constant parameter
 $d1$ - energy dissipation
 β - is dependent of the Poisson's ratio ν .

f_{eff} - frequency effective

RT - room temperature

EBSD - electron backscatter diffraction

R^2 - performance metric

Y - dependent variable

Xs - independent variables

R^2_{adj} - adjusted coefficient of determination

MAE - mean of absolute error

MSE – mean of squared error

RMSE - root mean of squared error

SHAP - Shapley additive explanations

$N_{f, pre}$ - predicted life

$N_{f, exp}$ - experimental life

$\dot{\epsilon}$ – cyclic strain rate

*If you want to find the secrets of the universe,
think in terms of energy, frequency and
vibration.*

Nikola Tesla

1 Introduction

The determination of fatigue life to design structures and mechanical components is extremely important. The evaluation of very high cycle fatigue (VHCF) makes it possible to reach high numbers of cycles, which is equivalent to the useful life of the components in service.

Traditionally, the fatigue life is estimated using the S-N curve, a method developed by Wöhler that is simple to apply and well established in the literature. However, the S-N curve can be affected by different operational conditions e.g. temperature, geometries, environment and surface finish. Some factors are more pronounced under ultrasonic fatigue test, depending on the material. The influence of the high frequency in the temperature of the specimen during the test and the fatigue strength of the materials are a complex subject. Moreover, frequency effect for specific steels such as BCC (body centered cubic) suffer more influence, resulting in a greater fatigue strength than in low frequency tests. One of the reasons may be related to a low movement of dislocations.

Another relevant aspect in VHCF is the mechanism of crack initiation and propagation. The fish-eye and fine granular area (FGA) phenomena are encountered in the fracture surface of the metallic materials. These features only occur when the crack initiation is within the specimen. The FGA phenomenon is only observed in the VHCF regime. Different models were developed in order to explain the roughness aspect observed in the FGA region, yet this is still not well established. The FGA region is usually related to the stress intensity factor threshold, which is an important parameter in terms of the fail-safe concepts of the material. In this study, five of the main models, judged by the author, are scrutinized: fine granular area, optically dark area, granular bright facet, number of cycles pressing and local grain refinement.

Fatigue damage based on temperature evolution is also explored. The temperature evolution during fatigue test is represented as a T-N curve which is divided in three phases: phase I, when the temperature increases until it achieves the steady state temperature in phase II, and in some cases phase III, which represents the temperature surge at the end of the fatigue test. Heat dissipation is introduced, depending on the temperature increase in the beginning of the test.

Microplasticity strain amplitude was calculated using Coffin-Manson-Basquin and localization and homogenizations law.

Aiming to discuss the operational factors and failure mechanism in VHCF behavior, this present study proposes an ultrasonic fatigue experimental test of two steels widely used in the mechanical components design, DIN 34CrNiMo6 and DIN 42CrMo4. Additionally, artificial intelligence modeling was used to predict the temperature during the test, based on the thermographic results obtained from different operational conditions. FGA and fish-eye features were identified. A scanning electron microscope (SEM) and were utilized in order to estimate the diameter of each phenomenon related to the stress intensity factor (SIF). A focused ions beam (FIB) were used to verify the fine grains in the cross-section of FGA.

2 Fatigue

Fatigue, in engineering terms, is a progressive damage of materials under repeated cyclic loads. It is the predominant failure in engineering systems, and studies in this area can determine the root cause of failure and save countless lives. Fatigue process can be classified as: mechanical fatigue controlled by stresses and strains; creep fatigue which consists of cyclic loads at high temperatures; thermal fatigue related to cyclic changes in the material temperature; thermo-mechanical fatigue, which is a combination of mechanical and thermal fatigue; corrosion fatigue, where cyclic loads are applied in the presence of a chemically aggressive/environment; contact fatigue caused by stress generated due to the contact of two bodies subjected to cyclic loading; fretting fatigue due to cyclic stresses together with the oscillatory motion and frictional sliding between surfaces [1].

This mechanical failure is characterized by crack nucleation, due to accumulation of small plastic deformations in a critical point of the component/material, which propagates with continued cyclic load applications [1-3]

The cyclic load consists in a harmonic function composed of a maximum stress (σ_{max}), minimum stress (σ_{min}), stress range ($\Delta\sigma$), stress amplitude (σ_a), mean stress (σ_m) and load ratio (R), which are present in Figure 1 and represented by Equations (1) to (4) [1-3].

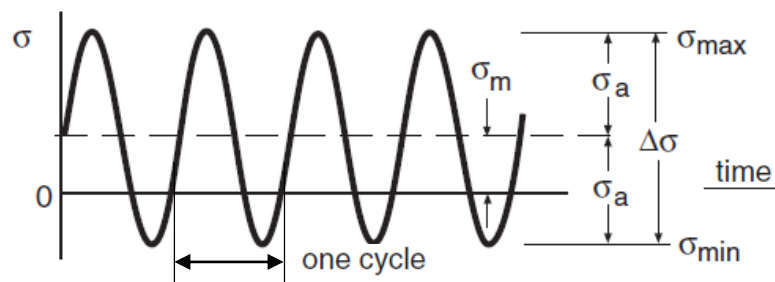


Figure 1: Schematic of cyclic loading with nomenclature (adapted by [2]).

Where,

$$\Delta\sigma = \sigma_{max} - \sigma_{min} \quad (1)$$

$$\sigma_a = \frac{\sigma_{max} - \sigma_{min}}{2} \quad (2)$$

$$\sigma_m = \frac{\sigma_{max} + \sigma_{min}}{2} \quad (3)$$

$$R = \frac{\sigma_{min}}{\sigma_{max}} \quad (4)$$

Traditionally, the fatigue life is estimated using the Stress-Number of cycles (S-N) curve and it was often classified into different regimes according to the number of cycles to failure (N_f) [1-3]. Until the 21st century, S-N was divide in two regimes:

- Low cycle fatigue (LCF) comprehending stress values between the ultimate strength (σ_u) and yield strength (σ_y) of the material. It is characterized as a short fatigue life and the failure is controlled by deformations.
- High cycle fatigue (HCF) where the fatigue life is up to 10^4 cycles and stress values are below the σ_y . In this case there are no observed macroscopic plastic deformations, and the failure is controlled by stress.

Figure 2 present the conventional S-N curve with the endurance limit (dashed line). When the material reaches the endurance limit or fatigue limit, which is when the curve becomes a horizontal asymptote, it was assumed that the material would withstand an infinite number of cycles for a given stress level. Generally, it occurs in $10^6 - 10^7$ cycles and the material does not fail. It is noteworthy that for non-ferrous metallic materials the endurance limit is not observed [1-4].

In the last 25 years, with the new testing technique using high frequency close to 20 kHz, researchers have shown that metallic materials continue to fail to stresses below the endurance limit and for a number of cycles that were previously unreachable [5-13]. In this context, the S-N curve was extended and a third regime was created, namely the “gigacycle fatigue”, “ultra high cycle fatigue” or “very high cycle fatigue”, with the third designation being the most common. Very high cycle fatigue (VHCF)

comprehend fatigue lives that exceeds 10^7 cycles. Figure 3 illustrates the extended S-N curve.

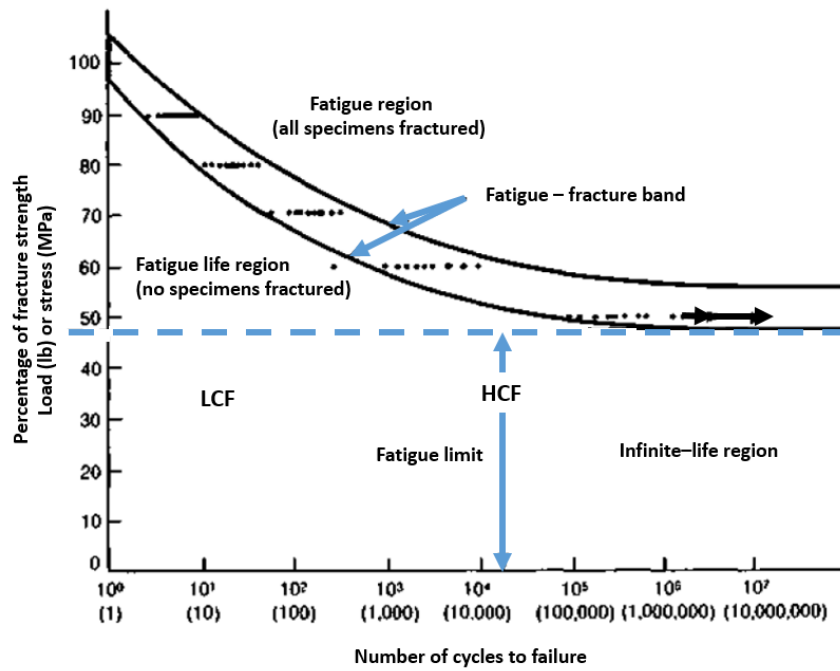


Figure 2: Conventional S-N curve (adapted by [4]).

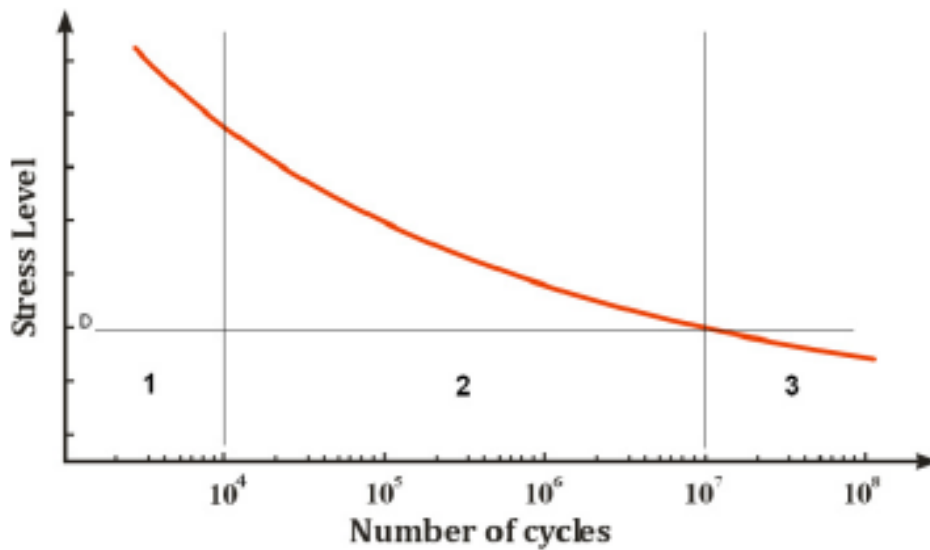


Figure 3: S-N curve with 3 domains: 1- LCF, 2: HCF, 3: VHCF [11-12].

3 Background of VHCF

3.1 Brief History

The concept of ultrasonic fatigue testing came into effect almost a decade after the beginning of the last century when the first resonance system of 116 Hz was developed by Hopkinson [14] in 1911; at that time the highest fatigue testing frequency of a mechanically driven system did not exceed 33 Hz. In 1925, Jenkin [15] crossed the 1 kHz frequency border using a similar procedure Hopkinson's technique. Later in 1929, Jenkin and Lehman [16], using a pulsating air resonance system, reached a frequency of 10 kHz. Then in 1950, Manson [17] made a relevant development in ultrasonic fatigue testing technique by using high power ultrasonic waves to induce materials fatigue by introducing piezoelectric transducers. Therefore, it was possible to transform 20 kHz electrical signals into mechanical vibrations of the same frequency. Later, Girard [18] (1959, 92 kHz) and Kikukawa [19] (1965, 199 kHz) also contributed to higher frequencies for fatigue testing developments. However, the modern ultrasonic equipment continues to be based on the Manson's model [5,6-11].

Advances in ultrasonic fatigue testing was started by Bathias (France) and Stanzl–Tschegg (Austria). Bathias left several important contributions in the field of very high cycle fatigue: development of data acquisition system for ultrasonic fatigue testing [5], in 1994, in cooperation with T. Wu and J. Ni; he did many experimental tests and the results can be found in his book [5]; chairman of the first conference on very high cycle fatigue (International Conference Euromech 382: Fatigue Life in Gigacycle Regime – VHCF 1) in 1998, in collaboration with Stanzl–Tschegg; the pioneer researcher in materials fatigue limit in Gigacycles with an important statement “There is no infinite fatigue life for metallic materials”[20-23]; the first one to propose standard specimen tests.

Most VHCF testing is performed under uniaxial condition, with constant and variable amplitude loads. However, Vieira and co-authors [24, 25] report VHCF tests carried out under multiaxial condition, making use of a self-designed device for ultrasonic fatigue which combines axial and torsional loads through a single piezoelectric transducer.

The development of the ultrasonic fatigue machine made it possible to perform tests of a very long life ($N > 10^7$ cycles). Fatigue life of several engineering components has been increased beyond 10^8 load cycles. A number of examples in that respect can be found in applications with aircraft, automobile, railway and energy industries (Figure 4). The high frequency, usually 20 kHz, makes it possible to reproduce the service life in a considerably lower test time [5-13]. Table 1 presents the time demands for fatigue testing with low frequency and high frequency considering continuous loading.

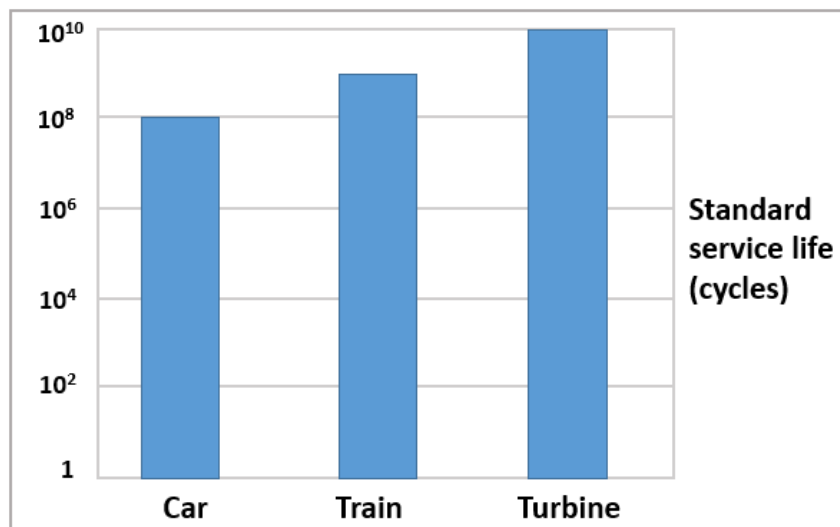


Figure 4: Examples of some applications that have service life beyond 10^8 cycles [adapted from 5].

Table 1: Time demand of ultrasonic and conventional fatigue test [6-8,26].

Number of cycles	Ultrasonic (20 kHz)	Conventional (100 Hz)
10^7	9 minutes	30 hours
10^8	1.4 hours	12 days
10^9	14 hours	4 months
10^{10}	6 days	3 years

3.2 Ultrasonic Fatigue Testing

Ultrasonic fatigue testing consists in a high frequency generator and a piezoelectric actuator which convert the ultrasonic electrical signal in ultrasonic waves of the same frequency, making the specimen to vibrate in a certain resonance [5-13,27,28].

The basic structure is composed of four main elements: ultrasonic generator, piezoelectric actuator, horn and data acquisition system. Figure 5 shows the mechanical resonance system of the equipment where (1) is the piezoelectric actuator, (2) booster, (3) horn and (4) specimen. The piezoelectric actuator is responsible for the resonance system, where a longitudinal sinusoidal vibration is transmitted to the booster and subsequently to the horn, which increases the amplitude vibration and sends it to the specimen. The behavior in the stress-displacement field is also presented in figure 1. It can be observed at points (a) and (b), at the ends of the specimen, that stress is minimum (stress nodes) and displacement is at maximum, while at the center of the specimen we observe maximum stress and zero displacement (displacement node). At point (c), between the booster and horn, there is the third stress node (zero stress) [5-8,26].

As previously mentioned, the specimen in VHCF test vibrate in resonance, which is different from the conventional fatigue tests. The frequency supplied by VHCF machine should be the same one of the natural frequencies of the specimen [5]. In other words, the specimen is tested in free vibration. The specimen geometry is obtained from the ultrasonic fatigue principles based on the elastic wave theory.

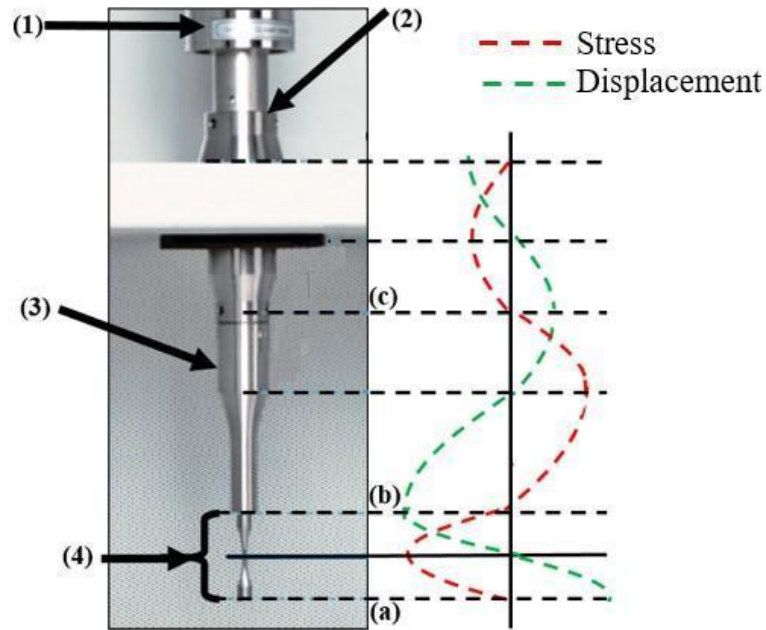


Figure 5: Illustration of mechanical resonance system adapted from [29].

To obtain the resonance length (L_1) it is necessary to know the elasticity modulus (E) and the density (ρ) of the material. The specimen's resonance length will ensure that the specimen will be cycling at the same frequency as the ultrasonic fatigue system. The usual specimen design has an hourglass shape, and its length is obtained according to Equations 5 to 9. The ultrasonic specimen geometry can be observed in Figure 6 [5-13].

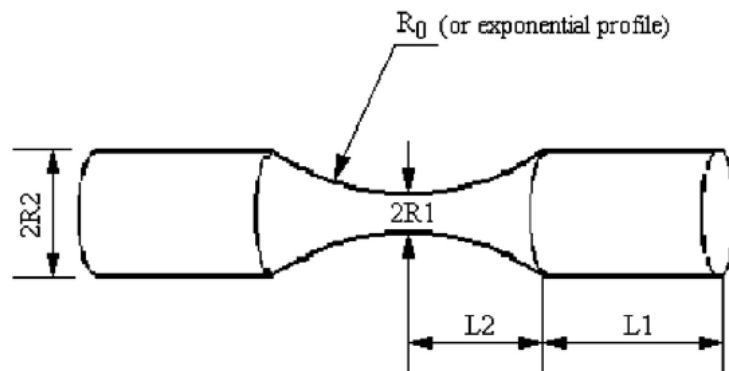


Figure 6: Ultrasonic specimen geometry [5].

$$L_1 = \frac{1}{k} \arctan \left\{ \frac{1}{k} [\beta \coth(\beta L_2)] - \alpha \tan(\alpha L_2) \right\} \quad (5)$$

where,

$$\alpha = \frac{1}{L_2} \operatorname{arccosh} \left(\frac{R_2}{R_1} \right) \quad (6)$$

and

$$\beta = \sqrt{\alpha^2 - k^2} \quad (7)$$

where,

$$k = \frac{2\pi f}{c} \quad (8)$$

and

$$c = \sqrt{\frac{E_d}{\rho}} \quad (9)$$

Where, f and c are resonance frequency and wave velocity, respectively.

Knowing the dimensions of the specimens and α, β parameters, it is possible to calculate the stress (σ) for the reduced section part. The σ is described in Equation (10).

$$\sigma(x) = EA_0 \varphi \frac{[\beta \cosh(\beta x) \cosh(\alpha x) - \alpha \sinh(\beta x) \sinh(\alpha x)]}{\cosh^2(\alpha x)} \quad (10)$$

where,

$$\varphi(L_1, L_2) = \frac{\cos(kL_1) \exp(\alpha L_2)}{\sinh(\beta L_2)} \quad (11)$$

and x is the axial distance along the reduce section part, with A_0 representing the displacement amplitude at the ends of the specimen.

3.3 VHCF Interpretations

Materials with high performance are quite often studied because such materials possess a vast application in several industries. The ultrasonic fatigue testing machine allows for many studies of different metallic materials to investigate the fatigue properties in VHCF region.

3.3.1 VHCF behavior of engineering materials

The first published studies focused mainly on high strength steels and presumed that the S-N curve can exhibit a duplex curve or stepwise [6-12,27-33]. Mughrabi [30-32], proposed a schematic diagram with multistage for the fatigue lives and distinguished the VHCF properties of metallic materials in two types:

- Type I: Ductile, homogeneous, single-phase face metals and alloys besides low carbon steel, cast iron and some stainless steels. Essentially, metal which does not contain inclusions. The S-N curve presents a gap of fatigue strength lower than 50 MPa between 10^6 and 10^9 cycles.
- Type II: Most high strength steels and other materials that contain heterogeneities like inclusions and pores. The fatigue strength goes up to 50 MPa between 10^6 and 10^9 cycles.

The diagrams, presented in Figure 7 and 8, were proposed by Mughrabi and described in four stages, from short to very long lives regarding the metallic materials. In Figure 6, I – range is characterized by LCF regime, where persistent slip bands (PSB) are formed after a certain number of cycles; II – HCF range, considering the PSB

threshold of stress and strain amplitudes (the value of plastic strain amplitude - $\Delta\varepsilon_p/2 \approx 2.5 \times 10^{-5}$ was obtained for copper [30]). III – VHCF range. The accumulation of irreversible slip is slight (the deformations are more reversible) and result in increased roughness on the surface, inducing the crack initiation. Only when the irreversible threshold is reached is the real fatigue limit considered. The stress amplitude is too small, and makes it difficult to create the PSBs. [9-11,30-33].

Figure 8 illustrates the double S-N curve of materials type II. Mughrabi proposed this schematic based on the Wöhler diagram. Regions I and II describe the traditional S-N curve, representing I LCF regime and II HCF regime, with crack initiation mostly occurring on the surface. The third region comprehends the VHCF regime, with stress amplitudes below the “conventional” endurance limit. The crack initiation occurs typically from internal defects [9-11,30-33].

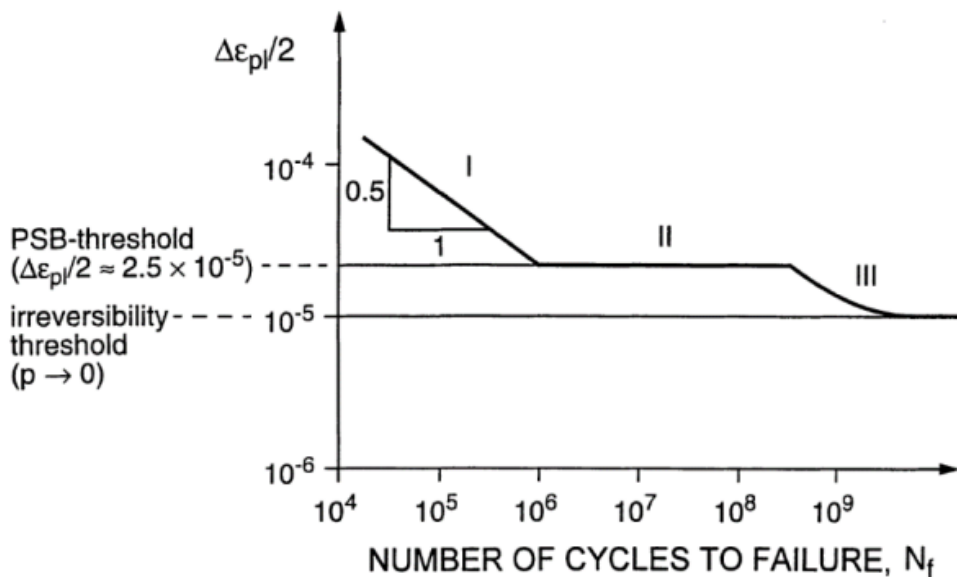


Figure 7: Schematic diagram of materials type I [27-33].

Region IV, as presented in Figure 8, promoted controversial discussions among researchers about the existence of a “real” fatigue limit. Based on this, Pyttel et al. [34], proposed a new schematic for type II materials, as shown in Figure 9. This diagram is more general and presented the regimes and typical crack initiation for each region. Region I is LCF regime, where crack initiation can occur in several sites on the

specimen's surface simultaneously. As local cyclic hardening takes place, PSBs are also formed. Region II (between 10^5 and 10^7 cycles) corresponds to the high cycle fatigue regime (HCF), where failure occurs due to microscopic yielding and crack initiation is usually limited to the specimen's surface. Regions I and II represented by curve (1) is the traditional Wöhler diagram [27-33].

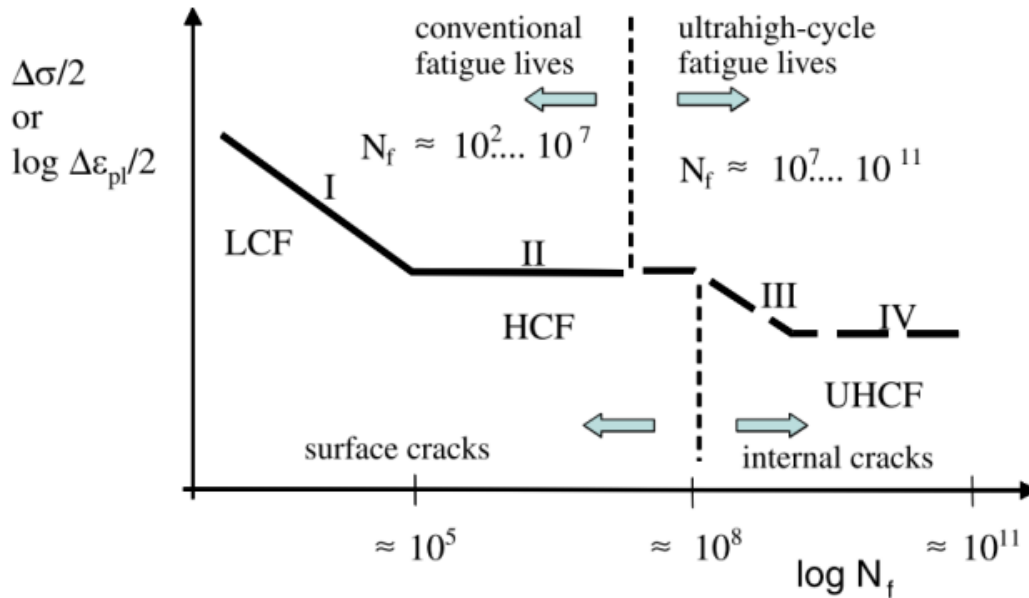


Figure 8: Schematic diagram of materials type II [27-33].

Concerning VHCF (region III), fatigue life extends beyond 10^7 cycles, with the failure mechanism governed by stresses lower than the σ_y of the material. The cracks can initiate from internal defects of the specimen, such as non-metallic inclusions. VHCF experiments reveal that most materials do not have their fatigue limit at 10^7 cycles, but instead begin decreasing gradually as fatigue life reaches $10^8 - 10^{10}$ load cycles. Region IV highlights the questioning about the existence of a real fatigue limit.

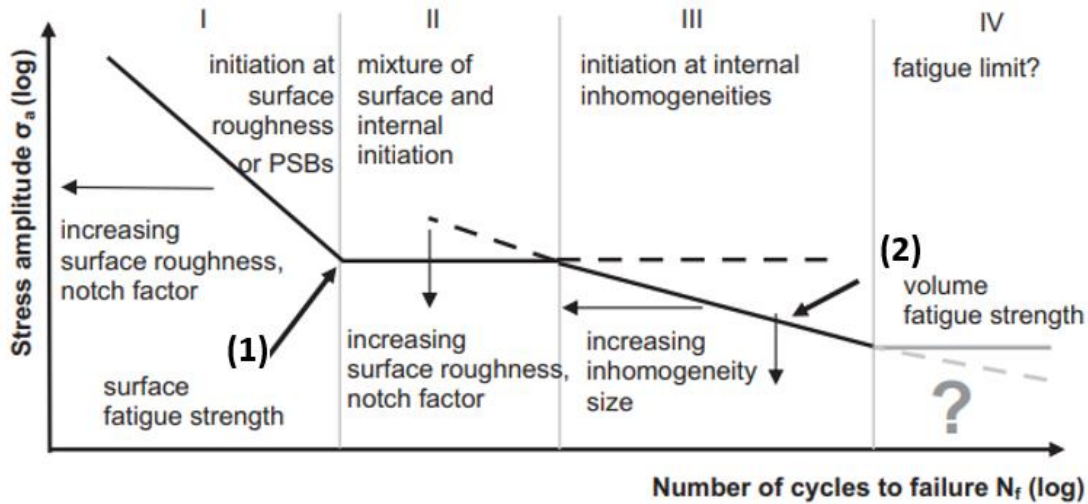


Figure 9: Schematic diagram of materials type II proposed by Pyttel et al. [34].

3.3.2 Fracture mechanisms

According to the literature [5-9,33], when the stress amplitude decreases with the increasing number of cycles to failure, the fatigue crack initiation can migrate from the surface to internal areas, indicating that in VHCF regimes the material can be more sensitive to internal defects. Most of internal crack initiation originate at non-metallic inclusions. In Figure 10, the transition of the crack initiation site as it goes from LCF to VHCF is made more evident.

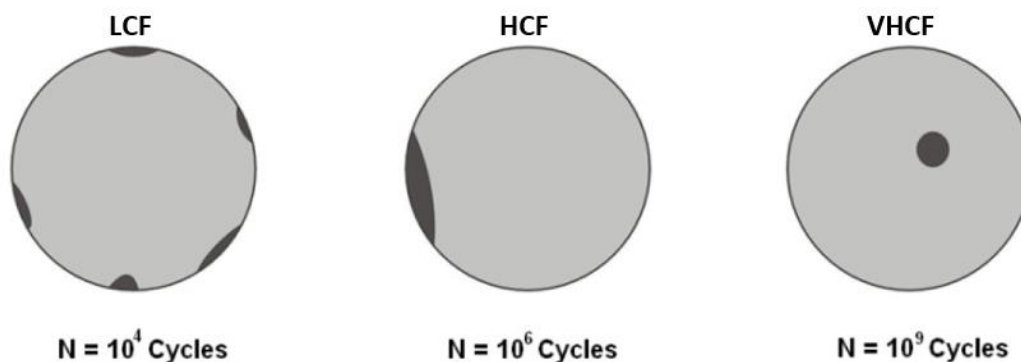


Figure 10: Illustration of the mechanism of fatigue crack initiation site [33].

In LCF regime, the specimen is under macroscopic plastic deformations and multiple cracks are nucleated at the surface due to PSBs. At 10^6 cycles, in HCF regime, only one crack initiation site is detected, while for VHCF regimes, internal or subsurface cracks can initiate from internal inclusions, which act as stress concentrators and promote more slip than cyclic slip at surface level [5-11].

According to Bathias and Paris, the mechanism behind the shift of crack initiation from the surface to interior of the metallic material relies on three main factors, namely the anisotropy of metals, stress concentration and statistical conditions. Nevertheless, the crack initiation site depends on the stress levels and size of potential sites [5,20,23,34]. It is a competition between the surface and the interior.

An important characteristic when the crack initiation occurs from a defect within the material matrix is the phenomenon called “fish-eye”. Fish-eye is a feature of the crack growth stage. It could be defined as a circular crack propagation, presenting a smooth surface compared to other regions in the fracture surface. These phenomena occur mainly in high strength steels and result in a fracture surface with four stages for crack formation, as presented in Figure 11. The (i) stage corresponds to the crack initiation site, (ii) a crack growth into the fish-eye, (iii), crack growth outside the fish-eye as conventional fatigue test and (iv) final fracture [5-11,35].

It is imperative to point out that the fish-eye feature was reported by Ohuchida for the first time in 1961. He suggested that fish-eye appear in the fracture surface of metallic materials which possess higher hardness on the surface [38]. He related in his experiments that the fish-eye could not appear in the fracture surface for specimens with hardness below 550 HV. Nonetheless, this phenomenon was made evident when ultrasonic fatigue tests began taking place.

Kazymyroyich, V. et al. [6-8,39], describe the fish-eye as slower fatigue crack propagation. He compared the striations inside and outside the fish-eye region and observed that the distance of each striation is shorter than outside the fish-eye.

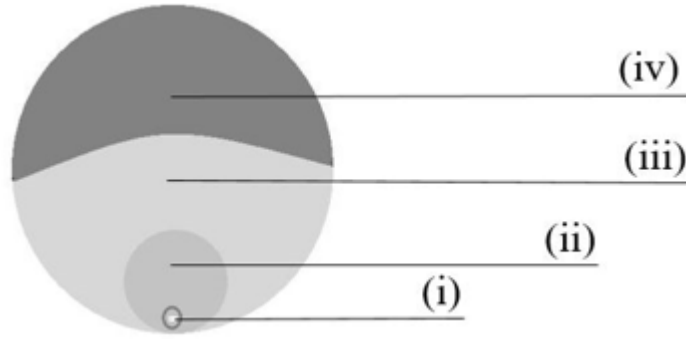


Figure 11: Different stages of the VHCF fracture surface [40].

There is no apparent relation between the fish-eye size increase and the increasing number of cycles or the decreasing stress amplitude. The more internal the defect that originates the crack initiation is, the bigger the fish-eye will be. This occurs because the fish-eye reaches its maximum size when its boundary is tangent with the specimen's surface. When this occurs, the material identifies as a defect on the surface and continues to grow, as observed in conventional fatigue tests [39,41]. Typically, the fish-eye diameter is between 0.5 and 1 mm [6]. Figure 12 displays the fish-eye phenomenon.

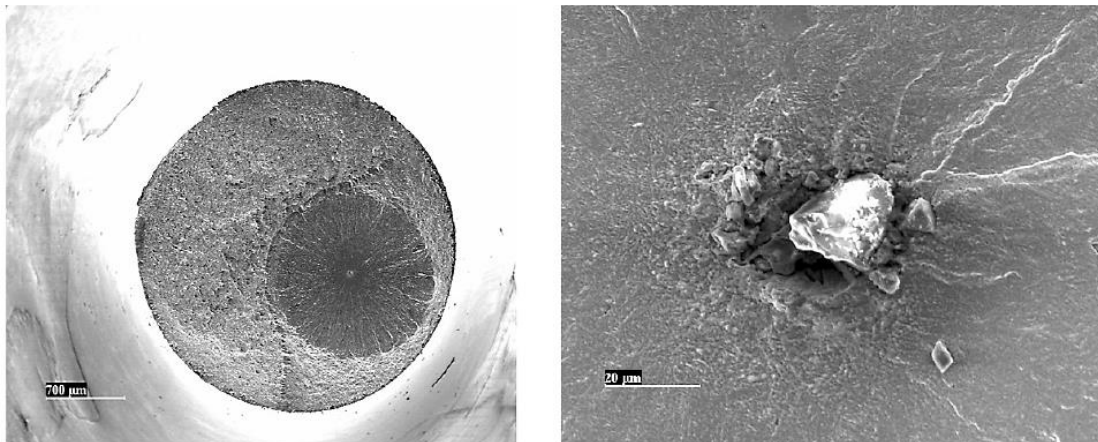


Figure 12: a) typical fish-eye fracture surface of internal inclusion in steel 4240; b) detail of the inclusion responsible by internal nucleation [20].

An additional phenomenon observed in VHCF regime is the so-called fine granular area (FGA). This feature is sited inside the fish-eye, nearby the internal defect which is responsible for the internal crack nucleation. The FGA fracture surface exhibits a rough appearance juxtaposed with the fish-eye region. This aspect can be more clearly observed in Figure 13. The formation mechanism of the FGA feature has been interpreted discrepantly among different researchers, with several theories being proposed to describe its origin. It is consolidated that the FGA formation consumes more than 95% of the fatigue life, with its size relating to the stress intensity factor threshold of the material (ΔK_{th}) and surging with the increase of fatigue life [43,66,67].

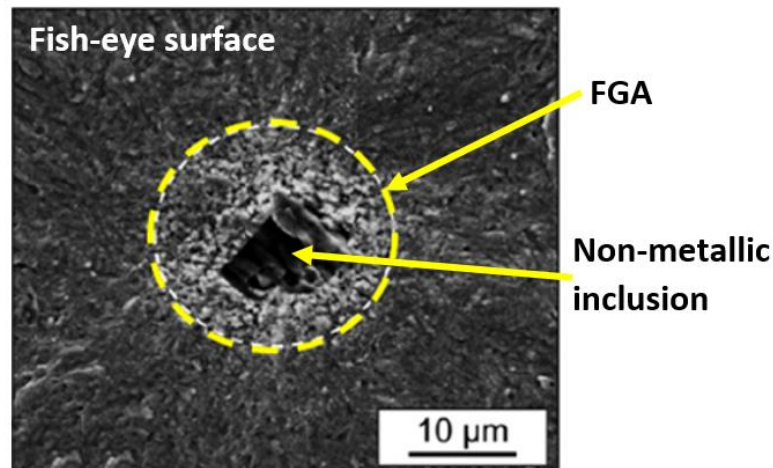


Figure 13: FGA fracture surface nearby the non-metallic inclusion (adapted by [43]).

It is paramount to emphasize that there is still no answer about which mechanism takes place to create the FGA. Figure 14 presents a schematic with the different morphologies along the fracture surface if the crack initiation was induced by a non-metallic inclusion or another internal defect. Five of the main existing models will be further analyzed in the subsequent paragraphs.

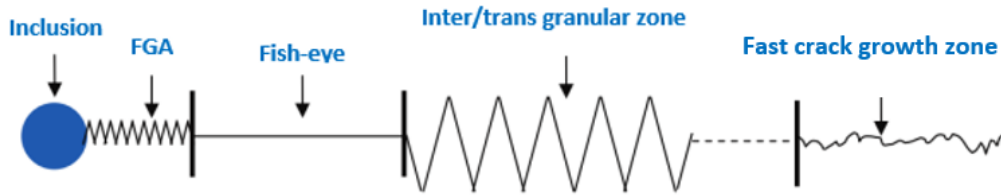


Figure 14: Schematic with different morphologies in the fracture surface [adapted by 42].

Sakai, T. et al. called the rough aspect in the fracture surface a fine granular area, as previously mentioned. The presented model suggested that the driving force behind the FGA formation is the polygonization mechanism and the debonding between inclusion and metal matrix. Figure 15 illustrated the stages of FGA formation. A microscale polygonization mechanism starts during the VHCF process and forms the FGA (Stage A). In the second stage the nucleation and coalescence of micro-debondings (fine sub grains boundaries) occurs. In Stage C, the micro-debondings spread over the FGA. After a long loading cycle, its formation is completed [35,37].

Murakami, Y. proposed one of the earliest models, called optically dark area (ODA). In line with Murakami, Y. et al. [43-46], this phenomenon is governed by hydrogen embrittlement. In their experiments, hydrogen trapped around the fatigue nucleation inclusion was observed (Figure 16). The fatigue process and trapped hydrogen display a synergistic effect. A schematic drawing of the hydrogen assisting in cyclic stress is presented in Figure 17 [6, 43-46].

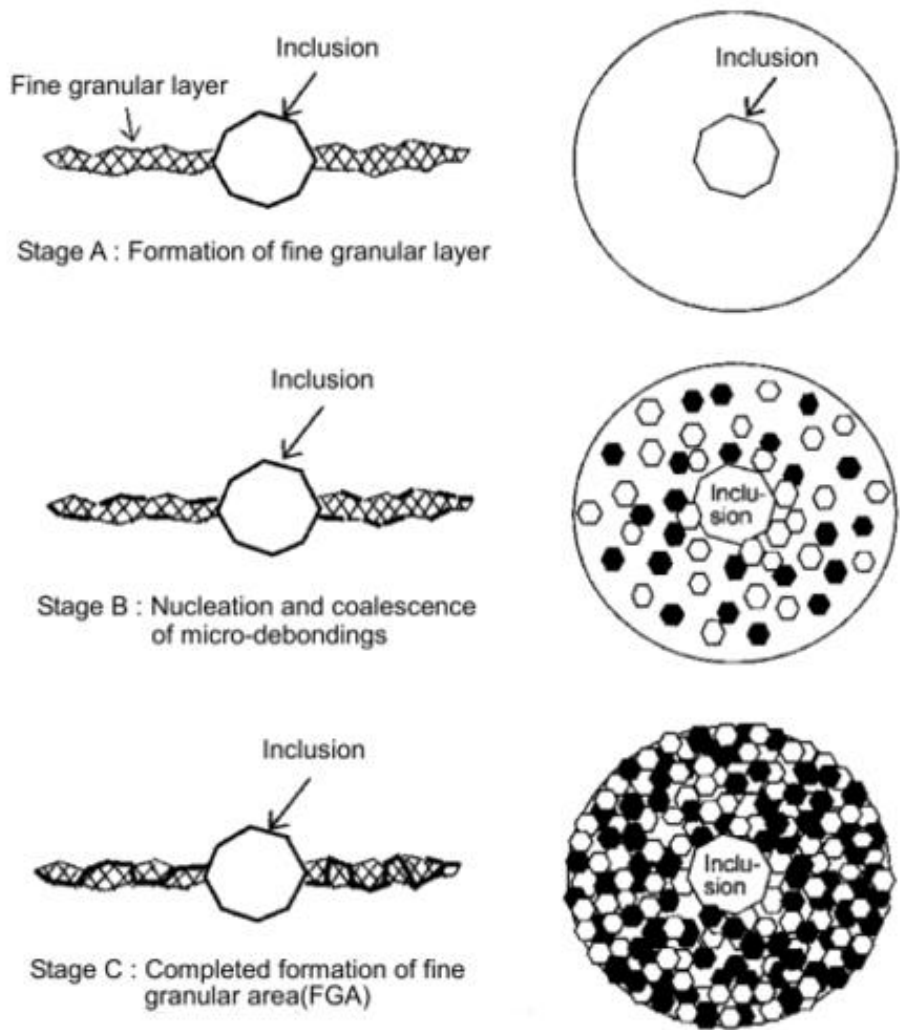


Figure 15: Steps of the FGA formation [37,39].

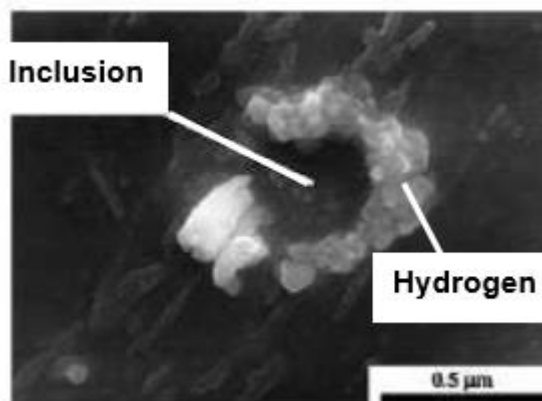


Figure 16: Fractography of the hydrogen trapped around the non-metallic inclusion [adapted by 6].

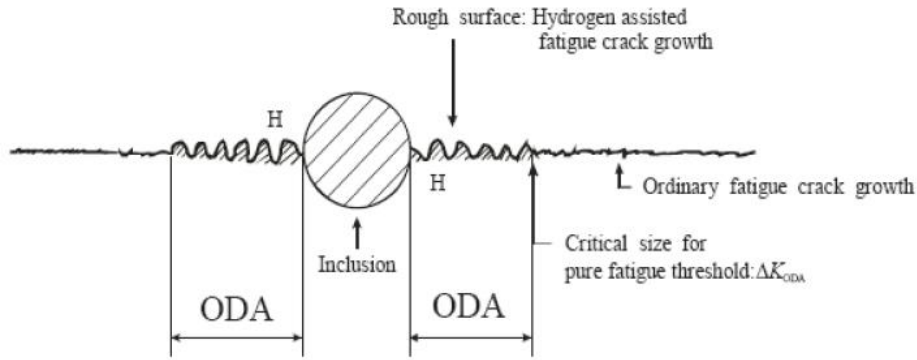


Figure 17: A schematic drawing of ODA formation mechanism [6,43-46].

Another model was proposed by Shiozawa, K. et al. in 2006, called granular bright facet (GBF). This theory suggests that the GBF or FGA formation occurs due to decohesion of spherical carbides with the metal matrix [22]. An illustration of the model can be seen in Figure 18, where (a) corresponds to the cross section of the steel after cyclic loadings and before the crack initiation, (b) represents micro cracks nucleated due to the lost cohesion of the carbides with the steel matrix, as well as the coalescence of the micro cracks, and finally (c) where the fracture surface is formed. Number ① represents the inclusion and fatigue initiation area, ② corresponds to the GBF region and ③ fish-eye region.

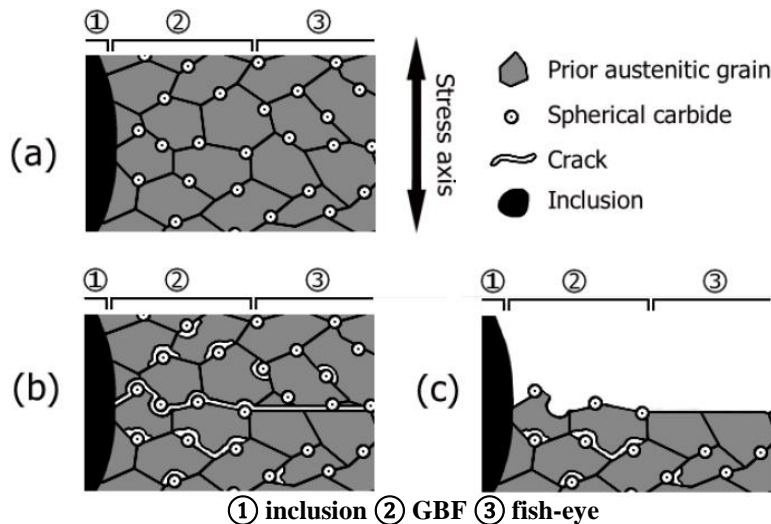


Figure 18: Illustration the cross section of mechanism that conduct the GBF formation [adapted by 39]: a) microstructure before the crack initiation, b) initiation of the micro cracks and coalescence, c) complete GBF facet.

Yet another approach was presented by Hong, Y. et al., named “numerous cyclic pressing” (NCP). The cornerstone of this model relates to the crack closure, that is, nanograins which are formed due to contact with the fracture surfaces after very long cycles. According to their experiments, the FGA formation is only observed in cases of negative loading ratio. It is crucial for compressive stress and the nanograins to be formed layer by layer until complete formation of the FGA [47,48]. The schema of NCP until FGA formation is presented in Figure 19.

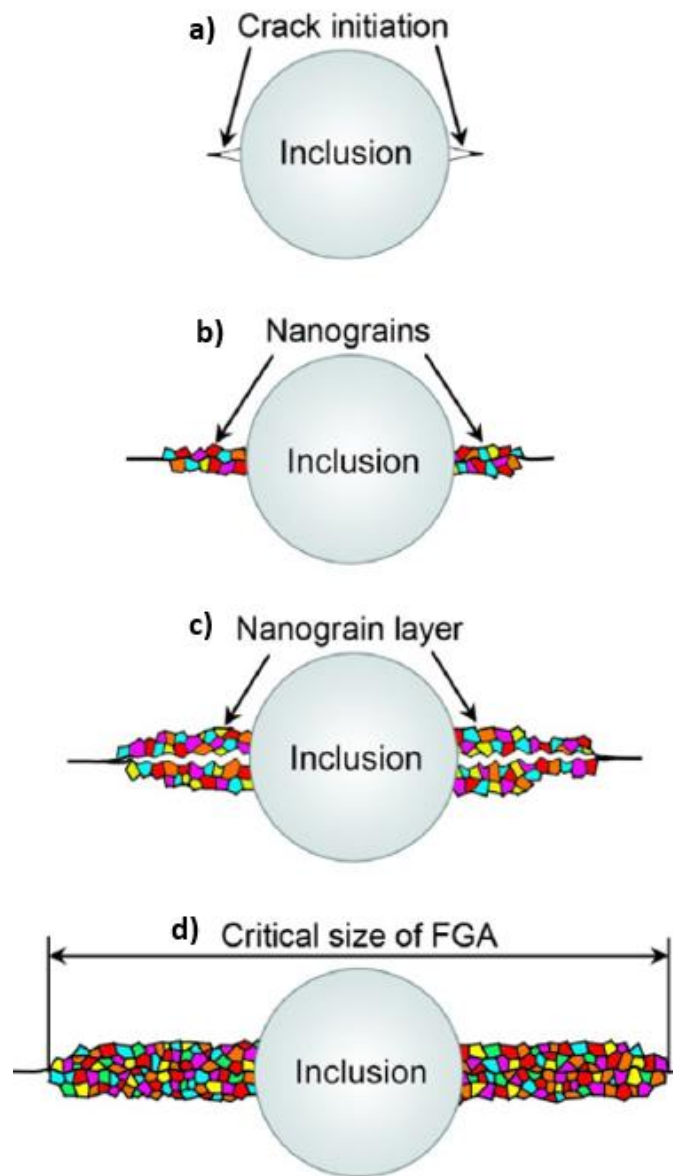


Figure 19: Schematic drawing of NCP model with 4 steps to complete the FGA formation after millions cycles [48]: a) crack initiation, b) nanograins layer, c) appear the rough aspect and d) complete formation of FGA.

NCP was divided in 4 steps, where a) represents the crack initiation between inclusion and the metal matrix. In b) the first layer of nanograins is formed by repeatedly pressing between the crack surfaces and in c) the formation of nanograins can be observed above the previous crack surfaces and the rough morphology after millions of cycles. Finally, the NCP process is finished when the FGA reaches its critical size [47,48].

The last method is similar to the one proposed by Sakai et. al [37]. Grad et al., investigated the FGA region and encountered average grain size around 70 nm for a high strength steel. They conceived a mechanism named “local grain refinement” and described it in six stages [24]. Figure 20 exemplifies the mechanism supported by the experiments conducted by Grad et al.

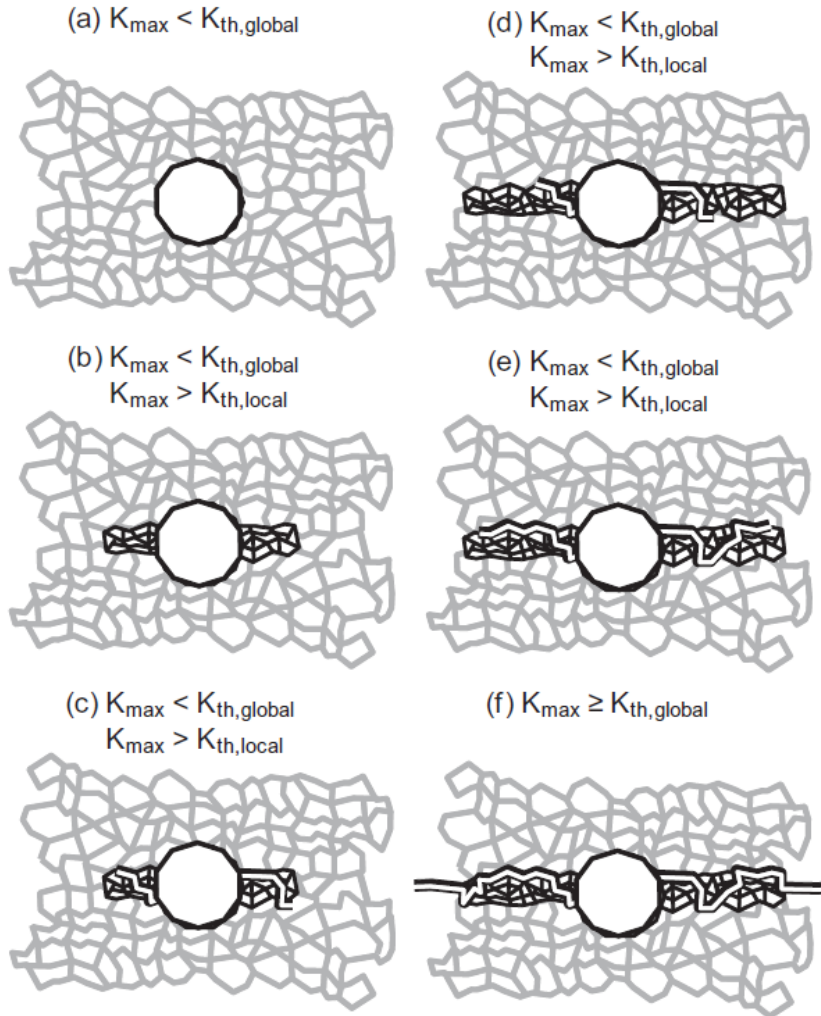


Figure 20: Mechanism of the FGA formation [24]: (a) microstructure before the crack nucleation, (b) local grain refinement, (c) crack nucleation and propagation along the grain refinement, (d) local grain refinement at crack tip, (e) crack propagation and (f) FGA

Firstly, the stages presented in figure 20 relate to the stress intensity factor (SIF). Before the cyclic loading, a microstructure with an inclusion that possess maximum SIF (K_{max}) is less than the global SIF threshold ($K_{th,global}$) value (a). With the cyclic loading, a local grain refinement is formed and the main hypothesis proposed by Grad et al. is that this is formed precisely due to increased stress promoted by the inclusion in its vicinity (b). In this case K_{max} remains less than $K_{th,global}$ but greater than the local SIF threshold ($K_{th,local}$). In the next stage (c) the crack initiates and starts to grow along the grain refinement (FGA). The fine grain continues to form due to the

stress concentration at the crack tip and the $K_{th,local}$ value decreases (d) and is able to propagate (e). These stages repeat until the K_{max} of the inclusion $\geq K_{th,global}$ (f) [49].

3.3.2.1 Empirical Equations

Numerous models with the goal of estimating the FGA size were developed from empirical equations. A common approach of these models is to connect the FGA size to the mechanical characteristics. The root parameter of area described by Murakami in his works and expressed by \sqrt{area} was initially developed to obtain the projected defect area the same direction of maximum stress applied in uniaxial loadings. Murakami and Endo [50,51] suggested that the fatigue limit can be estimated considering a small artificial defect on the specimen surface. Thereafter, Murakami used the same equation to estimate the FGA size from the applied stress and proposed three constants to differentiate the fatigue crack initiation sites. For all models (Equations 12-14) presented it is assumed that the FGA is a circular region.

Murakami and co-authors [50-52] proposed that FGA size is dependent on the applied σ_a and Vickers hardness (HV) as:

$$\sqrt{area_{FGA}} = \left[\frac{C (HV + 120)}{\sigma_a} \right]^6 \quad (12)$$

where C is a constant whose values vary with crack initiation site, being equal to 1.41 for superficial cracks, 1.43 for subsurface cracks and 1.56 for internal cracks initiation.

The following expression is an adaptation of equation (12) proposed by Liu and co-authors [52,53]. The constant C has a single value regardless of crack initiation site.

$$\sqrt{area_{FGA}} = \left[\frac{2(HV + 120)}{\sigma_a} \right]^6 \quad (13)$$

In the two equations given above, the FGA size is expressed in μm .

An expression obtained by Yang and co-authors [52, 54] indicates that the FGA size is influenced by σ_a as well as σ_y . The FGA size in meters is given by

$$\sqrt{area_{FGA}} = 1240 \frac{1}{\sigma_y^{0,533}} \frac{1}{\sigma_a^2} \quad (14)$$

Taking into account the FGA and fish-eye sizes, it is possible to calculate the stress intensity factor, ΔK , at their boundaries

$$\Delta K_{int} = \frac{2}{\pi} \Delta \sigma \sqrt{\pi a} \quad (15)$$

where $\Delta \sigma$ is the applied stress range, a is an interior crack radius and can be replaced by the FGA or fish-eye radius (r_{FGA} , $r_{fish-eye}$).

In fully reversed cyclic loading, the equation (16) can be rewritten to maximum SIF, K_{max} [55].

$$\Delta K_{int} = 2K_{max} = \frac{4}{\pi} \sigma_a \sqrt{\pi a} \quad (16)$$

3.3.3 Temperature and Frequency Effects

As aforementioned, VHCF tests use high frequency loading which reduce the test time. The main advantage of ultrasonic fatigue test is to investigate the properties of very long life materials in a reasonable time. Notwithstanding, the elevated frequency of stress levels during the test can cause heating of the test specimens. Some authors [9,26,56-59] reported the temperature effect. Peng et al. [59], averred that the

materials which possess ultimate strength lower than 1000 MPa are sensitive to burning.

It is known that temperature is one of the factors which can influence the materials fatigue performance. To avoid the temperature increase during the VHCF the cooling system is indispensable, and most tests use an intermittent driving resource (pulse and pause technique) [9]. Depending on the material under study, it is essential to increase the pause times to obtain better temperature control, and/or employ an additional mechanism to increase cooling and keep the test at room temperature.

Figure 21, shows the fracture surface of the steel AISI 4140 that burned.

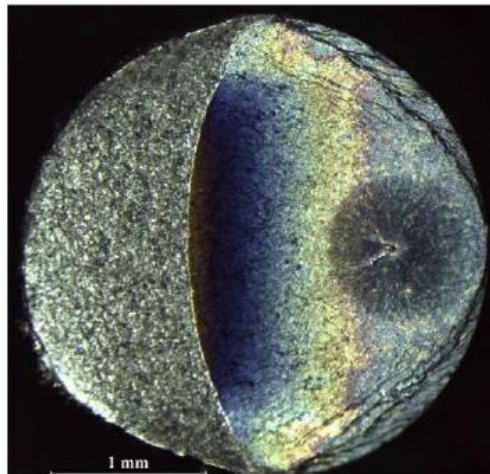


Figure 21: Fracture surface of tested specimen in ultra high frequency [56].

Moreover, the effect of loading frequency on deformation behavior of the metallic material is often discussed. Several authors [5,9,60-64] published on the influence of the stressing frequency in fatigue results and observed a strong material dependency of the frequency loading. Figure 22 exhibits the fatigue strength of low carbon steel under different loading frequencies [9, 66,67].

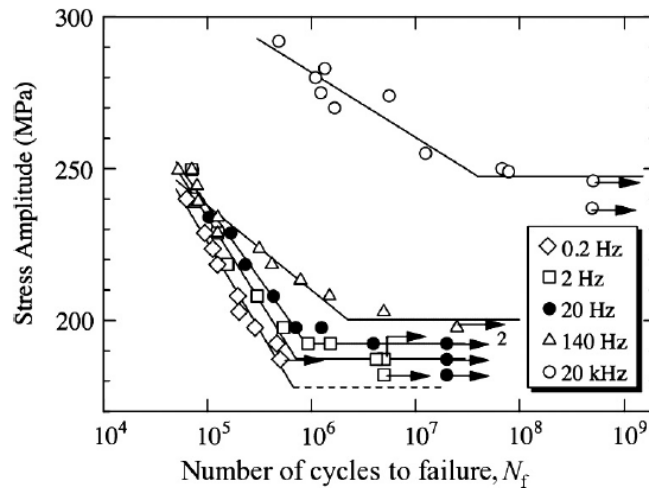


Figure 22: S-N curve of low carbon steel under different loading frequencies [67].

The frequency effect can be insignificant for some non-ferrous alloys, although for steels its influence cannot be ignored. A recent report [69] remarked that steels with a body-centered cubic (BCC) structure displayed a more pronounced effect of loading frequency. The dislocation in a BCC structure tends to be less active compared to FCC (face-centered cubic) structures. For FCC structures, the frequency effect is expected but insignificant, according to the literature [57-70].

Furthermore, it is known that the motion of dislocation is thermally activated [68,71]. Therefore, the motion of dislocations in BCC is associated with a high activation energy and lattice friction. Under ultrasonic fatigue tests, according to Shao et al. [68], the time for relaxation of dislocation is limited and a great part of the total strain is accommodated by elastic and anelastic deformation [72,73]. Consequently, BCC materials have limited mobility dislocation and exhibit a higher fatigue strength in VHCF tests when juxtaposed with low frequency tests. In addition, the rate dependence of cross-slip requires more time (higher number of cycles) to occur under 20 kHz. Under low frequency, the dislocations have more time to propagate [68].

4 Temperature Application to Predicted the Fatigue Life

Thermodynamic applications associated with the mechanical fatigue have been reported in the literature [74-87] in order to predicted the fatigue life. Some methods were tested based on Temperature parameters obtained from T-N curve. Meneghetti [75,79-81], related the fatigue life with heat dissipation. In fact, all of these methods, were used for LCF and HCF regime.

The temperature evolution during fatigue test is represented as T-N curve, illustrated in Figure 4. This curve is divided in 3 phases and each phase indicate different stages along the fatigue test [74-87]:

- Phase I: After starting the test, the temperature of the specimen increase rapidly from room temperature (T_0) until the stabilized temperature or steady state temperature (T_s).
- Phase II: There is a low temperature difference and it is considered the specimen is in the steady state temperature (T_s). According to the literature, this phase comprises the most of fatigue life.
- Phase III: The temperature increase rapidly again but with a small number of cycles. The third phase correspond the end of the fatigue test when the specimen fracture.

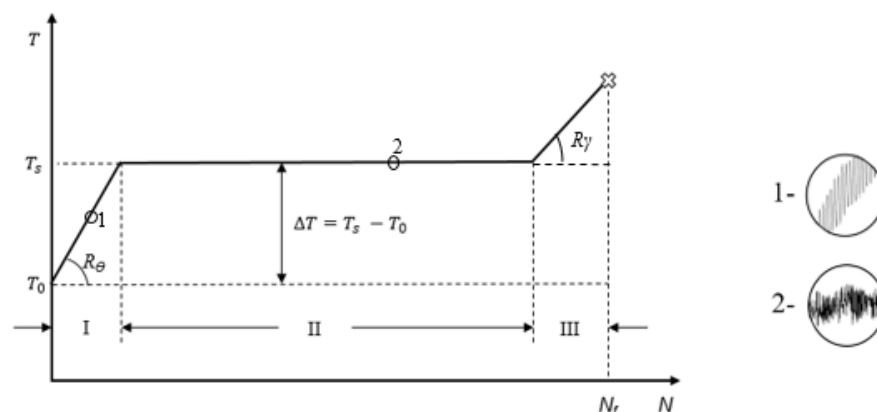


Figure 23: Theoretical T-N curve [adapted by 74].

The phase II tends to decrease and R_θ is more pronounced with the higher applied stress amplitude (σ_a) with constant operational frequency (Figure 24). This behavior is often described in low frequency tests.

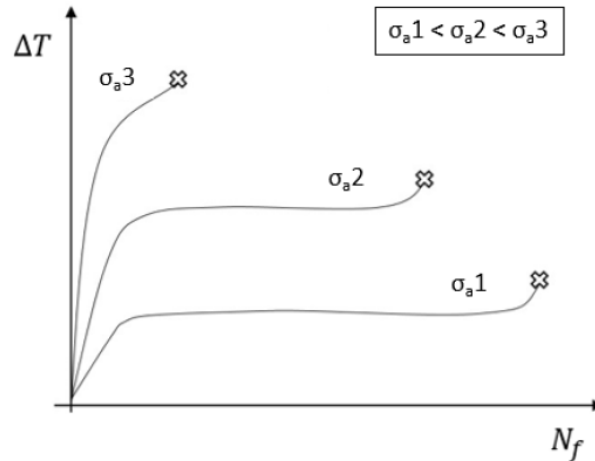


Figure 24: Illustration the temperature evolution with the applied σ_a (adapted by [75])

As known, the fatigue is an irreversible process and the energy dissipation during the cyclic loading is responsible to the temperature increase at the beginning of the test. When the temperature achieves the T_s , the thermal energy was totally dissipated [75,82,83].

Based on that, Meneghetti [75,79-81] performed several fatigue tests at low frequencies. Plain and notched specimens were subjected under low and high cycle fatigue regime. Meneghetti reported the Q_{cyc} is a material property independent the specimens' design, operational frequency and can be characterized as a fatigue damage parameter. A Q_{cyc} (Equation 17) is related to 1st law of thermodynamics and its analytical procedure can be seen in [23,24]. Originally, Q_{cyc} is proportional to the slope temperature at the beginning of cooling stage [75,79-81]. However, Jang and Khonsari [85] mentioned that the slope temperature when start the test ($t = 0$) is the same slope temperature at the cooling stage.

$$Q_{cyc} = \frac{\rho c_p R_\theta}{f} \quad (17)$$

where, ρ is density (kg/m^3), c_p specific heat capacity ($\text{J/kg } ^\circ\text{C}$), and f frequency (cycles/s).

Jiang et al. [86] related the fatigue life with T_s from the T_0 . The correlation is presented in Equation 18. This model can be applied if the performed test presented the steady state temperature and the final fracture.

$$(N_f)^m = C \Delta T \quad (18)$$

where m and C are material constants.

Fargionne et al. [87] presented the area underneath the T-N curve is constant and can estimate the fatigue curve. This also requires the steady state temperature. The equation presented the following correlation.

$$\emptyset = \int_0^{N_f} \Delta T dN = \text{constant} \quad (19)$$

The most recent model was provided by Amiri and Khonsari [84] and depends only the temperature increase at the beginning of the test, R_θ .

$$N_f = c_1 R_\theta^{c_2} \quad (20)$$

where c_1 and c_2 are constants.

5 Microplasticity

According to the Coffin-Manson law, macroplasticity strain amplitude and number of cycles to failure are interconnected. This law is usually applicable for LCF regime. However, the Coffin-Manson-Basquin it was attributed for HCF, where the deformations are macroscopically elastic and an elastic portion was added to obtain the total deformation in HCF regime. The Equation (21) exhibits the formulation of Coffin-Manson-Basquin [1].

$$\varepsilon_{a,T} = \varepsilon_{a,e} + \varepsilon_{a,p} = \frac{\sigma_f'}{E} [2N_f]^b + \varepsilon_f' [2N_f]^c \quad (21)$$

where, the elastic portion ($\varepsilon_{a,e}$) is given by σ_f' and b which are the fatigue strength coefficient and exponent. The plastic parcel ($\varepsilon_{a,p}$) depends the ε_f' which is the fatigue ductility coefficient and c that is the fatigue ductility exponent. The regression for the function (equation 21) has been determined by the method of least squares.

Mugrhabi [30-32], attributed the Coffin-Manson-Basquin law to estimate the microplasticity strain in VHCF regime.

Another theory introduced the law of localization and homogenization [88,89] to calculate the microplasticity strain. This law related the macroscopic stress tensor (considering the stress amplitude) to microscopic stress tensor (σ_a^μ) and plastic strain tensor ($\varepsilon_{a,p}^\mu$).

$$\varepsilon_{a,p}^\mu = \frac{\sigma_a}{4\mu(1-\beta)} - \sqrt{\left(\frac{\sigma_a}{4\mu(1-\beta)}\right)^2 - \frac{d1}{2\mu f \xi \pi(1-\beta)}} \quad (22)$$

Where μ is the shear modulus, f is frequency, ξ is the constant parameter commonly assumed as 0.9, $d1$ energy dissipation and β is dependent of the Poisson's ratio ν .

$$\beta = \frac{2(4 - 5\nu)}{15(1 - \nu)} \quad (23)$$

$$\sigma_a^\mu = \sigma_a - 2\mu(1 - \beta)\varepsilon_{a,p}^\mu \quad (24)$$

6 Materials and Experimental Procedure

The experiments and research work took place in LABFADAC and metallography laboratory of Materials and Chemical engineer department (DEQM) of PUC-Rio. The thermographic analyzes were supported by Senai Institute of Inspection and Integrity. The fractographic analysis (SEM, EDS and FIB) were supported by Mechanical department and Physics department, both in PUC-Rio university.

The steels under this study, were obtained from crankshaft that failed in service, related to the project “Saúde Estrutural de Eixos Virabrequins”.

6.1 Materials

The materials used for this study was a high strength steel, DIN 34CrNiMo6 and DIN 42CrMo4 which have a large applicable in a manufacturing of many mechanical components.

The chemical composition, restricted to main elements, of both steels are presented in Table 2. The entire chemical composition are available in Appendix B.

Table 2: Chemical composition with the main elements.

DIN 34CrNiMo6	C (%)	Mn (%)	Cr (%)	Mo (%)	Ni (%)	Fe (%)
	0.35	0.49	1.44	0.29	1.57	94.8
DIN 42CrMo4	C (%)	Mn (%)	Cr (%)	Mo (%)	Ni (%)	Fe (%)
	0.32	0.69	0.97	0.28	0.80	96.0

Mechanical properties of steels under study are available on Table 3. In both of steels, the density (ρ) is 7,870 kg/m³. The specific heat capacity (c_p) and Vickers

hardness are 475 J/kg °C and 302 HV for DIN 34CrNiMo6, 473 J/kg °C and 284 HV for DIN 42CrMo4.

Table 3: Mechanical properties of the steels under study.

	σ_u (MPa)	σ_y (MPa)	E (GPa)
DIN 34CrNiMo6	900	760	207
DIN 42CrMo4	907	715	209

6.2 Experimental Procedure

Specimens were machined from the crankshafts failed prematurely in a thermoelectric power plant.

To performed the VHCF test, hourglass geometry was chosen. The resonance length (L_j) was calculated directly to the *Supersonic* software that accompanies the ultrasonic fatigue machine. Figure 25 present the hourglass shape and its dimensions.

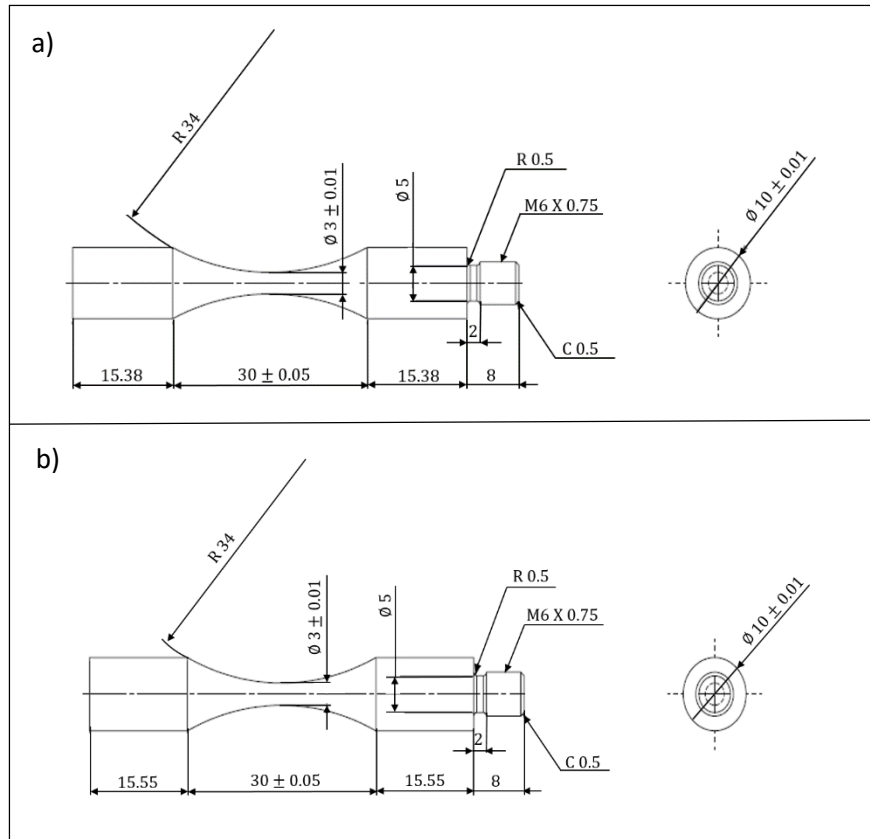


Figure 25: Hourglass specimens and its dimensions for testing in fully reversed conditions.

The resonance length is 15.38 mm and 15.55 mm for DIN 34CrNiMo6 and DIN 42CrMo4, respectively.

In order to evaluate with different loading conditions, that is, test with mean stress, it is necessary to machine specimens with thread in both side.

6.2.1 Calibration

Formerly to carry out the ultrasonic fatigue tests, the calibration step is necessary and must be done for each geometry and material. The calibration instrument and signal captured by the sensor can be seen in Figure 26.

The instrument should be positioned at the free end of the test specimen and the objective is to comprehend the response to a given displacement. Initially, it is measured 3 displacements for ± 500 millivolts (mV) (Figure 26b) and obtained the mean value. A factor ($\mu\text{m} / \text{mV}$) is estimated.

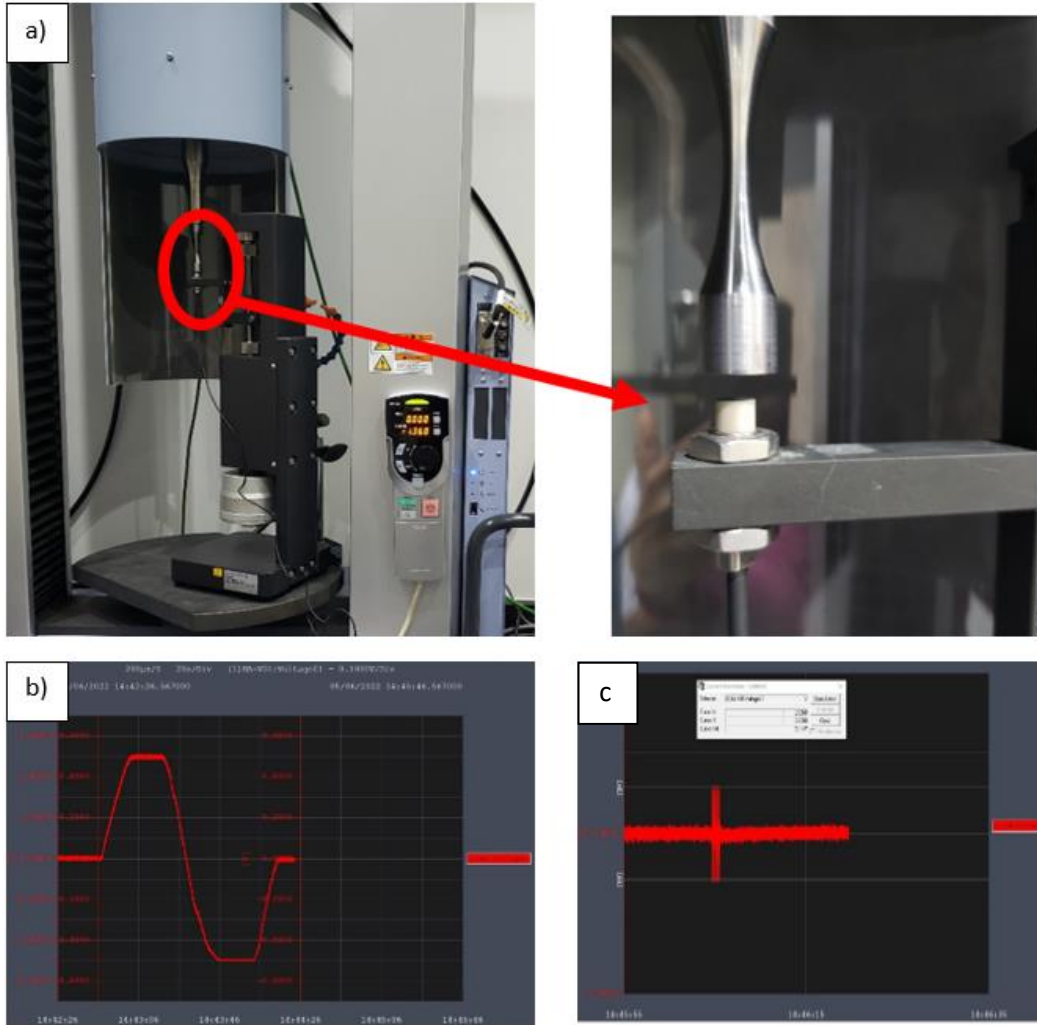


Figure 26: a) Calibration instrument, b) the signal captured the amplitude and c) oscillation (peak to peak value).

In sequence, it is measured the peak to peak from the oscillation applied for each percentage of the maximum power output of the system (20%, 40%, 60%, 80% and 100%), as presented in Figure 26c. The displacement for each percentage is calculated using the peak to peak value (mV) multiplied by the factor ($\mu\text{m} / \text{mV}$) obtained previously. A displacement for the horn side (μm) is obtained, related with each percentage and finally attained the correction factor. This correction factor ensures that the stress-strain relationship is linear.

Posteriorly, the VHCF test can be initiate inserting the stress amplitude that will be converted to the amplitude value of the actuator.

6.2.2 VHCF with Thermographic Test

Article publisher as “M.C. Teixeira, A.L.T. Brandão, A.P. Parente, M.V. Pereira, *Artificial intelligence modeling of ultrasonic fatigue test to predict the temperature increase*, International Journal of Fatigue, Volume 163, 2022, 106999, ISSN 0142-1123, <https://doi.org/10.1016/j.ijfatigue.2022.106999>. (**Appendix A**). Reproduced with permission from M.C. Teixeira and co-authors. Copyright 2022 Elsevier B. V.

Experiments were carried out on ultrasonic fatigue testing machine model Shimadzu USF-2000A (Figures 27). In the first thermographic analysis, specimens were subjected to fully reversed fatigue loadings ($R=-1$) with different *pulse* (loading times) – *pause* (pause times) and stress levels. Four stress levels were selected based on the mechanical strength limit of the material (σ_u), being 30, 35, 40 and 45%, that is equivalent a stress amplitude (σ_a) = 270, 315, 360 and 405 MPa and five times to *pulse* - *pause*, measured in milliseconds (300-200, 200-200, 200-300, 110-300 and 110-500) [26].

A thermographic camera (Figure 27) model A655SC on passive mode, which was coupled with an infrared lens IR with focal distance of $f = 41.3 \text{ mm}$ (15°FOV), was used to comprehend the temperature evolution during the tests and thus obtain the raw data for modeling. All tests were performed up to 10^7 number of cycles [26].

A black coating spray jet paint was applied to the specimens raising the emissivity to 0.93. This step is necessary to obtain better precision while monitoring the temperature. The spray jet is resistant to high temperatures ($600 \text{ }^\circ\text{C}$) and its emissivity was verified and compared with the obtained thermography data to measurements using a manual thermocouple contact system [26].

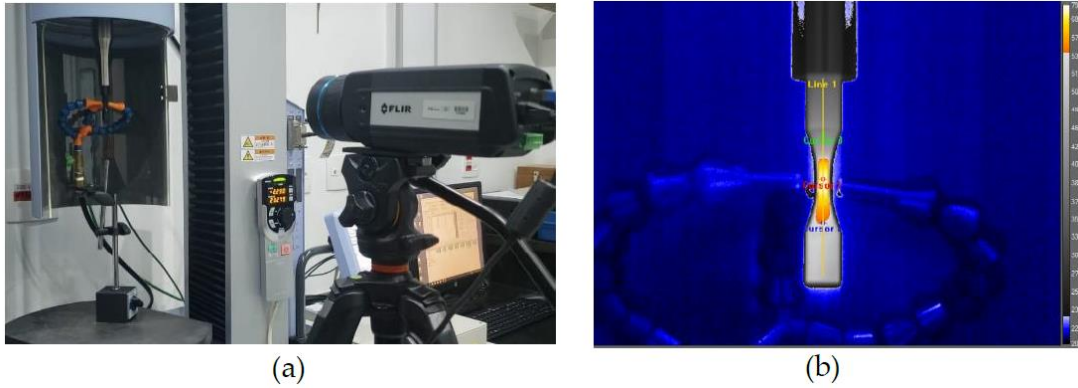


Figure 27: a) Illustration of the ultrasonic fatigue machine USF2000A and IR camera model FLIR A655SC [6]. b) Thermogram of the specimen surface.

In addition, tests were performed with and without cooling with target of number of cycles 10^6 . For these specific tests, were used the lower frequency effective (f_{eff}) in order to preserve the machine and the specimens. These tests were conducted to identify the efficiency of compressed air on temperature throughout the VHCF test.

With these test results, a second analysis was conduct with the same test conditions to obtain the S-N curve in room temperature (RT).

Table 4 presents the parameters relative to ambient conditions at the moment that the fatigue tests were carried out and passive thermography configurations.

Table 4: Parameters of the fatigue experiments[26].

d of camera to specimen	0.5 m
Room temperature	$\sim 20\text{ }^{\circ}\text{C}$
Emissivity	0.93
Frames per second	100
T range settings	$-40\text{ to }150\text{ }^{\circ}\text{C}; 100\text{ to }650\text{ }^{\circ}\text{C}; 300\text{ to }2000\text{ }^{\circ}\text{C}$

6.2.3 Ultrasonic Fatigue tests

Tests with high frequency were performed using the pulse-pause technique. After the thermographic tests the pulse-pause that gathered the specimens will not suffer temperature effect was 300 msec – 500 msec. This intermittent loading provides a f_{eff} around to 7,521 Hz.

Figure 28 demonstrates the software “Supersonic” and “Trapezium” used to control the test and data acquisition. Trapezium, it is only used to apply the pre-load.

Specimens were tested in fully reversed loading condition ($R = -1$) with different stress levels. Subsequently, the tests were carried out of $R = -0.5, -0.25$ and 0 for DIN34CrNiMo6 steel and with $R = -0.5, -0.25$ for DIN 42CrMo4. Figure 29 presented the USF2000A machine of Shimadzu company without and with the apparatus which allow to perform with mean stress. These tests were conducted with stress amplitude between 35% and 60 % of the ultimate strength of the material up to 10^9 cycles target.

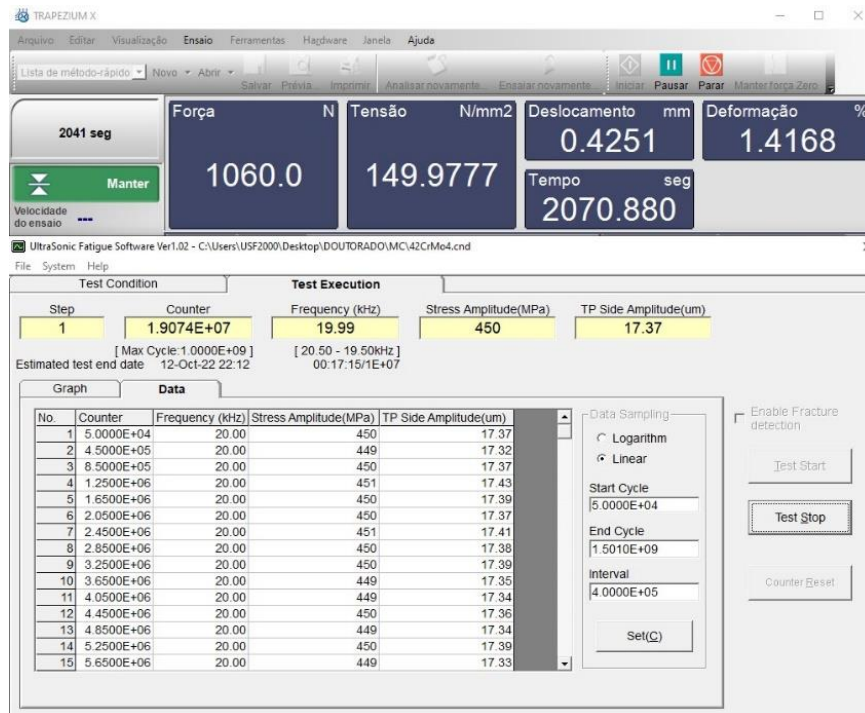


Figure 28: Software used to control the test.

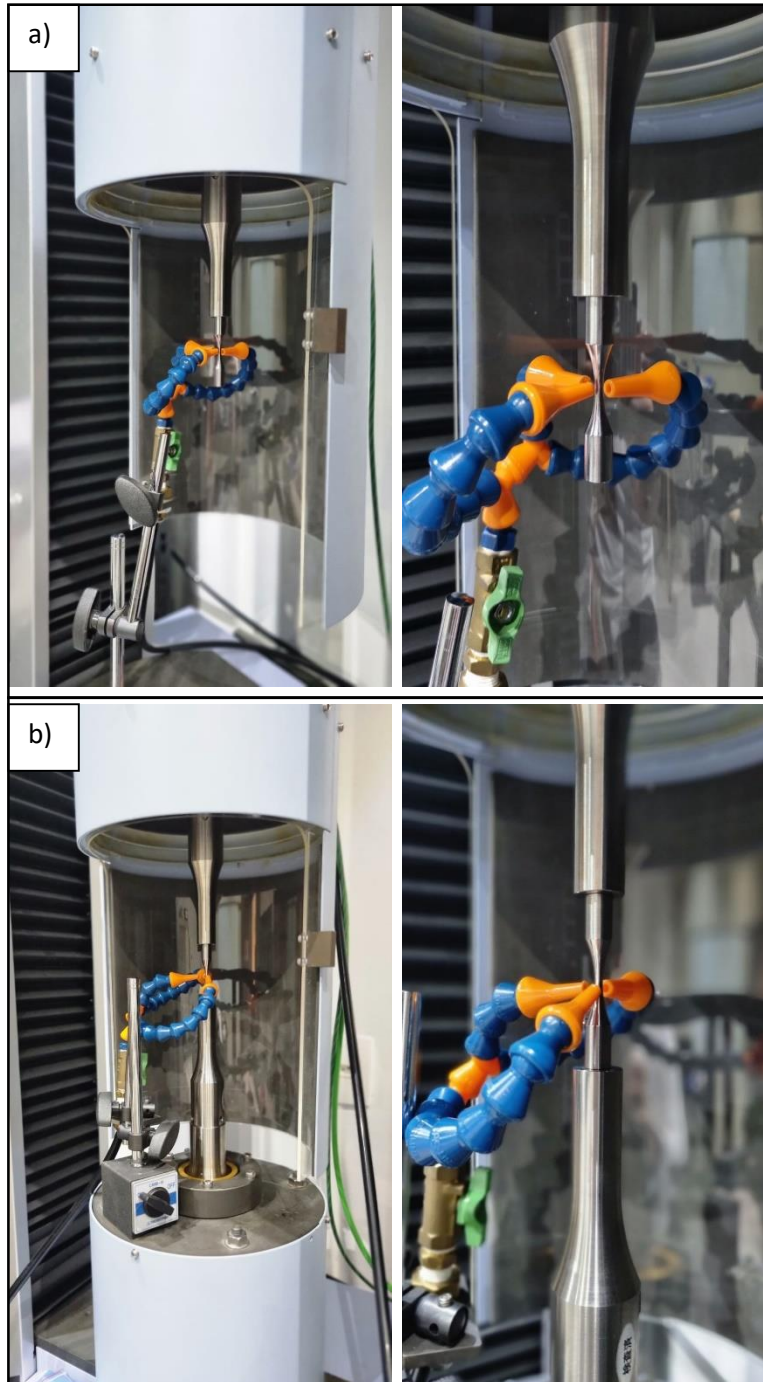


Figure 29: USF 2000A from LABFADAC used to performed the tests: a) $R=-1$ and b) $R \neq -1$.

6.2.4 Metallography

To determine the area fraction of inclusions, present in the material and their types, two samples of each steel were selected.

Samples were taken from the straight cylindrical part of specimens that failed due to fatigue. The samples were prepared on the polisher with different grain sizes and later on cloths with 6 μm , 3 μm and 1 μm .

A total of 20 images of each sample of each material were collected and used in a digital image program (Image J). An analyze particles was performed to obtain the quantity of particles for each image. After optical microscopy analysis, the samples were etched with “Nital” 2% to reveal the microstructure.

6.2.5 Scanner Electron Microscopy (SEM) and Focused Ion Beam (FIB)

Images of fracture surfaces were performed with SEM to identify the crack initiation. One specimen of each material with internal or subsuperficial crack initiation were lead to FIB in other to perform a cross-section of the FGA region and identify how much of the subsurface was modified for the formation of fine grains. Subsequently, the region obtained by FIB was observed in SEM-EBSD.

The equipment used to obtain the images of SEM-EBSD and FIB can be seen in Figure 30.



Figure 30: a) SEM/EBSD from mechanical department and b) FIB from physics department, both from PUC-Rio.

7 Results and Discussion

7.1 Microstructure and Inclusions

The microstructure encountered for both steel is predominantly bainitic and martensitic. This results are expected for the chemical composition presented in Table 2 and were underwent the process of quenching and tempering. Figure 31 present the micrograph of the steels.

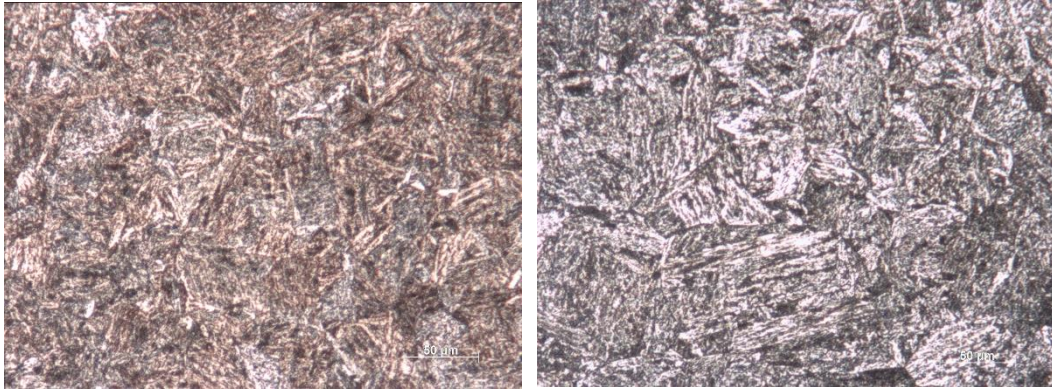


Figure 31:Micrograph of: a) DIN 34CrNiMo6 and b) DIN 42CrMo4.

The most of inclusions observed in the optical microscopy are sulfides and alumina, according to the standard E-45 18a. The inclusions of each steel can be observed in Figure 32.

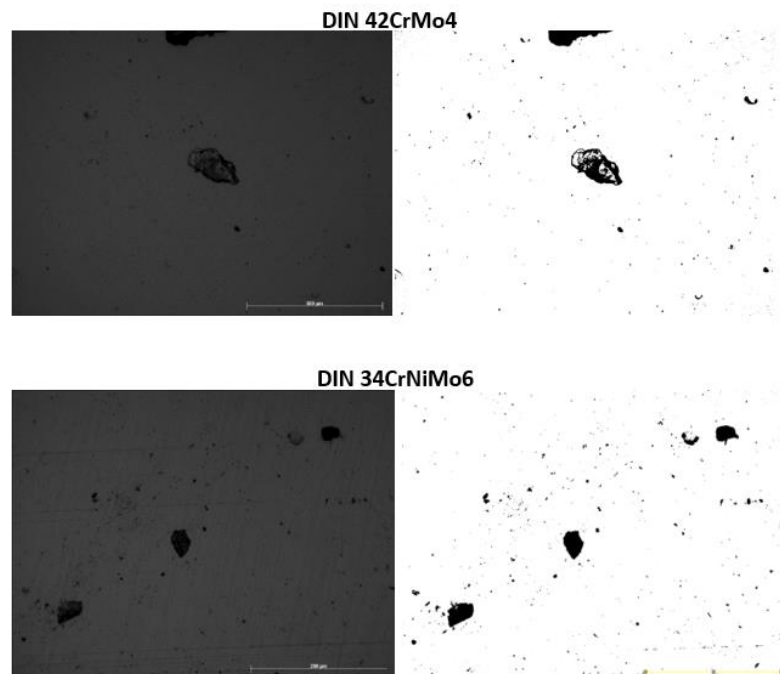


Figure 32: Fractographics obtained by optical microscopic and digital image program ImageJ.

7.2 Experiments and Computational T-N curve

Article publisher as “M.C. Teixeira, A.L.T. Brandão, A.P. Parente, M.V. Pereira, *Artificial intelligence modeling of ultrasonic fatigue test to predict the temperature increase*, International Journal of Fatigue, Volume 163, 2022, 106999, ISSN 0142-1123, <https://doi.org/10.1016/j.ijfatigue.2022.106999>. (**Appendix A**). Reproduced with permission from M.C. Teixeira and co-authors. Copyright 2022 Elsevier B. V.

7.2.1 Experimental Results

The graphs and images obtained through the thermography method can be seen in Figure 33-35. These images show the thermal gradients measured in the center of the specimen where the maximum stress occurs.

Figures 33 and 34 show the T-N curves of the tested specimens. For tpulse-tpause of 300-200 msec were those that presented the highest temperatures for all stress levels, as expected. For the stresses amplitude of 270 and 315 MPa can be observed the steady-state temperature independent of intermittent loading condition. All tests with intermittent loading of 110-300 msec, steady-state temperature were observed. Specimens tested with stress levels of 360 MPa and 405 MPa with tpulse-tpause for 300-200, 200-200 and 200-300 reached temperatures above 300 °C and failed. There was a clearly reduction in fatigue life due to temperature increase when comparing the test conditions of each specimen.

Figure 35 shows the T-N curves of 4 specimens in tpulse-tpause equal 110-500 msec with and without compressed air cooling. The specimens without cooling did not present the steady-state temperature until 10^6 cycles. On the other hand, the cooled specimens, obtained the steady-state temperature before 100,000 cycles. The cooled specimens decreased the maximum temperature in approximately 45 °C with the stress amplitude of 360 MPa. Already at the stress level of 30% σ_u reduced the temperature in 15 °C with the air cooling.

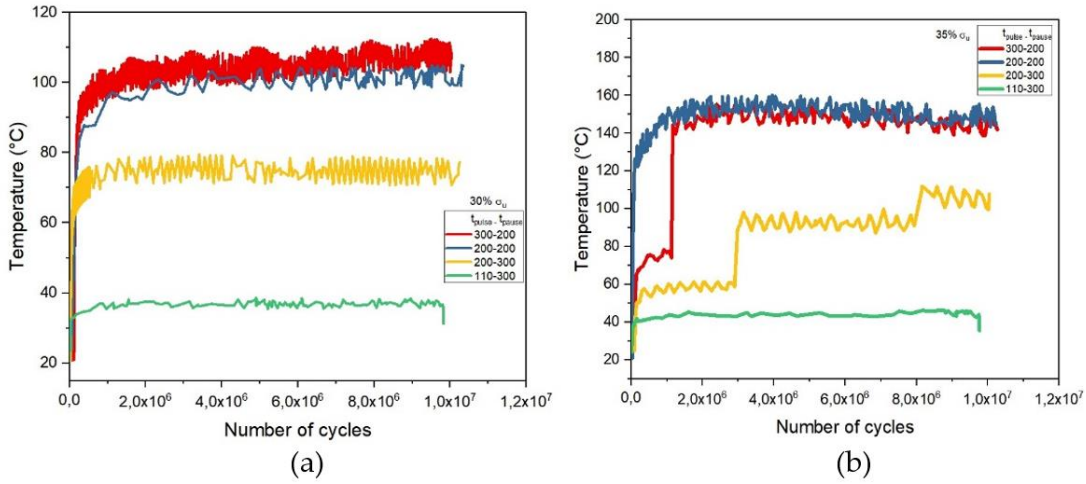


Figure 33: Thermal gradients of: a) 30% $\sigma_u = 270$ MPa and b) 35% $\sigma_u = 315$ MPa.

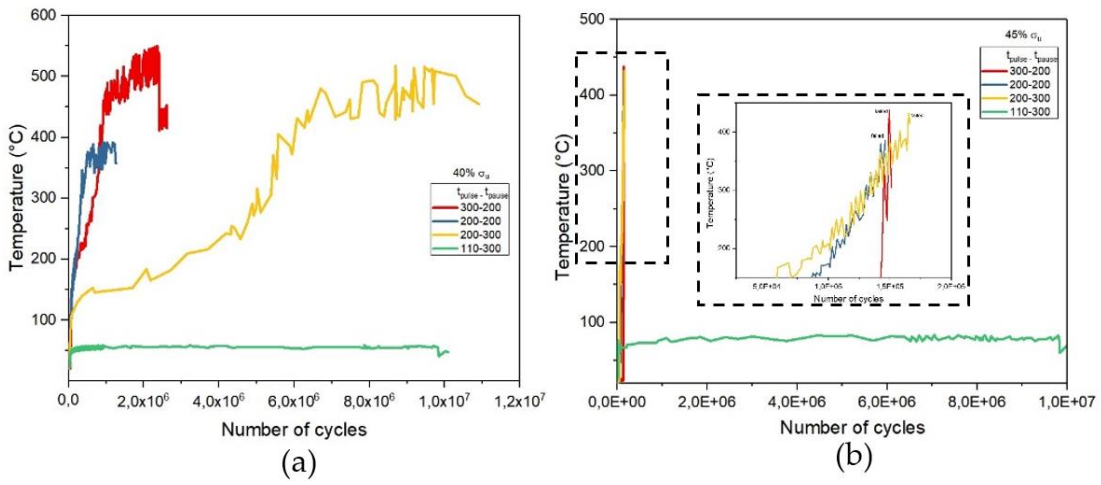


Figure 34: Thermal gradients of: a) 40% $\sigma_u = 360$ MPa and b) 45% $\sigma_u = 405$ MPa.

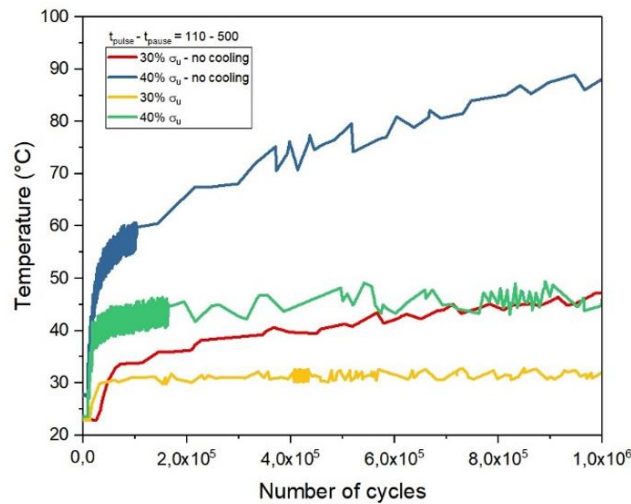


Figure 35: Thermal gradients of 30 and 40% σ_u in 110-500 msec with and without cooling.

7.2.2 Artificial Intelligence modeling to predict the temperature increase.

Figures 36a and 36b show the regression curve and the T-N curve for predicted versus observed values for the training dataset. They both compare experimental VHCF temperature values with those estimated by the XGBoost model. The high degree of agreement between the experimental data and the model's outputs suggests that the model learned the data's pattern even at non-linear regions. Based on the results of section 7.2.1, it can be said the model was able to learn the cases that failed before 10^7 cycles and the specimens that were not cooled throughout the test.

Figures 37a and 37b present similar profile concerning the test dataset, proving that not only is the model able to learn the data patterns but is also capable of generalization when presented to new data.

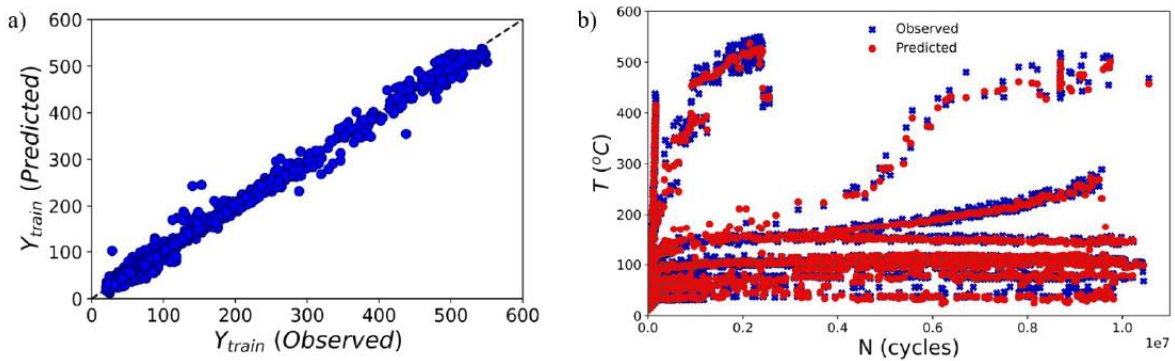


Figure 36: Scatter plots of train model: a) comparison predicted and observed T and b) T-N curve.

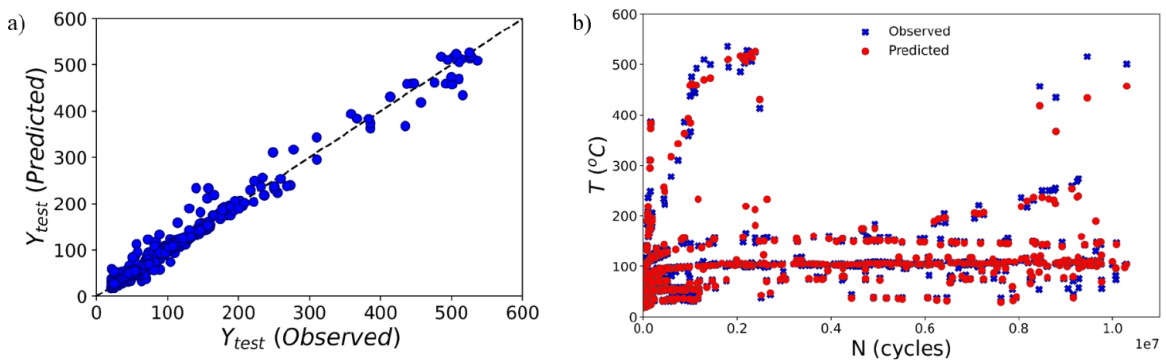


Figure 37: Scatter plots of test model: a) comparison predicted and observed T and b) T-N curve.

The learning curve depicted in Figure 38 presents the values of the performance metric R^2 for both training and validation sets as the number of training patterns increases. It enables us to detect and diagnose the occurrence of underfitting and overfitting. Underfitting happens when the model is not able to learn the patterns in the data properly. It is evidenced by low scores on both the training and validation sets and by a flat curve despite training. Overfitting happens when the model is over trained on the data, learning its noise. An overfit model learns each example so perfectly that it memorizes them. In overfit models the training and validation learning curves are usually far away from each other. Results indicate that the model did not overfit neither underfit; that is, it learned the latent data patterns and relationships and was able to make predictions on new data.

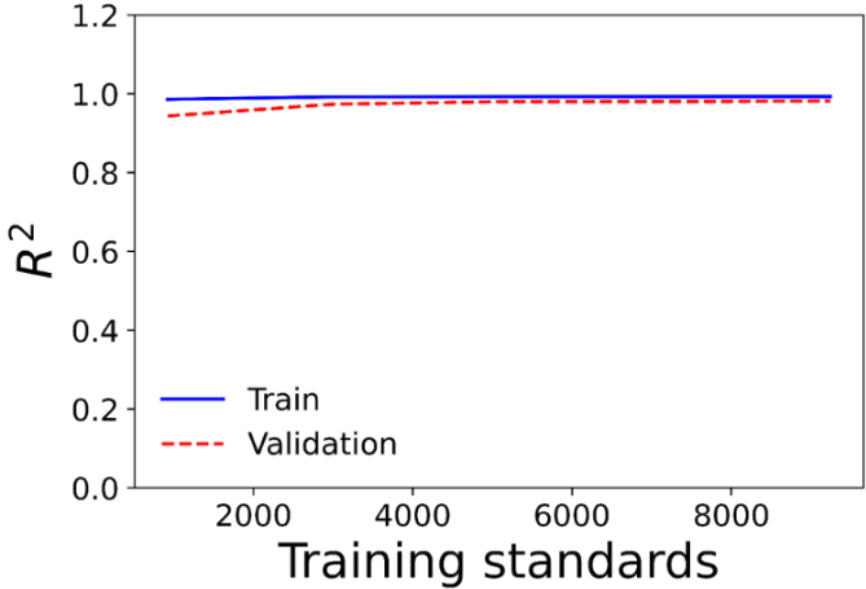


Figure 38: Model performance from the R^2 .

Additional performance metrics are presented in Table 5 to assess the model’s performance from multiple angles.

Table 5: Model comparison performance over MAE, R^2 , R^2_{adj} , MSE and RMSE.

	MAE	R^2	R^2_{adj}	MSE	RMSE
Train	3.1805	0.9932	0.9932	32.0372	5.6601
Validation	4.2344	0.9835	0.9835	72.2337	8.4990
Test	4.3158	0.9830	0.9829	74.0939	8.6077

In general, the performance metrics indicate a high-performance model. The R^2 values exceed 0.98 for all datasets, which evidences the high proportion of the variance in the dependent variable (Y) that is explained by the independent variables (Xs). As the coefficient of determination values do not differ from the adjusted coefficient of determination (R^2_{adj}), the number of input variables does not mask the results. While the mean of absolute error (MAE) is less sensitive to outliers, the mean of squared error (MSE) penalizes large errors. Even though there is no standardized value for MAE and MSE, the scores are small and comparable for all subsets of the dataset. The root mean of squared error (RMSE) values are reported in the unit of the target, and they are about 500x smaller than the experimental data variance, confirming the reliability of the model.

Machine learning models try to map relationships and patterns between the independent (X) variables and the target (Y). Model interpretation tries to understand the choices taken by models in their decision-making process. Shapley additive explanations (SHAP) is a game-theoretic approach to explain the output of any machine learning model. SHAP explains the prediction of an instance by computing the contribution of each feature to that prediction using the Shapley values, which is the average marginal contribution of a feature value across all possible coalitions [90,91].

Figure 39a depicts the features importance based on their absolute Shapley values. To compute the global importance, the absolute Shapley are averaged per feature across the data and are sorted by decreasing importance. As can be seen, the stress amplitude (σ_a) is the one that exerts the greatest influence on temperature behavior, followed by N . With respect to N , it can be said that the longer the fatigue life of the material, the longer it will remain at a certain temperature that depend on which loading conditions are adopted.

Figure 39b presents the SHAP summary plot, which combines feature importance with feature effects. Each point on the summary plot is a Shapley value for a feature and an instance. While the vertical location shows what feature it is depicting, the horizontal location shows whether the effect of that value caused a higher or lower prediction. The color plot represents the feature range from low to high. This summary plot reveals the impact of each feature on every temperature prediction across the whole

test dataset. Greater values for stress amplitude have a higher influence on temperature increase while low values for stress amplitudes lead to a low impact on temperature rise throughout the VHCF test. As for the oscillation time, greater values of *tpulse* have a larger impact on the temperature rise. On the other hand, greater values of *tpause* contribute to lower values of temperature. As expected, *tpulse* and *tpause* significantly contribute to temperature behavior.

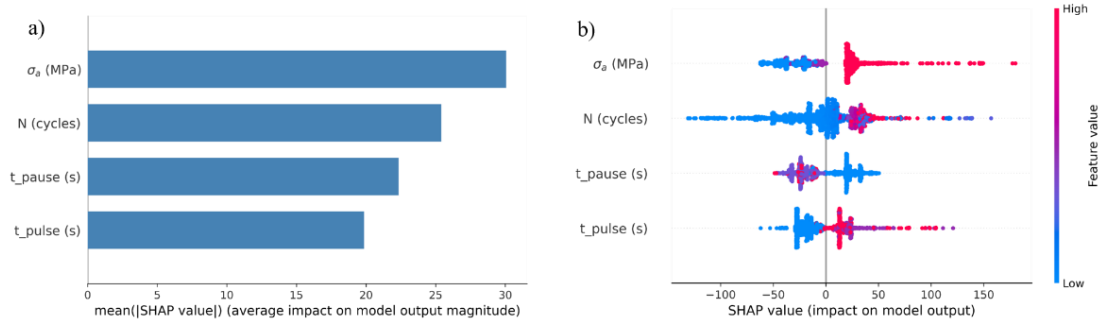


Figure 39: SHAP method: a) feature importance and b) summary plot.

7.3 S-N curve

In possession of the results presented in section 7.2.1 it was possible to define which test conditions better suffice in obtaining the S-N curve without a temperature effect. The intermittent loading conditions applied were 300 msec of pulse and 500 msec of pause.

Figures 40 – 41 exhibit the S-N curves obtained under $R = -1$ and room temperature (RT). It is observed of both of steels are classified as type II material. A high scatter in the results is indeed noticeable juxtaposing both materials. Even though the material still shows a fatigue tendency of having higher life for lower stresses in the VHCF regime, the applied stresses that caused fatigue failure in the VHCF regime are shown to be higher than expected for the two steels, mainly for DIN 42CrMo4. DIN 42CrMo4 achieved a run-out for 470 MPa, which is almost equivalent to 52 % of the ultimate tensile strength of the material. The values for the applied stress and number of cycles to failure can be seen in Table 6 and 7. For DIN 34CrNiMo6, the run-out was

reached for 440 MPa. In fact, two of the specimens' run-out did not fail under the action of stress higher than 440 MPa. Some specimens of DIN 34CrNiMo6 did not fail under higher stress levels, as presented in Table 6. The specimens of DIN 34CrNiMo6 demonstrated a lower fatigue strength compared to those of DIN 42CrMo4, although the materials have very similar mechanical properties. Nonetheless, an account for this discrepancy is the amount of metallurgical heterogeneities present in the steels under study. Amounts of inclusions were observed during the metallographic analysis, revealing a greater deal of inclusions in DIN34CrNiMo6 than 42CrMo4 (section 7.1).

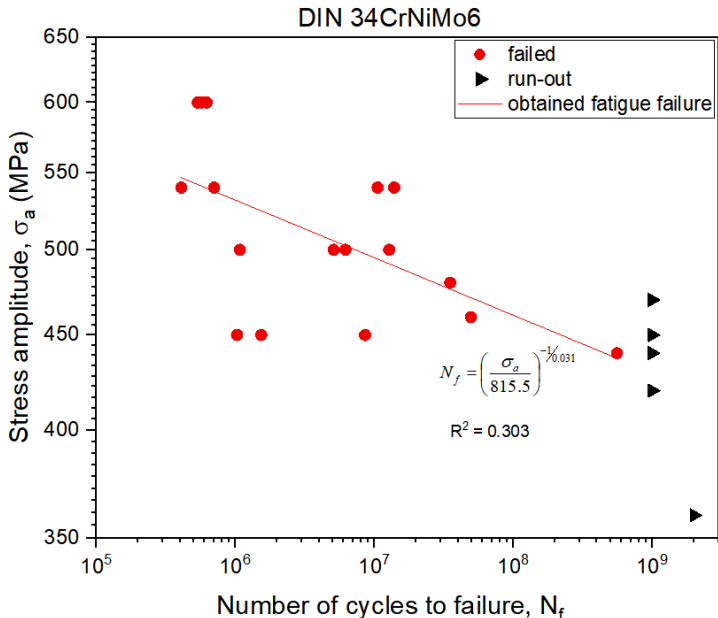


Figure 40:S-N for DIN 34CrNiMo6 steel.

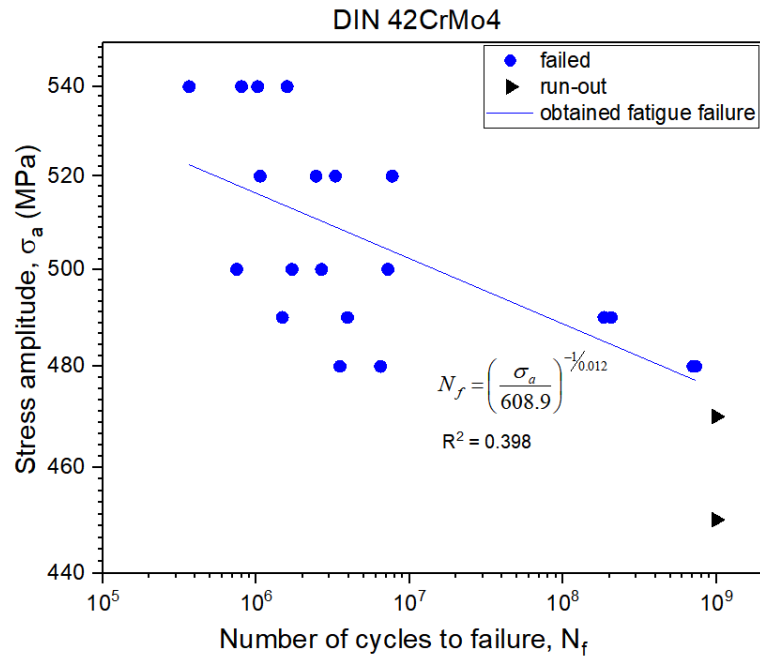


Figure 41: S-N for DIN 42CrMo4 steel.

Table 6: presents the stress applied and respective number of cycles to failure of DIN 34CrNiMo6.

DIN 34CrNiMo 6 - R = -1			
σ_a (MPa)	N_f (cycles)	σ_a (MPa)	N_f (cycles)
360	run out – 2E9	480	3.52E+07
420	run out – 1E9	500	6.22E+06
420	run out – 1E9	500	5.11E+06
440	run out – 1E9	500	1.08E+06
440	run out – 1E9	500	1.28E+07
440	5.58E+08	540	4.09E+05
450	1.03E+06	540	1.39E+07
450	run out – 1E9	540	7.04E+05
450	1.54E+06	540	1.06E+07
450	8.60E+06	600	5.75E+05
460	4.97E+07	600	5.37E+05
470	run out – 1E9	600	6.22E+05

Table 7: presents the stress applied and respective number of cycles to failure of DIN 42CrMo4.

DIN 42CrMo 4 - R = -1			
σ_a (MPa)	N_f (cycles)	σ_a (MPa)	N_f (cycles)
450	run out – 1E9	500	1.71E+06
470	run out – 1E9	500	7.21E+06
470	run out – 1E9	500	7.45E+05
470	run out – 1E9	500	2.66E+06
480	3.51E+06	520	1.06E+06
480	7.04E+08	520	7.70E+06
480	7.33E+08	520	3.28E+06
480	6.45E+06	520	2.45E+06
490	2.06E+08	540	8.00E+05
490	1.85E+08	540	3.64E+05
490	3.93E+06	540	1.02E+06
490	1.48E+06	540	1.59E+06

Subsequently, it was evaluating the accuracy of the predicted life with the experimental results. In the context of this, Figures 42 – 43 demonstrated the predicted life ($N_{f, pre}$) vs. experimental life ($N_{f, exp}$) with the 1:2 (red line) scatter bands (red line) to analyze the data from the Basquin equation. It was included the evaluation of 1:5 scatter bands due to the higher dispersive results, common in VHCF test.

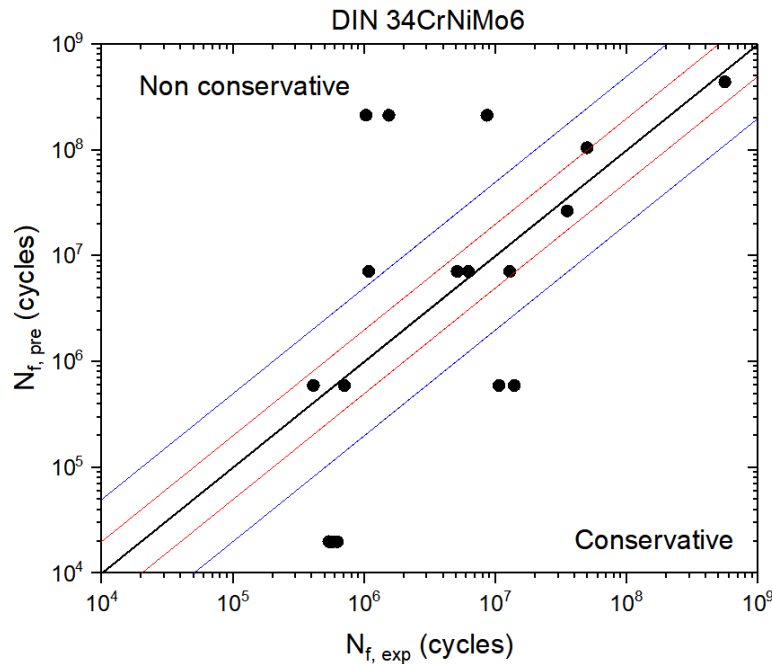


Figure 42: Comparative analysis of predicted life vs. experimental life of DIN 34CrNiMo6.

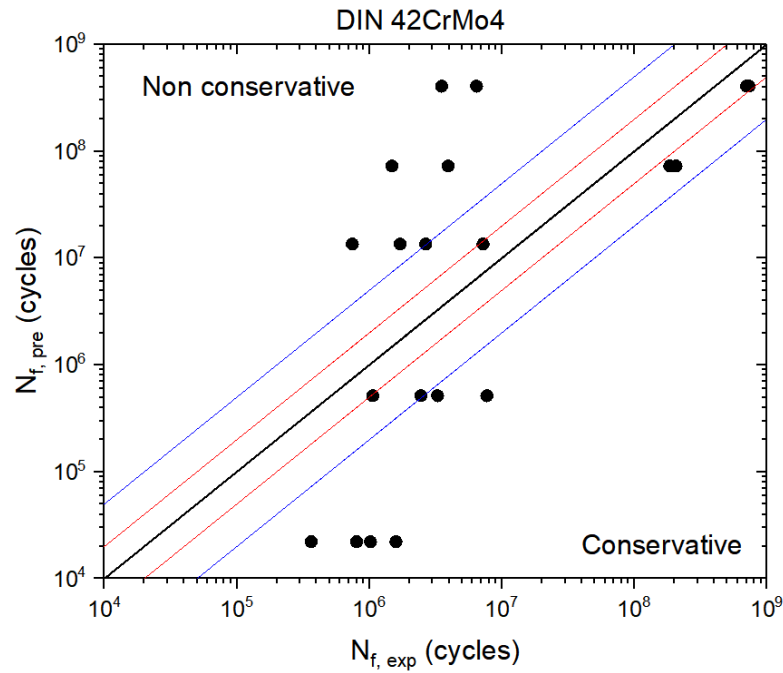


Figure 43:Comparative analysis of predicted life vs. experimental life of DIN 42CrMo4.

Aforementioned, the ultrasonic fatigue tests having higher scatter results and in spite of this the results of DIN 34CrNiMo6 provided the most of the predicted fatigue life data are within the 1:2 or 2:1 boundary and in conservative field. Already, DIN 42CrMo4 did not presented great theoretical data results, given that the data were divided in non-conservative and conservative field with little results inside the 1:5 scatter bands.

Tests with different loading ratios were also carried out and further compared with tests of fully reversed conditions and assess the crack initiation site. Figure 44 and 45 display the S-N curves with the applied stress for each material.

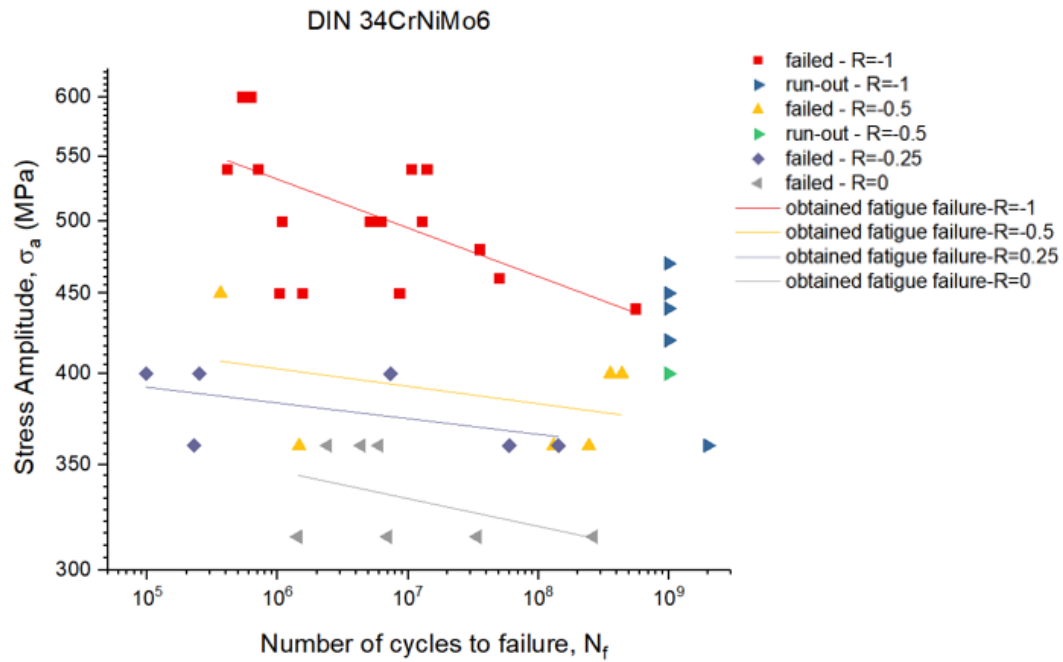


Figure 44:S-N curves of DIN 34CrNiMo6 for different loading ratios.

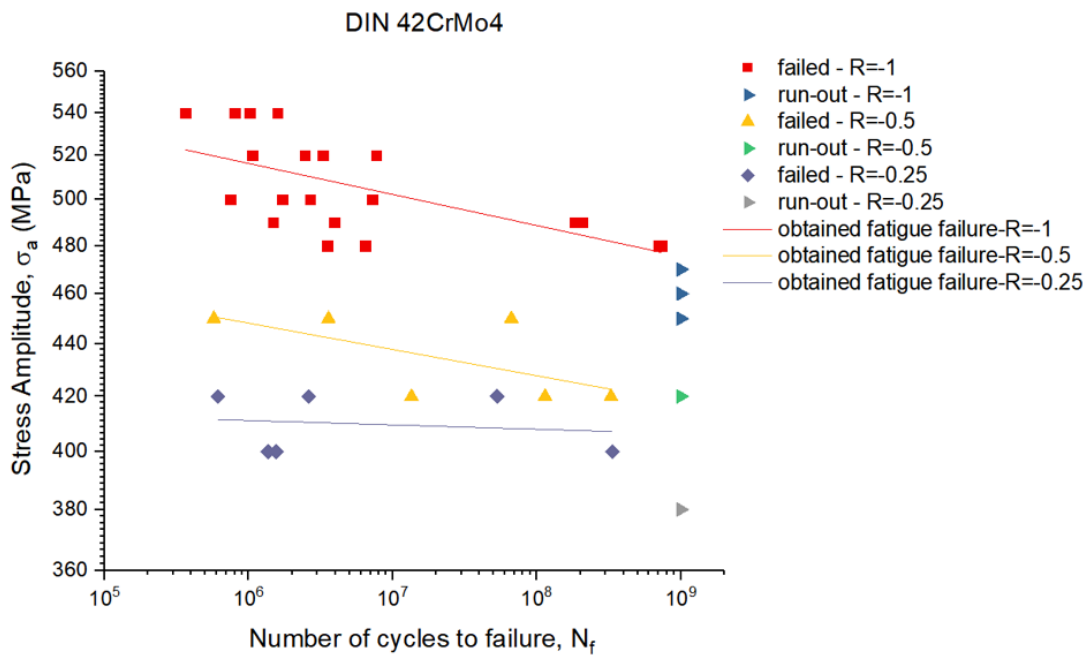


Figure 45:S-N curves of DIN 42CrMo4 for different loading ratios.

With the applied mean stress, the fatigue life of the material unsurprisingly decreased in both cases. Interestingly, DIN 42CrMo4 presented a greater fatigue strength seeing that some specimens reached the run-out even with higher stresses.

7.4 T-N curves

The second thermographic analysis was conducted in order to prove that the obtained results of the S-N curve did not display a temperature effect. Additionally, this data was used to estimate the R_{θ} and calculate the Q_{cyc} of each specimen that failed, and relate it to the number of cycles to failure. Figures 46 and 47 show the T-N curves of each steel. These curves were plotted until $5E+05$, to show the transition point between phase I and II. In both of cases the steady state is achieved around $5E+04$. The data taken from the T-N curves can be seen in the Tables 8 and 9.

The maximum and steady-state temperatures obtained are in line with expectations. The test temperature increases with an increase of σ_a . For DIN 34CrNiMo6 steel the maximum temperature measured was 34.28°C and for DIN 42CrNiMo4 steel approximately 35°C .

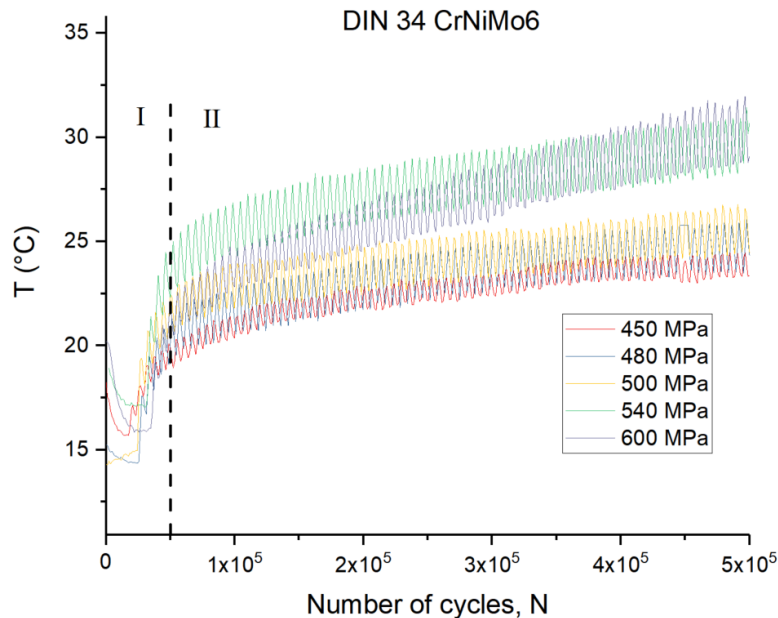


Figure 46: T-N curves until $5E+05$ cycles of DIN 34CrNiMo6.

Table 8: Data obtained from T-N curves of DIN 34CrNiMo6.

DIN 34CrNiMo6					
σ_a (MPa)	T_{max} (°C)	T_{SS} (°C)	ΔT (°C)	R_θ (°C/cyc)	Number of cycles
450	24.89	19.83	2.83	5.21E-05	-
480	26.18	24.52	7.52	6.60E-05	3.52E+07
500	31.77	28.01	11.01	9.90E-05	1.28E+07
540	32.29	30.06	13.06	1.03E-04	1.06E+07
600	34.28	29.40	12.40	1.05E-04	6.22E+05

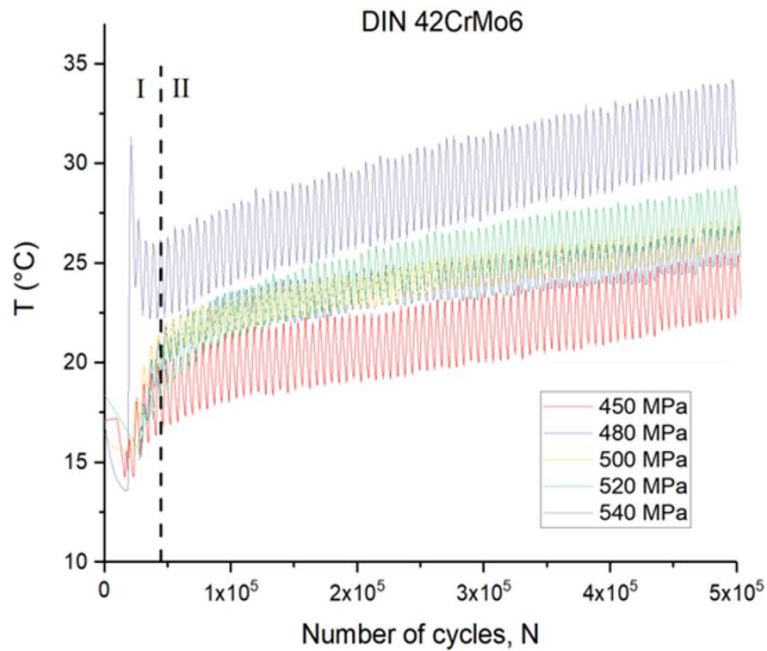


Figure 47: T-N curves until 5E+05 cycles of DIN 42CrMo4.

Table 9: Data obtained from T-N curves of DIN 42CrMo4.

DIN 42CrMo4					
σ_a (MPa)	T_{max} (°C)	T_{SS} (°C)	ΔT (°C)	R_θ (°C/cyc)	Number of cycles
450	24.84	21.22	4.22	5.58E-05	-
480	27.09	24.67	7.67	7.26E-05	6.45E+06
500	28.23	25.32	8.32	7.89E-05	2.66E+06
520	31.38	27.10	10.10	8.29E-05	2.45E+06
540	35.37	29.39	12.39	9.70E-05	1.59E+06

7.5 Fatigue Damage Parameters

7.5.1 R_{θ}

The estimated R_{θ} were plotted in a bars diagram with the σ_a (Figure 48a and 48b). It was observed that the increase in R_{θ} was gradual and increases with an increase of σ_a . For DIN34CrNiM6 steel there was a greater increase between the stresses of 480 - 500 MPa and for the following stresses there was practically no discrepancy.

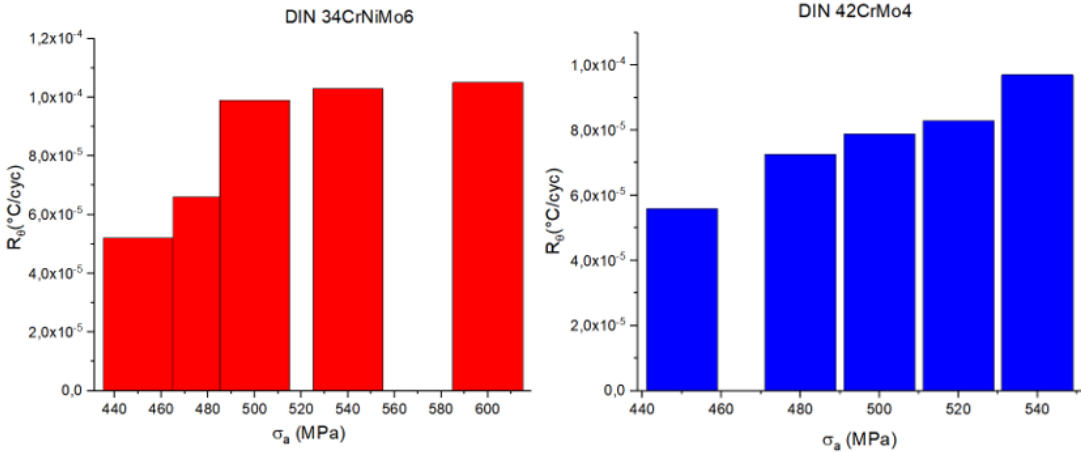


Figure 48: Bars diagram R_{θ} versus σ_a .

According to Amiri e Khonsari [84], the R_{θ} is the parameter which provides fast prediction failure. The R_{θ} related to the N_f can be observed in Figure 50. The constants of Equation 20, c_1 and c_2 are $3.47E-04$ and -0.085 of DIN 34CrNiMo6 with the $R^2 = 0.45$. Already, in steel DIN 42CrMo4 c_1 is $1.38E-03$ and c_2 equal to -0.19 with R^2 around 0.84. The reliability of the theoretical results was assessed as demonstrated in Figures 42-43. It can be observed in Figure 51, that predicted life of DIN 42CrMo4 had a better accuracy than DIN 34CrNiMo6. All data of DIN 42CrMo4 are within the 1:2 and 2:1 boundary, therefore data of DIN 34CrNiMo6 had a 50% inside the 1:5 scatter bands.

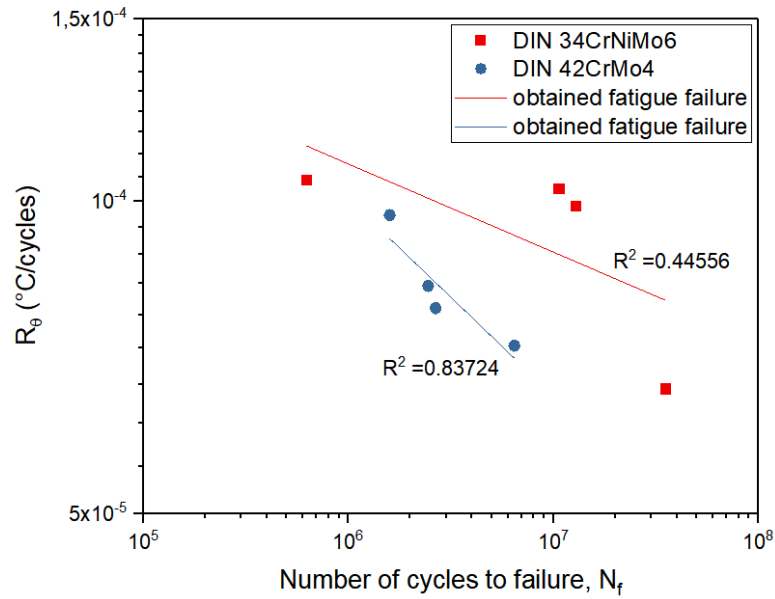


Figure 49: R_{θ} vs N_f .

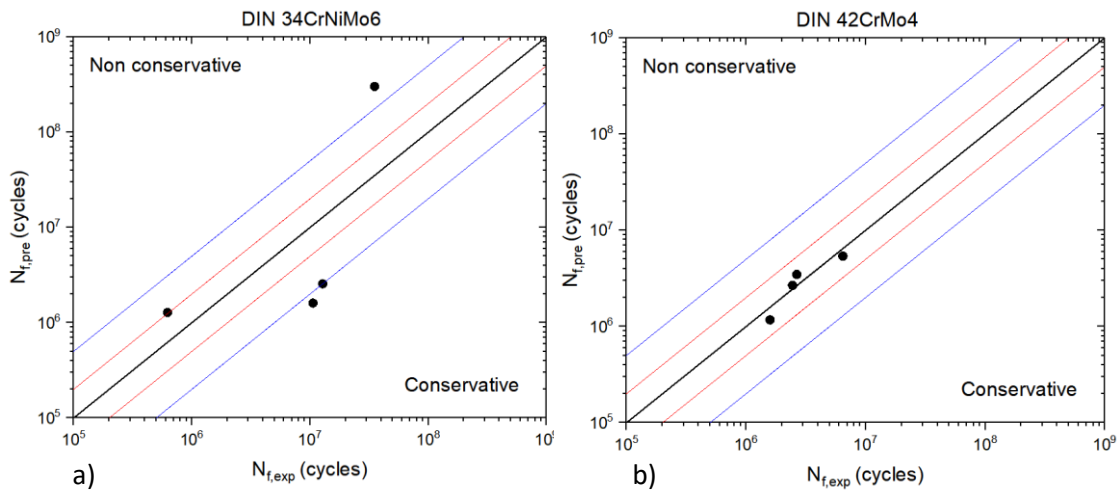


Figure 50: Comparative analysis of predicted life and experimental life of a) DIN 34CrNiMo6 and b) DIN 42CrMo4.

7.5.2 Q_{cyc}

Heat dissipation was calculated for each specimen that failed. In the first diagram it is display the Q_{cyc} versus N_f in Figure 51. Q_{cyc} was calculated using the R_{θ} data from tables 8 and 9. The determination coefficients (R^2) were obtained with the fit

curve. Despite the paucity of data, the R^2 of DIN 42CrMo4 steel was approximately 0.84 unlike of DIN 34CrNiMo6 which had around 0.45. Notice that R_θ and Q_{cyc} have the same value of the exponent in the first diagram, seeing as Q_{cyc} depends on R_θ in its calculations.

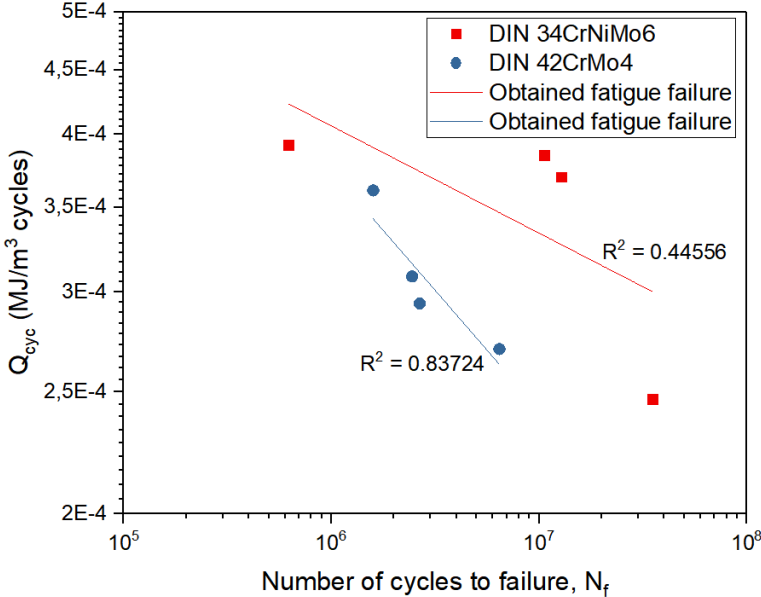


Figure 51: Q_{cyc} vs. N_f .

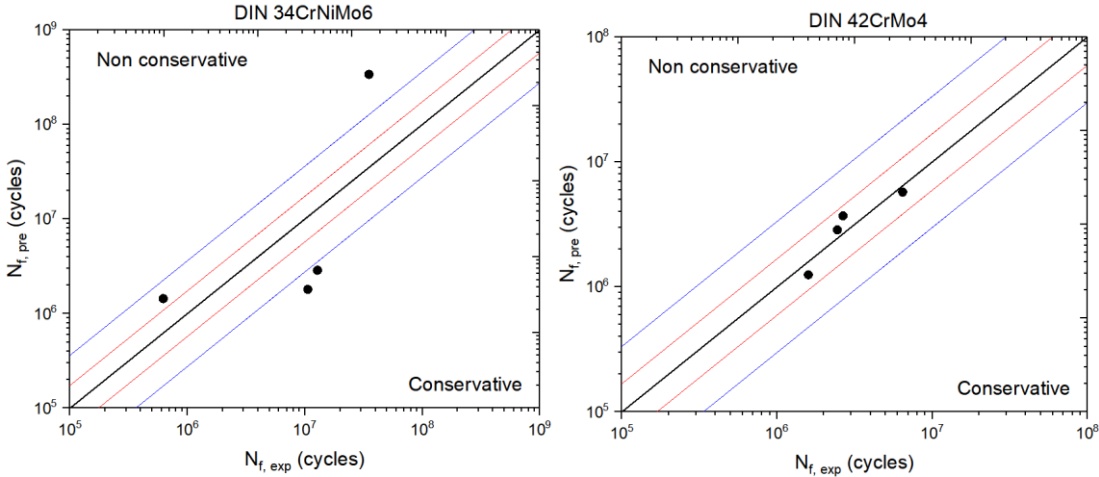


Figure 52: Comparative analysis of predicted life and experimental life of a) DIN 34CrNiMo6 and b) DIN 42CrMo4.

Figure 51 shown that Q_{cyc} decreases when the number of cycles increase, as in agreement of the literature [74,85]. It was obtained the fatigue function as $Q_{cyc}=C$

$(N_f)^m$, where C and m are constants of the material. For the materials under study were encountered C and m values equal to 0.0052 and -0.19 of DIN 42CrMo4, 1.31E-04 and -0.085 of DIN 34CrNiMo6.

A comparative analysis was conducted to assess the accuracy of the theoretical fatigue life achieved using the fitted curve in Figure 51. As observed in previous section that DIN 42CrMo4 reached a good reliability in comparison of DIN 34CrNiMo6 and it is observed the same behavior in Figure 52. However, DIN 34CrNiMo6 displays more conservative.

7.5.3 ΔT

Fargione and Jiang [86,87] proposed to use the ΔT to predict the fatigue life. As $\Delta T = T_{ss} - T_0$, it is inapt for tests do not have the steady state.

To use the constant applicable in Equation 19 it is necessary, at least, 2 curves with steady state in objective to compare and verify if is the same.

Table 10 provides the results of Fargione's formulation. Noticeable, the ϕ values for DIN42CrMo4 steel are in the same order of magnitude. The N_f of these specimens have the same magnitude and this exerts a high influence in ϕ values. However, three out of four values of ϕ in DIN34CrNiMo6 steel, presented N_f in the same order and leading the ϕ to the same magnification. The last specimen of DIN34CrNiMo6 had a totally different ϕ . Fargione's models demonstrated that there is no constant value for VHCF testing, indicating variability.

Table 10: Constant ϕ Fargione' s equation.

DIN 34CrNiMo6			
σ_a (MPa)	Number of cycles	ΔT (°C)	ϕ
480	3.52E+07	7.52	2,65E+08
500	1.28E+07	11.01	1,40E+08
540	1.06E+07	13.06	1,39E+08
600	6.22E+05	12.40	7,71E+06
DIN 42CrMo4			
σ_a (MPa)	Number of cycles	ΔT (°C)	ϕ
480	6.45E+06	7.67	4,94E+07
500	2.66E+06	8.32	1,32E+07
520	2.45E+06	10.10	2,47E+07
540	1.59E+06	12.39	3,30E+07

Using the Jiang model, Figure 53 present the obtained diagrams with the determination coefficients. Again the steel in red had worst fit. A comparative analysis for this model was not carried out because presented the worst fit in comparison with the Q_{cyc} and R_{θ} models using in the previous sections.

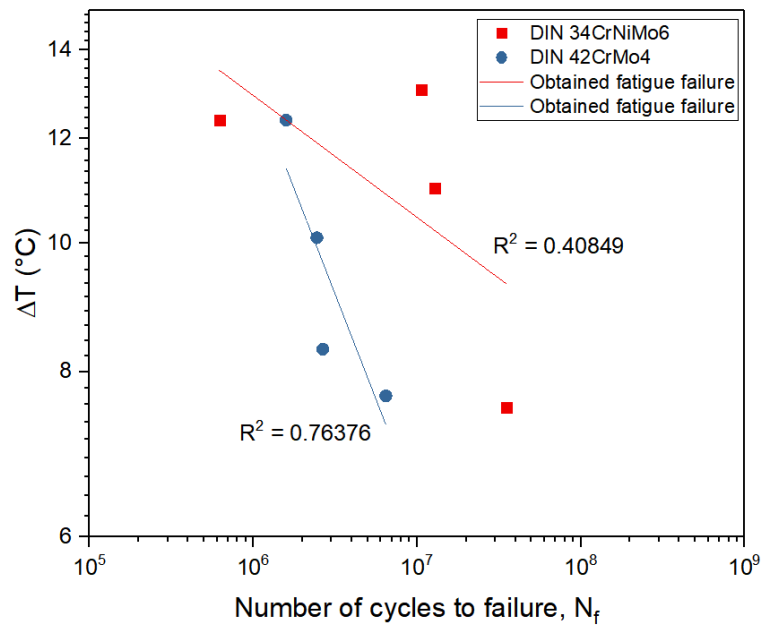


Figure 53: ΔT vs. N_f .

7.6 Microplasticity

As the HCF regime the crack initiations are microscopically and VHCF have the same behavior, the plastic strain deformation is localized (microscopically). This study assumes that it is also applicable the Coffin-Manson-Basquin law in the microscopic scale. Table 11 and 12 demonstrate the obtained values of $\epsilon_{a,p}$, and $\epsilon_{a,p}^{\mu}$ for the same experimental test conditions in Tables 8-9.

Table 11: Microplasticity strain amplitude of DIN 34CrNiMo6 results.

σ_a (MPa)	N_f (cycles)	$\epsilon_{a,p}$	$\epsilon_{a,p}^{\mu}$
450	1.54E+06	6.93E-05	1.53E-07
480	3.52E+07	9.95E-06	2.83E-07
500	1.28E+07	1.87E-05	2.62E-07
540	1.06E+07	2.09E-05	1.48E-07
600	6.22E+05	1.22E-04	2.32E-07

Table 12: Microplasticity strain amplitude of DIN 42CrMo4 results.

σ_a (MPa)	N_f (cycles)	$\epsilon_{a,p}$	$\epsilon_{a,p}^{\mu}$
480	1.54E+06	7.64E-05	1.53E-07
500	3.52E+07	1.29E-04	2.83E-07
520	1.28E+07	1.36E-04	2.62E-07
540	1.06E+07	1.75E-04	1.48E-07

The values are in agreement with presented by Mughrabi in the literature [30-32]. Microplasticity obtained by law of localization and homogenization which use the energy dissipation, present values almost constant and less than Coffin-Manson-Basquin law. Knowing the $f_{eff} = 7521.63$, $\tau = 1/f_{eff} = 1.33E-04$, the microplasticity strain rate using Coffin-Manson-Basquin law varied 10^{-5} and $10^{-6} s^{-1}$ for DIN 34CrNiMo6 and $10^{-5} s^{-1}$ for DIN 42CrMo4. On the other hand, $\epsilon_{a,p}^{\dot{\mu}}$ is around $10^{-8} s^{-1}$ for both steel.

In the face of these results, an interest was aroused in low frequency test and compare the results to obtain better comprehension of frequency effect associated with the microplasticity strain. Low frequency tests in 10 Hz were performed and it was chosen the same stress levels for each steel. Table 13 presents these results for each steel with microplasticity strain attained by Coffin-Manson-Basquin law.

Table 13: Results at low frequency test.

DIN 34CrNiMo6		
σ_a (MPa)	N_f (cycles)	$\epsilon_{a,p}$
450	1,44E+05	3.01E-04
500	1,02E+05	3.73E-04
600	6,88E+03	1.93E-03
DIN 42CrMo4		
480	1,04E+05	2.63E-03
500	1,20E+05	2.41E-03
540	2,05E+06	4.53E-04

It is noticeable the discrepancy of the microplasticity strain between VHCF and conventional test. In low frequency test the $\epsilon_{a,p}$ is around $10 - 10^2$ orders of magnitude higher than VHCF tests, depending on the stress level.

Additionally, it was calculating the cyclic strain rate according to Equation 25. Table 14 show the cyclic strain rate for low frequency at 10 Hz, the f_{eff} for intermittent loading used to obtain the S-N curves and for 20 kHz.

$$\dot{\epsilon} = 4 \frac{\sigma_a}{E} f \quad (25)$$

Table 14: Cyclic strain rate.

DIN 34CrNiMo6			
σ_a (MPa)	10 Hz	7,521 Hz	20,000 Hz
450	0.087	65.400	173.913
500	0.097	72.667	193.237
600	0.116	87.200	231.884
DIN 42CrMo4			
480	0.092	69.092	183.732
500	0.096	71.971	191.388
540	0.103	77.729	206.699

The cyclic strain rate increases considerably in ultrasonic frequency. These results proved frequency effect of these steel and the strain rate dependence should not be negligible.

7.7 Fracture surfaces

Aforementioned, fatigue crack in VHCF can arise on the surface, in subsurface or internally. Crack initiation have occurred in the three cases and it was chosen for each material, crack initiation on the surface and from interior of the specimen.

The fracture surfaces were analyzed in SEM, using two detectors. Additionally, energy dispersive spectroscopy (EDS) was used to identify the elements present in a non-metallic inclusions and a third analysis using focused ion beam (FIB). In this section will be presented an interior and surface crack initiation for each material.

Figures 54 – 57 show the crack surfaces of the steel DIN 34CrNiMo6. Figure 54 presents the fracture surface with crack initiation as indicate with yellow narrow. This specimen failed at $1.4E+07$ cycles under 540 MPa in fully reversed condition. In contrast Figure 55 shows the fish-eye feature, highlighted with a yellow narrow. Figure 55b can be seen fish eye obtained in magnification around 450x.

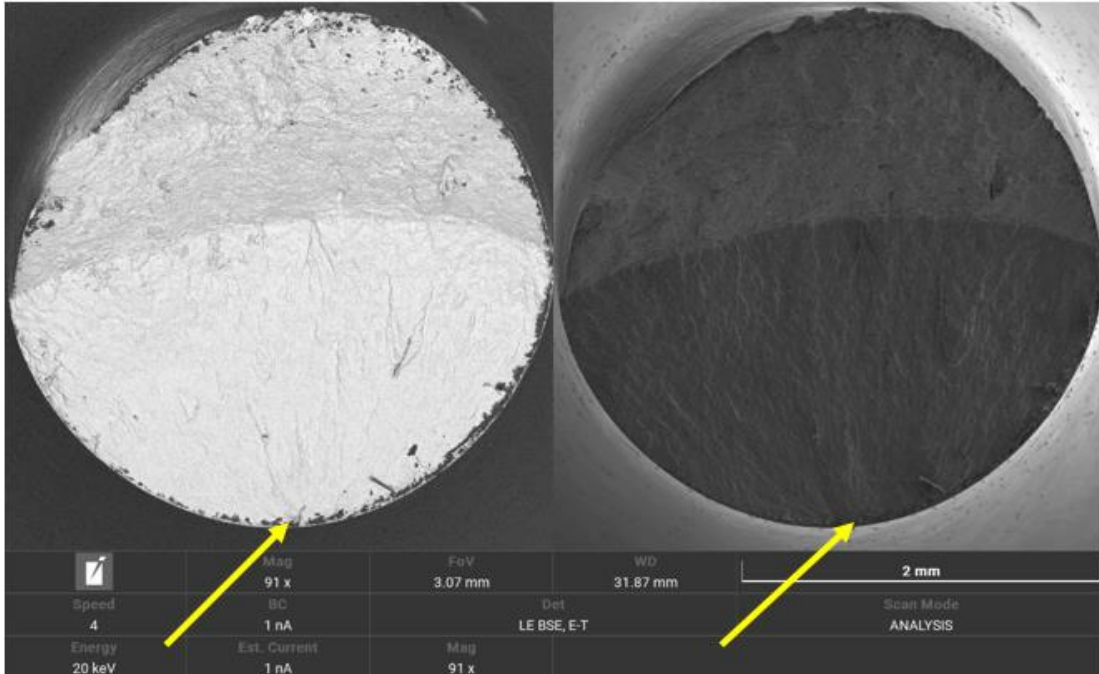


Figure 54:Fracture surface with crack initiation at the surface.

Figure 56 detail the same fish-eye as the Figure 55, but detected by backscattered electrons. In this image is clear to see the smooth surface in contrast the crack growth outside fish-eye. This specimen failed at $5.97E+07$ cycles with stress amplitude 360 MPa in loading ratio equal to -0.25. This fish-eye has a diameter around $358 \mu\text{m}$. FGA was identified and its diameter is approximately $160 \mu\text{m}$. Figure 57, details the FGA region in two magnifications 1k x and 5k x.

A K_{max} of FGA and fish-eye was calculated according to the Equation 16. It was encountered $3.63 \text{ MPa m}^{1/2}$ and $5.43 \text{ MPa m}^{1/2}$.

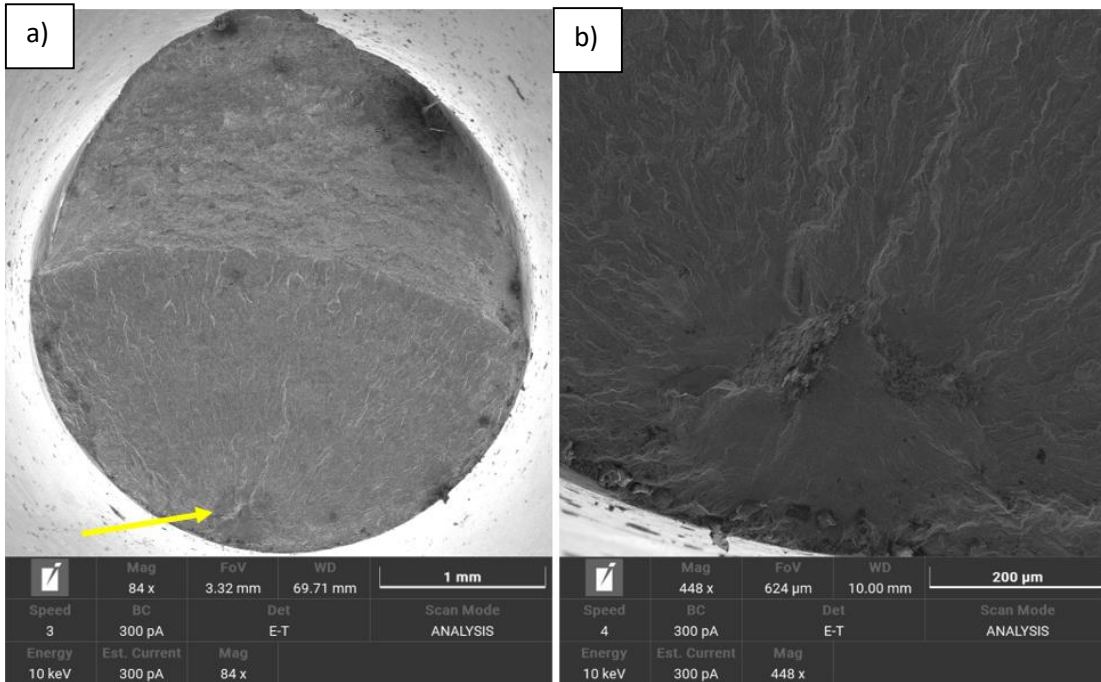


Figure 55: Subsuperficial crack initiation from non-metallic inclusions.

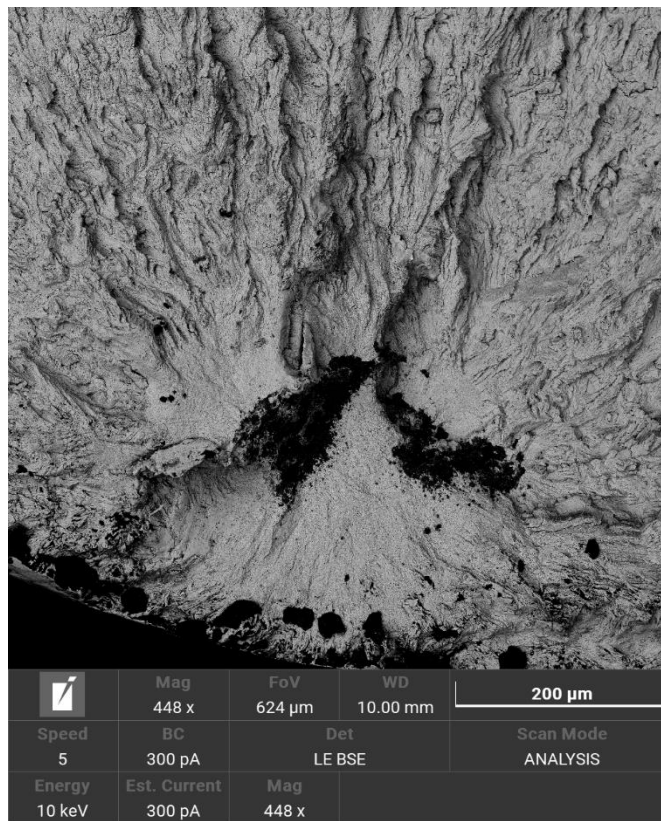


Figure 56: Fisheye image by backscattered electrons detector.

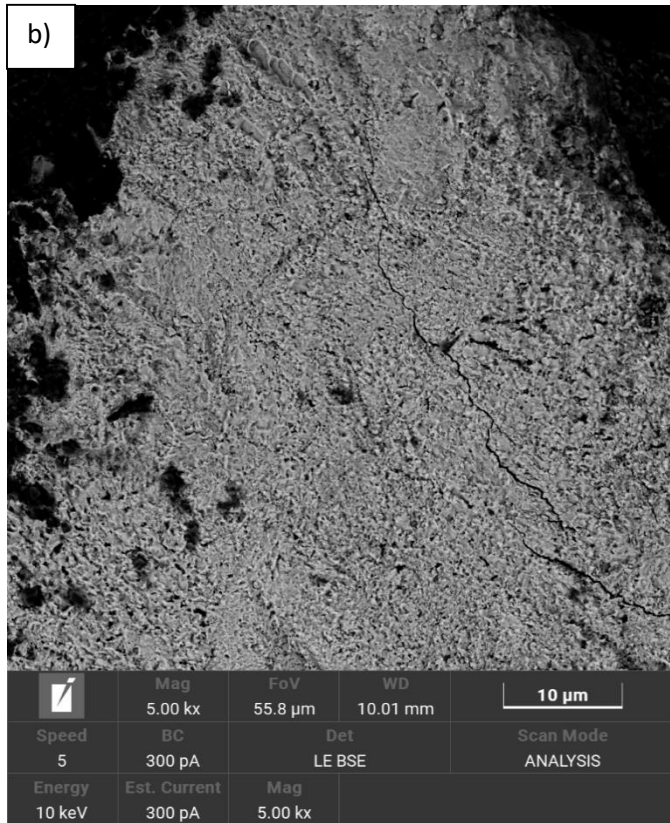
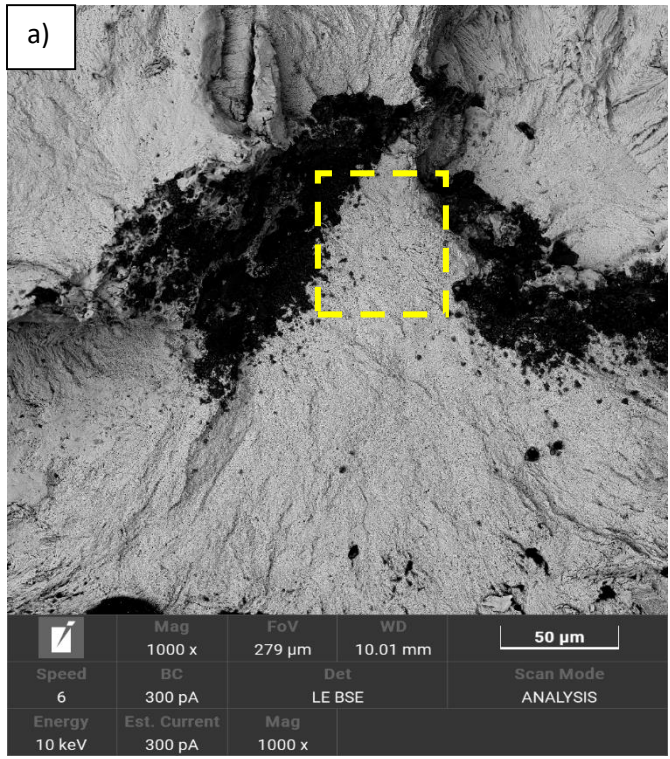


Figure 57: FGA region: a) 1000 x, b) 5000 x.

Subsequently, images of DIN 42CrMo4 steel. Figure 58 present fracture surface with fish-eye which is highlighted in dashed circle, beside a non-metallic inclusion is indicated by yellow narrow and the FGA region.

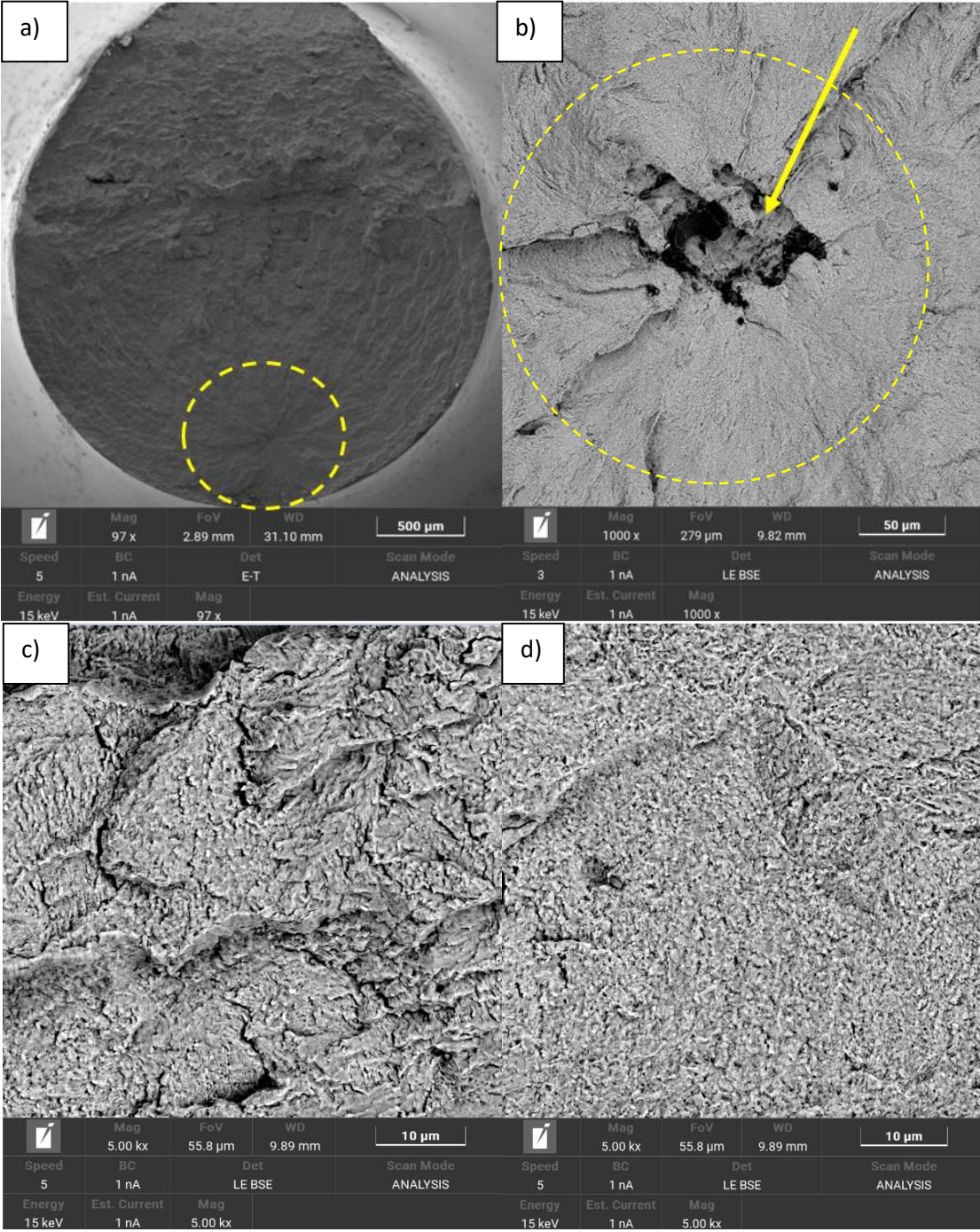


Figure 58: a) Fracture surface with crack initiation from the interior inclusion, b) highlighted of FGA and inclusion, c) aspect of fish-eye surface and d) aspect of FGA surface.

The magnifications of the fish eye and FGA surfaces are shown in Figures 58c and d. The difference between the surfaces are evident. Fish eye and FGA diameters were estimate and encountered values 840 μm around 284 μm . This specimen was tested with $R = -0.5$, stress amplitude of 420 MPa and had fatigue life in $3.27\text{E}+08$. K_{max} of fish-eye and FGA was calculated for this specimens and obtained $9.71 \text{ MPa m}^{1/2}$ and $5.64 \text{ MPa m}^{1/2}$.

Specimens failed in 490 MPa for $R = -1$ had N_f around 10^6 and 10^8 cycles. The four specimens at this stress level had nucleated cracks on the surface. Figures 59a and b referred a specimen failed in $3.93\text{E}+06$ and Figures 59c and d had fatigue life in $1.85\text{E}+08$.

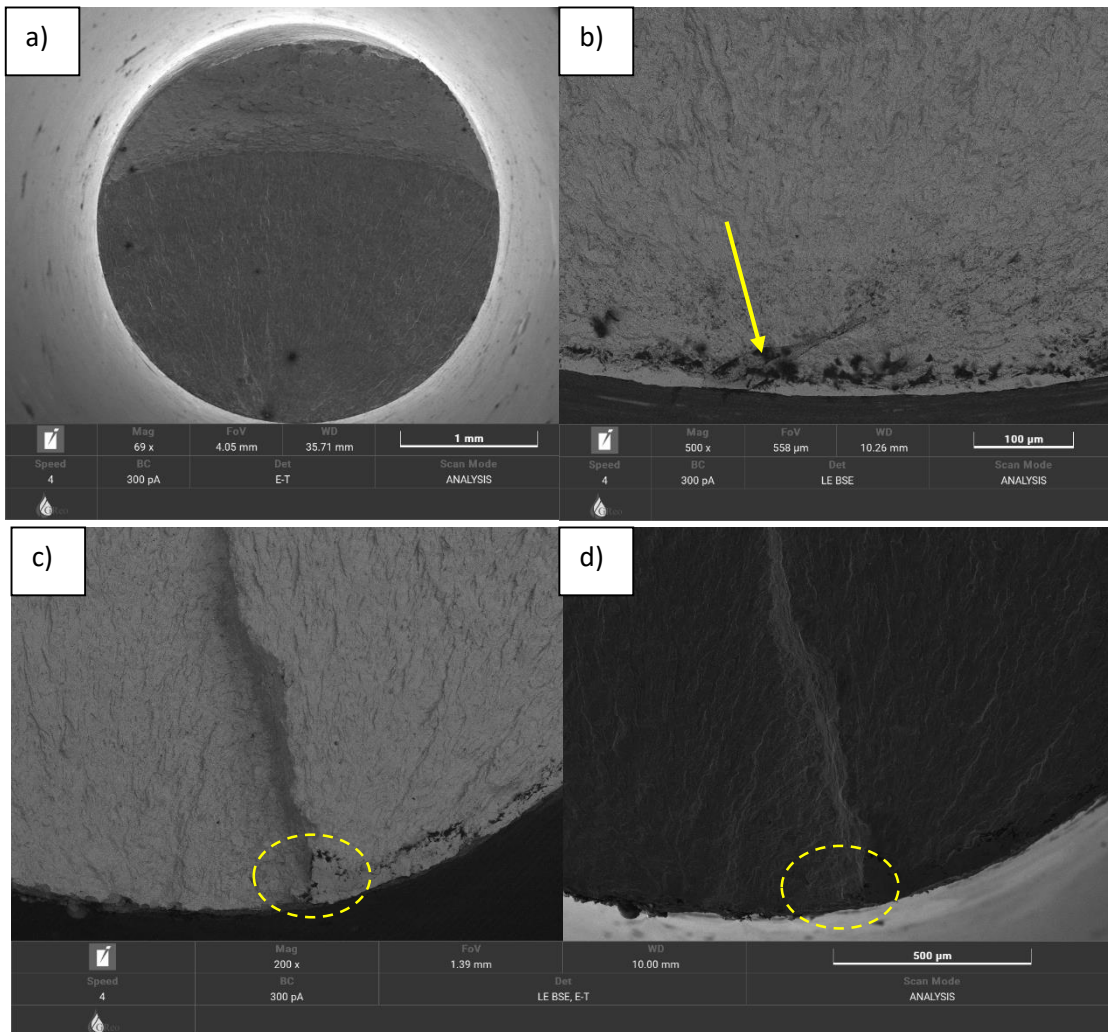


Figure 59: a) Entire fracture surface, b) crack initiation site of a), c) image of crack initiation site by backscattered electrons and d) the same of c) obtained by secondary electrons.

An EDS were used to verify the elements and to identify the type of a non-metallic inclusions. In both materials, oxygen and aluminum were found in greater amounts, as can be seen in Figure 60.

The presence of these elements indicates inclusions of the type Alumina (Al_2O_3).

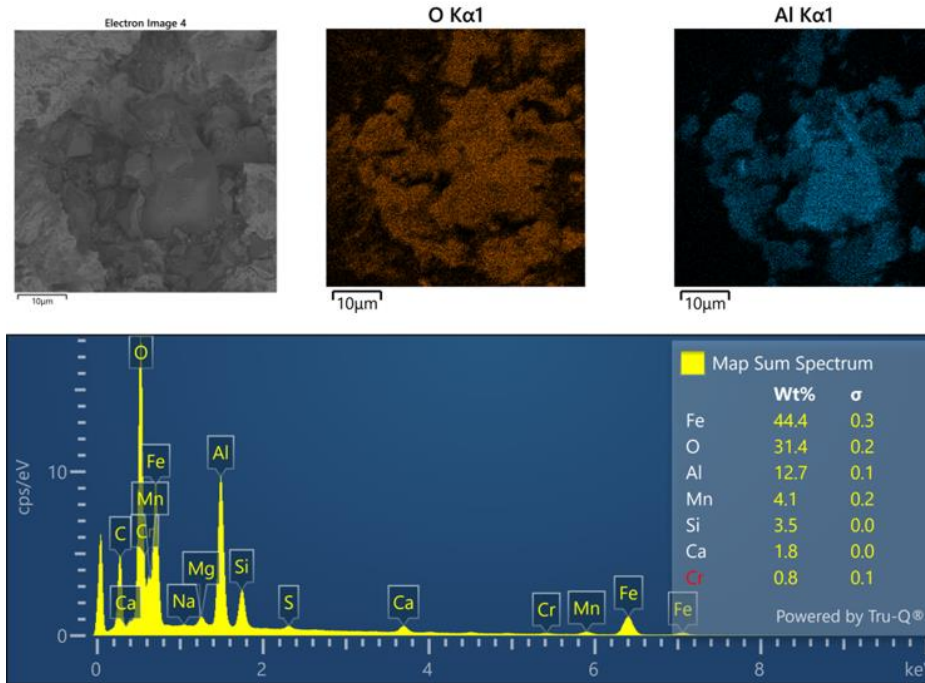


Figure 60: EDS of DIN42CrMo6.

Moreover, two specimens that failed in VHCF region and had fracture surface with FGA, were analyzed using FIB. A cross-sections were performed in FGA region.

The specimen of DIN 42CrMo4 steel which failed in $7.33E+08$ with σ_a 480 MPa, had a subsurface crack initiation. Figure 61a e b show the site where the laser was applied and cross-section, respectively. In figure 61b, it is possible to observe the fine grains region, highlighted with yellow dashed ellipse. Fine grains formations were identified in up to 700 nm bellow the fracture surface.

In FIB applied in DIN 34CrNiMo6 steel, had crack initiation site internally. This specimen was cyclic at 360 MPa with $R = -0.5$ and had fatigue life $2.44E+08$. Figure 62a shows the fish-eye region Figure 62b the lamella retired near to crack

initiation site (FGA region). Again, fine grains were observed. This lamella was analyzed in EBSD to have a better visualization of the fine grains.

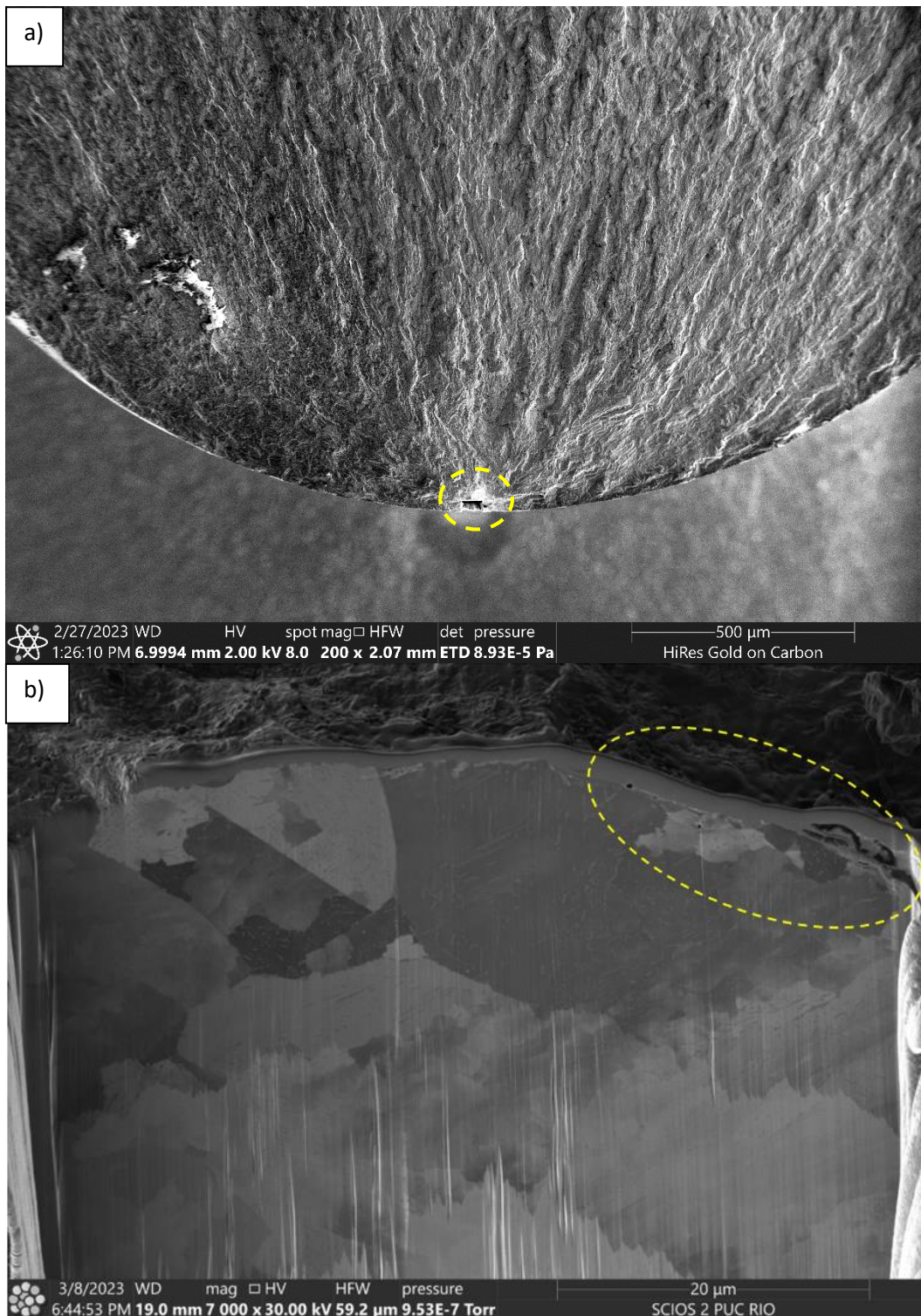


Figure 61: a) fracture surface with the cross made nearby the surface and b) cross-section of the specimen.

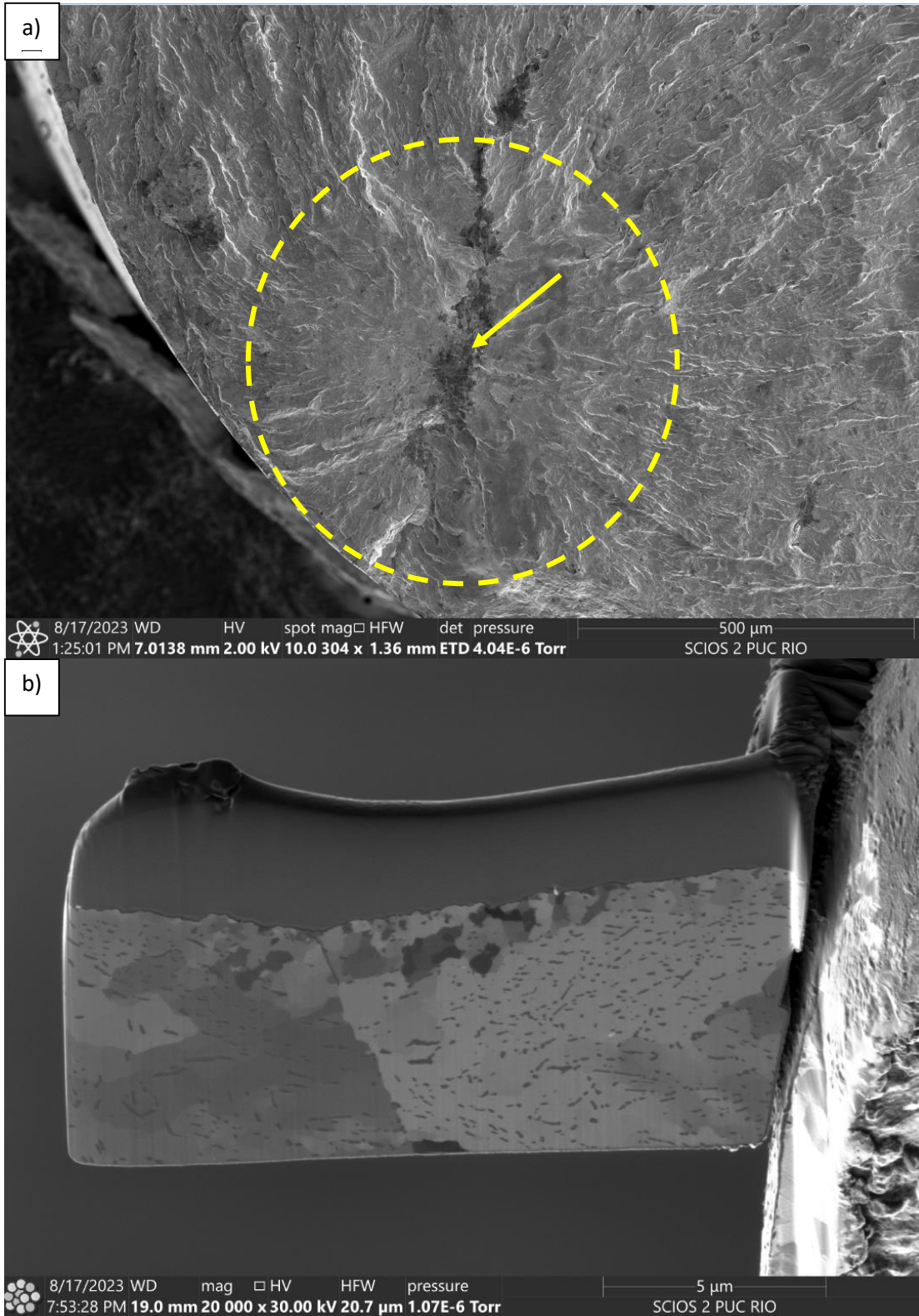


Figure 62: a) fracture surface obtained with FIB analysis, b) lamella.

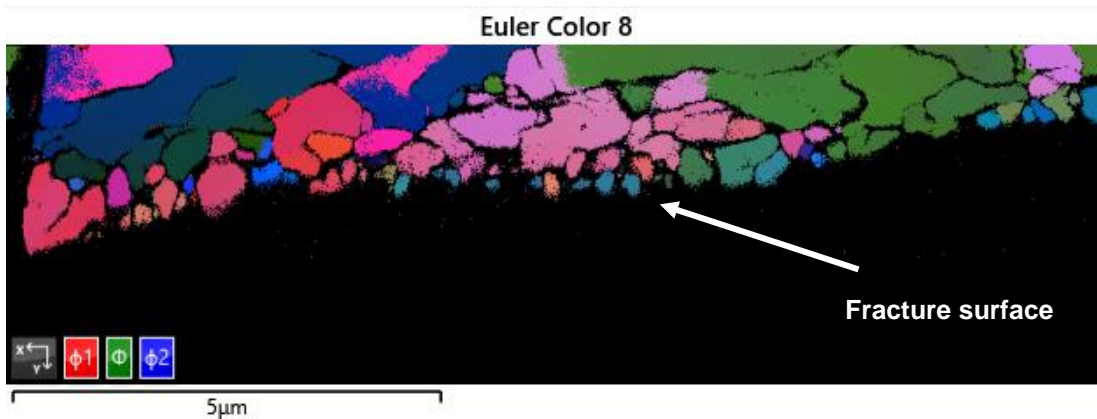


Figure 63: a) lamella of FGA regions after EBSD analysis (Euller map).

It is clear, in Figure 63, the discontinuous layer just below the surface with ultrafine grains. A FGA secondary cracks was observed along the layer. The difference of the ultrafine and coarse grains in the matrix can be verify too.

8 Conclusions

In this study, experimental data from VHCF tests was used for the development of a machine learning model based on an ensemble extreme gradient boosting algorithm, the XGBoost. Different models were trained and a SMBO/TPE/EI optimization strategy was used to select the optimal XGBoost hyperparameters. The best model was able to predict the VHCF temperature with R^2 values above 0.98 for the training, validation and testing subsets. The performance metric, RMSE, suggests that model error is within the data variance, being about 500x smaller than the experimental data variance and confirming the reliability of the model.

Based on the learning curve and also on the comparison of observed and predicted values, it can be said that the model presented high efficiency, managing to generalize the data even for the highly non-linear cases.

Model interpretation reveals that the stress amplitude is the most important feature to predict the VHCF temperature and that greater values of σ_a have a higher

influence on the temperature increase. This behavior occurs for all other features, with the exception of t_{pulse} , wherein greater values lead to lower temperature values.

The proposed model makes possible to estimate the temperature (T-N curve) from the test conditions in VHCF, making it an important tool to define which test conditions should be used to avoid overheating specimens.

With the modelling results, S-N curves were obtained using $t_{\text{pulse}} - t_{\text{pause}}$ equal 300 and 500 msec. Thermographic tests at this effective frequency confirmed that the specimens did not suffer the self-heating effect, reaching a maximum temperature of 35 °C. From the T-N curves, it was observed that the transition from phase I to phase II, where the steady state temperature is achieved, occurred in approximately $5E+04$ cycles (around 6 sec.).

The S-N curves for the two materials in the loading condition equal to -1, showed high fatigue strength, reaching 10^9 cycles with stress amplitudes equivalent to 50% of the LRM or more. For DIN 34CrNiMo6 steel, specimens with 40% of the LRM, i.e. 360 MPa reached 2 billion cycles and did not fail. DIN 34CrNiMo6 contain more heterogeneities than DIN 42CrMo4 which explain the difference of the fatigue strength even these materials having an equivalent microstructure and mechanical properties. These results also indicate a possible frequency effect. Although the scatter results, DIN 34CrNiMo6 steel presented theoretical results of N_f around 50 % reliability. Already, DIN 42CrMo4 presented 50% of theoretical data results in the conservative field.

The value of the microplasticity strain was calculated for the Coffin-Manson-Basquin and the homogenization and localization law. Based on the observed results, 6 specimens were tested at low frequency, 10 Hz, and compared with the value obtained at 20 kHz. It was noticed that the microplasticity strain in 10 Hz tests are approximately 100 - 1000 x higher than 20 kHz. A cyclic strain rate was estimated including 3 frequencies and compared. It was clear that both steel was subjected to frequency effect. Accordingly, at 20 kHz, a maximum strain rate of $\dot{\epsilon} = 230 \text{ s}^{-1}$, and at 10 Hz, a maximum strain rate of $\dot{\epsilon} = 0.116 \text{ s}^{-1}$ reached.

Models based on temperature increase were calculated from the results obtained from the T-N curves. For each conditions, R_{θ} , Q_{cyc} , ΔT were expressed in terms of number of cycles according to the literature for tests at low frequency. In addition, the constant ϕ were calculated following the Fargione's model. In all results different constants were found, however in the same order of magnitude. For the other equations, the number of cycles to failure were estimated and compared with the experimental results. The better agreement with the experimental results was provided by R_{θ} followed by Q_{cyc} . These techniques are only demonstrated for low frequency test and R_{θ} , Q_{cyc} show that can be also used as fatigue damage parameter for ultrasonic fatigue tests. DIN 42CrMo4, in these cases, had more reliable results than DIN 34CrNiMo6. Fargione and Jiang models showed are inapt for VHCF test according to results with the materials under this study.

Both crack initiations from the surface and initiations from the inner region of the material were found. All internal initiations were from non-metallic inclusions. In the EDS performed for the samples of the two steels, it was found the non-metallic inclusion Alumina (Al_2O_3), which probably appeared during the manufacturing process and formed as agglomerates of aggregated particles. Even a both steel presented sulfides, only Alumina was responsible for internal crack initiation.

Fracture surfaces with different crack initiations were encountered. FGA and fish-eye regions were explored and calculated the K_{max} for each morphology. The K_{max} values obtained for FGA are in concordance of the threshold intensity factor for high strength steels in the literature and can be considered as the threshold for short crack growth. In Specimens of DIN 34CrNiMo6 tested with $R = 0$ did not observe the fatigue crack initiation from internal defects.

Focused Ion Beam were performed on 2 samples which have FGA region. Fine grains were identified up to approximately 700 nm in depth with the DIN 42CrMo4 specimen and 500 nm for DIN 34CrNiMo6, which is in agreement with the literature. EBSD analysis in the lamella obtained from DIN 34CrNiMo6 was performed and were visualized the ultrafine grains nearby the fracture surface. Below the FGA regions it was observed coarse grains.

This author, after this work, believes that the model better explain the FGA formation is “local grain refinement” by Grad et al. As it was not possible to carry out tests with positive loading conditions, the NCP model cannot be proven. However, this author considers a possible model for explanation the FGA morphology.

9 Suggestion for future work

This study addressed various aspects of Very High Cycle Fatigue (VHCF) testing. However, further tests using different steels and alloys are required to enhance our understanding of the effects of frequency and temperature.

The use of temperature based models has been well established in the literature for low frequency tests. For future tests, we recommend using a larger number of specimens, accompanied by infrared thermography until failure occurs. This will yield more results and help validate the models in the VHCF regime.

It is still necessary to identify the mechanism responsible for the formation of FGA regions. To achieve this, it is recommended to perform tests in a vacuum environment with specimens machined to introduce stress intensification in the middle. Analyzing these specimens using SEM, FIB, EBSD, and TEM is essential to confirm the presence of fine grains. It is suggested to carry out specimens in VHCF test with positive loading conditions ($R > 0$).

10 References

- [1] Suresh, S. *Fatigue of Materials*, New York: Cambridge University Press, 1998.
- [2] Downing, N. E. *Mechanical Behavior of Materials: Engineering Methods for Deformation, Fracture, and Fatigue*, 4^o ed., Pearson Education, 2012.
- [3] Castro, J. T. P. d., Meggiolaro, M. A. *Fadiga - Técnicas e Práticas de Dimensionamento Estrutural sob Cargas Reiais de Serviço*, vol. 1 e 2, CreateSpace, 2009.
- [4] Bouyer, H. E. *Atlas of Fatigue Curve*. s.1.: American Society of Metals, 1983.
- [5] Bathias, C. *Fatigue Limit in Metals*, ISTE Ltda - John Wiley & Sons Inc, 2014.
- [6] Kazymirovych, V. “Very High Cycle Fatigue of Engineering Materials,” 2009.
- [7] Kazymirovych, V. “Very High Cycle Fatigue of High Performance Steels,” 2008.
- [8] Kazymirovych, V. “Very High Cycle Fatigue of Tool Steels,” 2010.
- [9] Jeddi, D., Palin-Luc, T. A review about the effects of structural and operational factors on the gigacycle fatigue of steels. *Fatigue & Fracture of Engineering Materials & Structures*, 2018, vol.41, pp.969-990.
- [10] Palin-Luc, T., Jeddi, D. The gigacycle fatigue strength of steels: a review of structural and operating factors, *Procedia Structural Integrity*, 2018, vol.13, pp 1545-1553.
- [11] Mora, R. P. “Study of the Fatigue Strength in the Gigacycle Regime of Metallic Alloys in Aeronautics and Off-shores Industries,” 2010.
- [12] Teixeira, M.C. *Comportamento do aço DIN 34CrNiMo6 em fadiga de altíssimo ciclo*. [Dissertation]. Rio de Janeiro: PUC-Rio; 2018 (in Portuguese).
- [13] Stanzl-Tschegg, S. Very high cycle fatigue measuring techniques, *International Journal of Fatigue*, 2014, vol.60, pp 2-17.
- [14] Hopkinson, B., referred by [5]. For a detailed analysis see Hopkinson, B. *Proc. R. Soc. A*86:101.
- [15] Jenkin, C. F., referred by [5]. For a detailed analysis see Jenkin, C. F., *Proc. R. Soc. A*109:119.
- [16] Jenkin, C. F., Lehman, G. D., referred by [5]. For a detailed analysis see Jenkin, C. F., Lehman, G. D., *Proc. R. Soc. A*125:83.
- [17] Manson, W.P., referred by [5]. For a detailed analysis see Manson, W.P., *Piezoelectric Crystals and their Application in Ultrasonics*. New York: Van Nostrand, p.161.
- [18] Girard, F., Vital, G., referred by [5]. For a detailed analysis see Girard, F., Vital, G., *Rev. Metall* 56:25.
- [19] Kikukawa, M., Ohji, K., Ogura, K. J., referred by [5]. For a detailed analysis see Kikukawa, M., Ohji, K., Ogura, K. J., *Basic Eng. (Trans ASME, D)*, 87:857.
- [20] Bathias, C. “There is no Fatigue Infinity Life in Metallic Materials,” *Fatigue & Fracture of Engineering Materials & Structures*, 1999, vol.22, pp. 567-579.
- [21] Wagner, D., Ranc, N., Bathias, C., et al. Fatigue crack initiation detection by an infrared thermography method, *Fatigue Fract Engng Mater Struct.* 2009, vol.33, pp 12–21.

- [22] Fargione, G., Geraci, A., La Rosa, G., Risitano, A. Rapid determination of the fatigue curve by the thermographic method, *International Journal of Fatigue* 2002, vol.24, pp 11–19.
- [23] Mughrabi, H., Antolovich, S. D. “A Tribute to Claude Bathias - Highlights of his pionering work,” *International Journal of Fatigue*, 2016, vol.93, pp. 217-223.
- [24] Vieira, M., De Freitas, M., et al. Development of a Very High Cycle Fatigue (VHCF) Multiaxial Testing Device. *Frattura ed Integrita Strutturale*, 2016, vol.10, pp 131–37.
- [25] Costa, P., et al. Tension/torsion ultrasonic fatigue testing on a railway wheel *Procedia Structural Integrity*, 2020, vol.25, pp 445–453.
- [26] Teixeira, M.C., Brandão, A.L.T., Parente, A.P., Pereira, M.V. Artificial intelligence modeling of ultrasonic fatigue test to predict the temperature increase, *International Journal of Fatigue*, 2022, vol.163, 106999.
- [27] Sakai, T., Nakagawa, A., Oguma, N., et al. A review on fatigue fracture modes of structural metallic materials in very high cycle regime, *International Journal of Fatigue*, 2016, vol.93, pp 339-35.
- [28] Mayer, H. Recent developments in ultrasonic fatigue. *Fatigue Fract Engng Mater Struct*, 2016, vol.39, pp 3–29.
- [29] Shimadzu Excellence in Science. Catalog C225-E036: Very High Cycle Fatigue Testing System USF – 2000A.
- [30] Mughrabi, H. Fatigue, an everlasting materials problem - still en vogue, *Procedia Engineering*, 2010, vol.2, pp 3-26.
- [31] Stanzl-Tschegg, S., Mughrabi, H., Schoenbauer, B. Life time and cyclic slip of copper in the VHCF regime, *International Journal of Fatigue*, 2007, vol.29, pp 2050-2059.
- [32] Mughrabi, H. Specific features and mechanisms of fatigue in the ultrahigh-cycle regime, *International Journal of Fatigue*, 2006, vol.28, pp 1501-1508.
- [33] Dehkord, N. T. High and very high cycle fatigue behavior of DP600 dual-phase steel: correlation between temperature, strain rate, and deformation mechanisms, 2017.
- [34] Pyttel, B., Schwerdt, D., Berger, C. Very high cycle fatigue – Is there a fatigue limit?. *International Journal of Fatigue*, 2011, vol.33, pp 49-58.
- [35] Sakai, T., Sato, Y., Oguma, N. Characteristic S-N properties of high-carbonchromium-bearing steel under axial loading in long-life fatigue,” *Fatigue Fract. Eng.Mater. Struct.*, 2022, vol. 25, pp. 765–773.
- [36] Shiozawa, K., Morii, Y., Nishino, S., Lu, L. “Subsurface crack initiation and propagation mechanism in high-strength steel in a very high cycle fatigue regime,” *Int. J. Fatigue*, 2006, vol.28, pp. 1521–1532.
- [37] Sakai, T., et al. “A review on fatigue fracture modes of structural metallic materials in very high cycle regime,” *Int. J. Fatigue*, 2016, pp. 1–13.
- [38] Ohuchida H., Andoh S. “Fatigue Strength - Hardness Relationship for High Carbon Low Alloy Steel,” *Bulletin of JSME*, 1967.
- [39] Karlson, D. Life and Fracture in Very High Cycle fatigue of a high strength steel, 2021.

- [40] Pereira, M.V., Teixeira, M.C., Darwish, F. A. Correlation between fractographic aspects and stress intensity factor in very high cycle fatigue. *Procedia Structural Integrity*, 2019, vol.17, pp 105-114.
- [41] Kazymyrovych, V., et al. Evaluation of the giga-cycle fatigue strength, crack initiation and growth in high strength H13 tool steel. Fourth international Conference on Very High Cycle Fatigue (VHCF -4), 2007, Ann Arbor, MI, United states.
- [42] Zhao, A., Xie, J., Sun, C., Lei, Z., Hong, Y. “Effects of strength level and loading frequency on very-high-cycle fatigue behavior for a bearing steel,” *Int. J. Fatigue*, 2012, vol.38, pp 46-56.
- [43] Murakami, Y., et al. On the mechanism of fatigue failure in the superlong life regime ($N > 10^7$ cycles). II. A fractographic investigation. *Fatigue & Fracture of Engineering Materials & Structures*, 2000, vol.11, pp 903-10.
- [44] Murakami, Y., Nomoto, T., Ueda, T. Factors influencing the mechanism of superlong fatigue failure in steels. *Fatigue Fract Eng Mater Struct*, 1999, vol.22, pp 581–90.
- [45] Murakami, Y., Matsunaga, H., “The effect of Hydrogen on Fatigue Properties of Steels Used for Fuel Cell System,” *International Journal of Fatigue*, 2006, vol. 28, pp. 1509-20.
- [46] Roiko, A., Murakami, Y. “A design Approach for Components in Ultralong Fatigue Life Steels with Step Loading,” *International Journal of Fatigue*, 2012, vol.41, pp. 140-149.
- [47] Hong, Y., Sun, C. The nature and the mechanism of crack initiation and early growth for very-high-cycle fatigue of metallic materials – An overview, *Theoretical and Applied Fracture Mechanics*, 2017, vol.92, pp 331-350.
- [48] Hong, Y., Liu, X., Lei, Z., Sun, C. The formation mechanism of characteristic region at crack initiation for very-high-cycle fatigue of high-strength steels, *International Journal of Fatigue*, Volume, 2016, vol.89, pp 108-118.
- [49] Grad, P., Reuscher, B., Brodyanski, A., Kopnarski, M., Kerscher, E. Mechanism of fatigue crack initiation and propagation in the very high cycle fatigue regime of high-strength steels. *Scripta Mater*, 2012, vol.67, pp 838–41.
- [50] Murakami, Y., Endo, M., “Effects of Defects, Inclusions and Inhomogeneities on Fatigue Strength,” 1993.
- [51] Murakami, Y. *Metal Fatigue - Effects of Small Defects and Nonmetallic Inclusions*, Elsevier, 2002.
- [52] Yong, D. Li., Li-Li, Z., Fei, Yu-Huan, Liu, Xiao-Yan, Li, Mei-Xia. On the Formation Mechanisms of Fine Granular Area (FGA) on the Fracture Surface for High Strength Steels in the VHCF Regime. *International Journal of Fatigue*, 2016, vol.82, pp 402–10.
- [53] Liu, Y B, Li S.X., Li Y.D., Yang Z.G. Factors Influencing the GBF Size of High Strength Steels in the Very High Cycle Fatigue Regime. *Mater Sci Eng*, 2011, vol.358, pp 935–42.
- [54] Yang, Z G. Estimation of the Size of GBF Area on Fracture Surface for High Strength Steels in Very High Cycle Fatigue Regime. *International Journal of Fatigue*, 2008, vol.30, pp 1016–23.
- [55] Marines-Garcia, I., Paris, P.C., Tada, H., Bathias, C., Lados, D. *Fatigue*

- assessment using an integrated threshold curve method—Applications. *Eng. Fract. Mech.*, 2008, vol.75, pp 1657–1665.
- [56] Crupi, V., Epasto, G., Guglielmino, E., Risitano, G. Analysis of temperature and fracture surface of AISI4140 steel in very high cycle fatigue regime. *Theor Appl Fract Mech.*, 2015, vol.80, pp. 22-30
- [57] Peng, W., Zhang, Y., Qiu, B., Xue, H. A Brief Review of the Application and Problems in Ultrasonic Fatigue Testing. *AASRI Conference on Power and Energy Systems*, 2012, vol.2, pp 127-133.
- [58] Ebara, R. The present situation and future problems in ultrasonic fatigue testing – Mainly reviewed on environmental effects and materials’ screening. *Int J Fatigue*, 2006, vol.28, pp 1465-1470.
- [59] Peng W., Xue H., Ge R., Peng Z. The influential factors on very high cycle fatigue testing results. *MATEC Web OF Conferences* 165, 20002 Fatigue 2018.
- [60] Torabian, Favier, N.V., Dirrenberger, J., Adamski, F., Ziaei-Rad, S., Ranc, N. Correlation of the High and Very High Cycle Fatigue Response of Ferrite Based Steels with Strain Rate-Temperature Conditions. *Acta Mater.*, 2017, vol.134, pp 40–52.
- [61] Hu, Yuanpei, Sun, C., Xie, J., Hong Y. Effects of Loading Frequency and Loading Type on High-Cycle and Very-High Cycle Fatigue of a High-Strength Steel. *Materials (Basel)*, 2018, vol.11.
- [62] Gorash, Yevgen, Comlekci, T., Styger, G., Kelly, J., Brownlie F. Investigation of S275JR+AR Structural Steel Fatigue Performance in Very High Cycle Domain. *Procedia Struct. Integr.*, 2022, vol.38, pp 490–96.
- [63] Bach, J., Göken, M., Höppel, H-W., Fatigue of Low Alloyed Carbon Steels in the HCF/VHCF-Regimes, In “Fatigue of Materials at Very High Numbers of Loading Cycles,” H.-J. Christ (Ed.). Springer Fachmedien Wiesbaden, 2018, pp. 1–23.
- [64] Klusák, J., Horník, Lesiuk, V., Seitzl, G. S. Comparison of high- and low-frequency fatigue properties of structural steels S355J0 and S355J2. *Fatigue FractEngMaterStruct*, 2021, vol.44, pp3202- 3213.
- [65] Guennec, B., et al. Effect of the loading frequency on fatigue properties of JIS S15C low carbon steel and some discussions based on micro-plasticity behavior. *International Journal of Fatigue*, 2014, vol.66, pp 29-38.
- [66] Guennec, B., et al. Dislocation-based interpretation on the effect of the loading frequency on the fatigue properties of JIS S15C low carbon steel. *International Journal of Fatigue*, 2015, vol.70, pp 328-341.
- [67] Guennec, B., et al. Effect of the loading frequency on fatigue properties of JIS S15C low carbon steel and some discussions based on micro-plasticity behavior. *International Journal of Fatigue*, 2014 vol.66, pp 29-38.
- [68] Shao, S., Khonsar, M.M, Wang, J., et al. Frequency dependent, deformation, reversibility, during, cyclic loading. *Material Research Letters*, Taylor and Francis, 2018, vol.6,7, pp 390-397.
- [69] Hu, Y., Sun, C., Xie, J., Hong, Y., Materials Effects of Loading Frequency and Loading Type on High-Cycle and Very-High-Cycle Fatigue of a High-Strength Steel, 2018, vol.11, 1456.

- [70] Mayer, H., Papakyriacou, M., Pippan, R., Stanzl-Tschegg, S. Influence of loading frequency on the high cycle fatigue of AlZnMgCu1.5 aluminum alloy. *Materials Science and Engineering A*, 2001, vol.314, pp 48-54.
- [71] Hirth, J.P., Lothe, J. *Theory of dislocations*. 2nd ed. Malabar (FL): Krieger Publishing Company; 1982. [Google Scholar]
- [72] Arechabaleta, Z., Van Liempt, P., Sietsma, J. Quantification of dislocation structures from anelastic deformation behaviour. *Acta Mater*, 2016, vol.115, pp 314–323.
- [73] Tsutsumi, N., Murakami, Y., Doquet, V. Effect of test frequency on fatigue strength of low carbon steel. *Fatigue Fract Eng Mater Struct*, 2009, vol.32, pp 473–483.
- [74] Amiri, M., Khonsari, M.M. *Introduction to thermodynamics of mechanical fatigue*, CRC Press, 2013.
- [75] Ricotta, M., Meneghetti, G., Atzori, B., Risitano, G., Risitano, A. Comparison of Experimental Thermal Methods for the Fatigue Limit Evaluation of a Stainless Steel, *Metals*, 2019, vol.9, 677.
- [76] Lee, H. W., Basaran, C. Predicting high cycle fatigue life with unified mechanics theory, *Mechanics of Materials*, 2022, vol.164, 104116.
- [77] Ellyin, F. *Fatigue Damage, Crack Growth and Life Prediction*, Chapman & Hall, London, 1997.
- [78] Halford, G.R. The energy required for fatigue, *J. Mater.*, 1966, vol.1, pp 3-18.
- [79] Meneghetti, G., Ricotta, M. The use of the specific heat loss to analyse the low- and high- cycle fatigue behavior of plain and notched specimens made of a stainless steel, *Eng. Fract. Mech.*, 2012, vol.81, pp 2-16.
- [80] Meneghetti, G. Analysis of the fatigue strength of a stainless steel based on the energy dissipation, *International Journal of Fatigue*, 2007, vol.29, pp 81-94.
- [81] Meneghetti, G., Ricotta, M., Atzori, B. A synthesis of the push-pull fatigue behavior of plain and notched stainless steel specimens by using the specific heat loss *Fatigue Fract. Eng. Mat. Struct.*, 2013, vol.36, pp 1306-1322.
- [82] Ellyin, F. *Fatigue Damage, Crack Growth and Life Prediction*, Chapman & Hall, London, 1997.
- [83] Halford, G.R. The energy required for fatigue, *J. Mater.*, 1966, vol.1, pp 3-18.
- [84] Amiri, M., Khonsari, M.M., Rapid determination of fatigue failure based on temperature evolution: Fully reversed bending load, *International Journal of Fatigue*, 2010, vol.32, pp 382-389.
- [85] Jang, J.Y., Khonsari, M.M. On the evaluation of fracture fatigue entropy, *Theoretical and Applied Fracture Mechanics*, 2018, vol.96, pp 351-361.
- [86] Jiang L., Wang, H., Liaw, P.K., et al. Characterization of the temperature evolution during high cycle fatigue. *Metall. Mater. Trans. A* 32, 2279-2296.
- [87] Fargione, G. et al. Rapid determination of the fatigue curve by thermographic method. *International Journal of Fatigue*, 24, 11-19.
- [88] Teng, Z., Wu, H., Boller, C., Starke, P. A unified fatigue life calculation based on intrinsic thermal dissipation and microplasticity evolution, *International Journal of Fatigue*, 2020, vol.131, 105370.
- [89] Lee, H.W., Basaran, C., Egner H., Lipski A., Piotrowski M., Mroziński, S., Noushad Bin Jamal M, Rao, C.L. Modeling ultrasonic vibration fatigue with

unified mechanics theory, *International Journal of Solids and Structures*, 2022, Vol.236–237, 111313.

- [90] Štrumbelj, E., Kononenko, I. “Explaining prediction models and individual predictions with feature contributions.” *Knowl. Inf. Syst*, 2014, vol.41, pp 647–665.
- [91] De-Cheng Feng, Wen-Jie Wang, Sujith Mangalathu, Ertugrul Taciroglu. *Interpretable XGBoost-SHAP Machine-Learning Model for Shear Strength Prediction of Squat RC Walls* American Society of Civil Engineers, 2021, vol.147, 04021173.

Appendix A

23/11/2022 14:22

Rightslink® by Copyright Clearance Center



Home

Help ▾

Live Chat

Sign in

Create Account



Artificial intelligence modeling of ultrasonic fatigue test to predict the temperature increase

Author: M.C. Teixeira, A.L.T. Brandão, A.P. Parente, M.V. Pereira

Publication: International Journal of Fatigue

Publisher: Elsevier

Date: October 2022

© 2022 The Authors. Published by Elsevier Ltd.

Journal Author Rights

Please note that, as the author of this Elsevier article, you retain the right to include it in a thesis or dissertation, provided it is not published commercially. Permission is not required, but please ensure that you reference the journal as the original source. For more information on this and on your other retained rights, please visit: <https://www.elsevier.com/about/our-business/policies/copyright#Author-rights>

BACK

CLOSE WINDOW

© 2022 Copyright - All Rights Reserved | [Copyright Clearance Center, Inc.](#) | [Privacy statement](#) | [Data Security and Privacy](#)
| [For California Residents](#) | [Terms and Conditions](#) Comments? We would like to hear from you. E-mail us at customer@copyright.com

Appendix B

DIN 34CrNiMo6

IST Solda Sample Testing of different Qualities

Análise Química

Amostra / sample ID : CR34-Maria Clara Técnico / Tester: Yuri Nascimento

Cliente / customer : ISI-Senai solda

Material / Material : FE_100

Data. / Date. : 12/05/2023

Hora / Time : 15:37:13

Foundry-MASTER Norma / grade :

	Fe	C	Si	Mn	P	S	Cr	Mo
1	95.2	0.329	0.247	0.467	< 0.0005	0.0008	1.45	0.285
2	95.0	0.397	0.235	0.499	0.0009	0.0023	1.37	0.280
3	94.7	0.428	0.263	0.533	0.0035	0.0099	1.57	0.316
4	94.6	0.308	0.281	0.496	0.0035	0.0063	1.35	0.279
5	94.4	0.272	0.299	0.458	0.0032	0.0054	1.46	0.272
Ave	94.8	0.347	0.265	0.491	0.0022	0.0049	1.44	0.286

	Ni	Al	Co	Cu	Nb	Ti	V	W
1	1.58	0.0058	0.0006	0.224	< 0.0005	< 0.0005	0.0296	< 0.0010
2	1.58	0.0042	< 0.0005	0.302	< 0.0005	< 0.0005	0.0316	0.0042
3	1.58	0.0045	0.0052	0.187	< 0.0005	< 0.0005	0.0421	< 0.0010
4	1.51	0.0104	0.0025	0.198	< 0.0005	0.0016	0.0427	< 0.0010
5	1.63	0.0043	< 0.0005	0.269	< 0.0005	0.0007	0.0294	< 0.0010
Ave	1.57	0.0058	0.0016	0.236	< 0.0005	< 0.0005	0.0351	< 0.0010

	Pb	Sn	B	Ca	Zr	Zn	Bi	As
1	< 0.0010	0.0121	0.0011	0.0002	0.0063	0.0027	< 0.0005	0.0076
2	< 0.0010	0.0103	0.0021	0.0002	0.0069	0.0022	0.0259	0.0069
3	< 0.0010	0.0182	0.0007	0.0002	0.0077	0.0025	0.0179	0.0115
4	< 0.0010	0.0116	0.0001	0.0002	0.0062	0.0022	< 0.0005	0.0090
5	< 0.0010	0.0111	0.0001	0.0001	0.0072	0.0021	< 0.0005	0.0087
Ave	< 0.0010	0.0126	0.0008	0.0002	0.0069	0.0023	0.0087	0.0087

	N	Se	Sb	Ta
1	0.0935	0.0016	0.0295	< 0.0050
2	0.0999	0.0053	0.0251	< 0.0050
3	0.149	0.00453	0.0274	0.0337
4	> 0.200	0.0055	0.0437	0.0121
5	> 0.200	0.0026	0.0276	0.0174
Ave	> 0.200	0.0039	0.0307	0.0132

Oxford Instruments Analytical GmbH
Wellesweg 31
47589 Uedem (Germany)
Tel. : +49 2825 9383-0 Fax: +49 2825 9383100
Web: www.oxford-instruments.com
e-mail: info@oxford-instruments.com

DIN 42CrMo4

IST Solda Sample Testing of different Qualities

Análise Química

Amostra / sample ID : CR42-Maria Clara Técnico / Tester: Yuri Nascimento

Cliente / customer : ISI-Senai solda

Material / Material : FE_100

Data. / Date. : 12/05/2023

Hora / Time : 15:47:13

Foundry-MASTER Norma / grade :

	Fe	C	Si	Mn	P	S	Cr	Mo
1	95.9	0.318	0.100	0.715	0.0048	0.0043	0.938	0.281
2	96.3	0.307	0.0868	0.670	0.0059	0.0052	1.00	0.307
3	96.5	0.316	0.0843	0.644	0.0095	0.0048	0.932	0.287
4	95.7	0.331	0.170	0.699	0.0080	0.0063	0.985	0.274
5	95.7	0.324	0.0835	0.700	0.0071	0.0039	0.964	0.259
Ave	96.0	0.319	0.105	0.686	0.0071	0.0049	0.966	0.282

	Ni	Al	Co	Cu	Nb	Ti	V	W
1	0.823	0.0031	0.0096	0.208	< 0.0005	< 0.0005	0.0794	< 0.0010
2	0.872	0.0018	< 0.0005	0.129	< 0.0005	0.0055	0.0725	< 0.0010
3	0.775	0.0034	0.0113	0.0962	< 0.0005	< 0.0005	0.0766	< 0.0010
4	0.766	0.0031	0.0144	0.135	< 0.0005	< 0.0005	0.0747	< 0.0010
5	0.759	0.0011	0.0030	0.147	< 0.0005	< 0.0005	0.0733	< 0.0010
Ave	0.799	0.0025	0.0077	0.143	< 0.0005	0.0011	0.0753	< 0.0010

	Pb	Sn	B	Ca	Zr	Zn	Bi	As
1	< 0.0010	0.0093	0.0010	0.0001	0.0062	0.0010	0.0256	0.0063
2	< 0.0010	0.0093	0.0004	0.0001	0.0077	0.0014	0.0240	0.0075
3	< 0.0010	0.0111	0.0013	0.0001	0.0097	0.0013	0.0292	0.0090
4	< 0.0010	0.0087	0.0001	0.0001	0.0094	0.0008	0.0266	0.0062
5	< 0.0010	0.0092	0.0006	0.0001	0.0098	0.0015	0.0401	0.0067
Ave	< 0.0010	0.0095	0.0007	0.0001	0.0086	0.0012	0.0291	0.0071

	N	Se	Sb	Ta
1	> 0.200	< 0.0010	0.0662	0.0176
2	0.0564	0.0059	0.0084	0.0293
3	0.0518	0.00423	0.0730	0.0307
4	> 0.200	0.0040	< 0.0010	0.0388
5	> 0.200	0.0047	< 0.0010	0.0338
Ave	> 0.200	0.0038	0.0295	0.0300

Oxford Instruments Analytical GmbH
 Wellesweg 31
 47589 Uedem (Germany)
 Tel. : +49 2825 9383-0 Fax: +49 2825 9383100
 Web: www.oxford-instruments.com
 e-mail: info@oxford-instruments.com